# Abstract


Title of dissertation: Dynamics of Erythrocytes and Microcapsules

Walter R. Dodson III
Doctor of Philosophy, 2008
Fischell Department of Bioengineering

Dissertation directed by: Panagiotis Dimitrakopoulos, Ph.D.
Department of Chemical and Biomolecular Engineering

The erythrocytes are the primary carriers of oxygen and carbon dioxide to and from the systemic tissue. The ability of these cells to deform and navigate through the capillary beds is of fundamental importance for proper functioning of the cardiovascular transport system. The erythrocyte is essentially a capsule, and flow-induced erythrocyte deformation involves the interfacial dynamics of a membrane-enclosed fluid volume stressed in a viscous flow. Elastic capsule dynamics is a complicated problem involving the coupling of fluid and membrane forces; it is also found in a variety of scientific and engineering applications. In this work, we investigate the dynamics of elastic capsules and erythrocytes using the Spectral Boundary Element (SBE) method, a high-order / high-accuracy method for capsule and cellular dynamics.

For strain-hardening Skalak elastic capsules in an extensional flow, our investigations demonstrate a shape transition in accordance with experimental observations [6] to a cusped conformation at high flow rates, which allows the capsule to withstand the increased hydrodynamic forces. Our computational methodology reveals a region of bifurcation, in which both spindled and cusped steady-state geometries

coexist for a single flow rate. The method is also used to investigate the dynamics of strain-softening Neohookean capsules in the same flow pattern. The strain-softening capsules become highly extended at weaker flow rates than strain-hardening capsules, and do not form steady-state cusped shapes.

The SBE method has been extended to model the erythrocyte by using a biconcave disc reference geometry and adaptive prestress to enforce area incompressibility. The method accurately reproduces experimental data from erythrocyte ektacytometry, but allows examination of the erythrocyte dynamics beyond the geometric constraints inherent in ektacytometry and other experimental techniques, including observation of the three-dimensional oscillatory behavior over a range of capillary numbers and viscosity ratios. Our results support a prediction by Fischer, Skalak, and coworkers [32] that the erythrocyte shear modulus decreases at small shear deformations. Our work also suggests that cellular deformation is largely independent of the flow pattern, consistent with the findings of experimental investigators [78].

# Dynamics of Erythrocytes and Microcapsules

by

Walter R. Dodson III

Dissertation submitted to the Faculty of the Graduate School of the
University of Maryland, College Park in partial fulfillment
of the requirements for the degree of
Doctor of Philosophy
2008

Advisory Committee:

Professor Panagiotis Dimitrakopoulos, Chair/Advisor
Professor Raymond A. Adomaitis
Professor Helim Aranda-Espinoza
Professor Marco Colombini
Professor Keith E. Herold

Dedicated to my beautiful and wonderful wife Pawinee,

## Acknowledgements

I would like to thank my advisor, Professor Panagiotis Dimitrakopoulos for support, guidance, and the opportunity to work on such interesting problems in computational physics. I would also like to thank former and current students in our research group, including Inuka D. Dissanayake, Yechun Wang, and Shugi Kuriakose. Special acknowledgement is due to Yechun Wang for developing, in conjunction with Professor Dimitrakopoulos, the numerical method for viscous droplet deformation without which this work would not have been possible. Further, I must acknowledge the Fischell Department of Bioengineering and its Chairman Professor William E. Bentley, in addition to the Department of Chemical and Biomolecular Engineering, both at the University of Maryland, College Park. I must also thank my examining committee members, including Professors Raymond A. Adomaitis, Helim Aranda-Espinoza, Marco Colombini, and Keith E. Herold.

On a personal note, I would like to thank my wife Pawinee for her love and support. I would like to thank my parents Walter and Sandra, for raising me and providing me with so many opportunities. I would also like to thank my sister Stephanie, and my grandparents Walter and Helen. On the other side of the planet, I would like to thank my in-laws Singha and Rean for accepting me into their family, and treating me as one of their own.

This research was supported in part by the National Science Foundation and the National Center for Supercomputing in Illinois.

# Table of Contents

# List of Tables

# List of Figures

# List of Abbreviations

| | | | |
|---|---|---|---|
| $\|_\alpha$ | Covariant derivative [16] | $\boldsymbol{I}$ | Identity tensor [15] |
| $\alpha$ | Prestress parameter [110] | $K$ | Area dilitation modulus [20] |
| $\delta_\alpha^{\ \beta}$ | Identity tensor [14] | $K_d$ | Derivative control [111] |
| $\Delta \boldsymbol{f}$ | Hydrostatic traction [10] | $K_i$ | Integral control [111] |
| $\Delta t$ | Time step [36] | $K_p$ | Proportional control [111] |
| $\kappa$ | Reduced bending modulus [23] | $\boldsymbol{m}$ | Bending moment tensor [23] |
| $\kappa_m^R$ | Mean reference curvature [23] | $\boldsymbol{n}$ | Surface normal vector [14] |
| $\lambda$ | Viscosity ratio [9] | $N_B$ | Number of basis points [35] |
| $\lambda_\alpha$ | Stretch ratios [18] | $N_E$ | Number of elements [34] |
| $\mu$ | Ambient viscosity [9] | $\boldsymbol{N}$ | Reference normal vector [16] |
| $\Psi$ | Mooney-Rivlin parameter [20] | $p$ | Pressure [9] |
| $\boldsymbol{\sigma}$ | Stress tensor [10] | $\boldsymbol{P}$ | Surface projection tensor [15] |
| $\tau_\alpha^P$ | Principal tensions [18] | $\boldsymbol{q}$ | Shear resultant vector [15] |
| $\boldsymbol{\tau}$ | In-plane stress resultant [15] | $R_0$ | Undeformed cell radius [105] |
| $\theta^\alpha$ | Curvilinear parameters [14] | $\mathcal{R}^2$ | 2D Cartesian space [15] |
| $a$ | Characteristic length scale [21] | $\mathcal{R}^3$ | 3D Cartesian space [15] |
| $a_{\alpha\beta}$ | Surface metric tensor [15] | $Re$ | Reynolds number [4] |
| $\boldsymbol{A}$ | Surface strain tensor [17] | $\boldsymbol{S}$ | Stokeslet solution [10] |
| $b_{\alpha\beta}$ | Surface curvature tensor [15] | $t_{area}$ | Area time scale [22] |
| $\hat{\boldsymbol{b}}_\alpha$ | Principal stretch directions [18] | $t_{bend}$ | Bending time scale [23] |
| $\boldsymbol{B}$ | Curvature tensor [22] | $t_{flow}$ | Flow time scale [22] |
| $C$ | Moduli ratio [20] | $t_{shear}$ | Shearing time scale [22] |
| $Ca$ | Elastic capillary number [21] | $\boldsymbol{t}_\alpha$ | Natural surface vectors [14] |
| $D$ | Deformation parameter [44] | $\boldsymbol{t}^\alpha$ | Contravariant base [14] |
| $D_{xy}$ | XY D parameter [119] | $\boldsymbol{T}$ | Reference surface vector [16] |
| $e_n$ | Area error at step n [111] | $\boldsymbol{u}$ | Velocity [9] |
| $E_B$ | Bending modulus [23] | $\boldsymbol{u}^\infty$ | Undisturbed velocity [9] |
| $\boldsymbol{F}$ | Strain tensor [16] | $\boldsymbol{V}^2$ | Left Cauchy-Green tensor [18] |
| $G_s$ | Shear modulus [21] | $\mathcal{W}$ | Strain energy function [19] |
| $h$ | Membrane thickness [15] | $\boldsymbol{x}$ | Geometry [10] |
| $I_\alpha$ | Strain invariant [19] | $\boldsymbol{X}$ | Reference geometry [14] |

*[#]: Page number in which the quantity is defined or first encountered.

# Chapter 1

# Erythrocyte and Microcapsule Rheology

In 1969, Schmid-Schönbein and Wells [74] were studying the shear-thinning properties of human blood. Focusing on the micro-rheological properties of red blood cells, or erythrocytes, they observed that the erythrocyte membrane rotates around the body of the cell when subjected to shear flow. Comparing this motion to the treads of a tank, they hypothesized that the tank-treading motion transmits shear stresses from the ambient fluid to the interior fluid of the cell. Thus, like a viscous droplet, the erythrocyte can participate in the flow, instead of impeding it like a solid particle. Along with the formation and breakup of rouleaux, this mechanism contributes to the shear-thinning behavior of blood [9, 13]. Understanding the fluid dynamic properties of blood therefore requires investigation into flow-induced deformation at the cellular level.

In an ambient flow, an erythrocyte deforms as a capsule, defined as an object consisting of a liquid core enclosed by an elastic or viscoelastic shell [56]. The dynamic behavior of such an object is a fluid mechanics problem coupled to an elastic solid mechanics problem [66]. This necessitates an interdisciplinary approach, wherein a traditional methodology in microfluid dynamics is used in conjunction with an elastic solids framework. Ubiquitous in biological systems, the capsule de-

formation problem is also found in scientific and engineering applications including pharmaceuticals, adhesives, cosmetics, and pesticides [17, 21, 45, 61, 87]. Like an emulsion or a suspension of solid particles, a capsule suspension can exhibit complex viscoelastic flow behavior as a result of the capsule micro-rheology [72]. Therefore, understanding or designing fluid-flow systems with these capsule suspensions requires a comprehension of the behavior of fluid-filled capsules in ambient flow, and the response of these capsules to various flow conditions.

The purpose of this work is to investigate the flow-induced deformation dynamics of elastic capsules and erythrocytes using the Spectral Boundary Element (SBE) method, which we have developed for interfacial dynamics of elastic shells in Stokes flow. This numerical method, originally developed for fixed boundary Stokes flow computations [57, 59], and later for interfacial dynamics and the deformation of viscous droplets [88], has excellent geometric versatility, and it preserves the exponential convergence in accuracy characteristic of spectral methods. The method is more robust than previous methods, and thus it reveals new phenomena, including shape bifurcation at high capillary numbers for strain-hardening elastic capsules. Regarding erythrocytes, the SBE method, as far as we are aware, is the first numerical method to reproduce quantitatively experimental results from erythrocyte ektacytometry at moderate flow rates.

## 1.1 Erythrocyte Physiology

The erythrocytes are the primary carriers of oxygen and carbon dioxide to and from the systemic tissue. The ability of these cells to navigate through the capillary beds is of fundamental importance for proper functioning of the cardiovascular transport system. The lack of a three-dimensional cytoskeleton, coupled with a large surface area to volume ratio, allows erythrocytes to undergo large changes in shape. This is necessary in order for the cells to pass through narrow constrictions in the capillaries, passages often of smaller diameter than the undeformed cells themselves.

An erythrocyte is essentially a capsule, consisting of an outer shell composed of proteins and phospholipids, and a liquid interior. The cytoplasm, although it is a concentrated hemoglobin solution, behaves as a Newtonian fluid, with viscosity 5-6 $cP$ [56, 68]. In healthy blood and in the absence of flow, the erythrocyte assumes a biconcave discoid shape, with a diameter of 7-8 $\mu m$, and 2 $\mu m$ in thickness [9]. The average human erythrocyte has a surface area of 135 $\mu m^2$, and a volume of 94 $\mu m^3$ at physiological osmolarity [30]. For purposes of comparison, a sphere of the same volume would have a surface area of only 100 $\mu m^2$, and a radius of 2.8 $\mu m$. The surface area to volume ratio allows the cells to assume flattened and extended conformations impossible for more spherical cells.

In the capillary beds of the microcirculation, the vessels reach a minimum diameter which is on the order of, and can actually become less than, the major diameter of an erythrocyte. The purpose of these small vessels is to maximize the surface area available for mass transfer. Often the diameter of capillaries is irregular

[77], and the concentration of capillaries in tissue can be high, with a distance of only 34 $\mu m$ between vessels [35]. Moving through this micro-vasculature, erythrocytes form parachute-like shapes, due to the fluid flow and hydrodynamic interactions with the vessel walls [79]. These shapes are in general non-axisymmetric. Other more complicated three-dimensional shapes have also been observed. To estimate a Reynolds number for the flow induced movement of an erythrocyte through a capillary, we will use the erythrocyte diameter and the average viscosity of plasma, 1.1-1.3 $cP$ [77]. The density is approximately that of water, e.g. 1 $g/cm^3$. For the characteristic velocity, we use the results of Vink and Duling [86], regarding erythrocyte movement in hamster capillaries; they observed average red cell velocities in microvessels ranging from 18 to 220 $\mu m/s$. Using the larger observed velocity, one can estimate the upper bound for capillary Reynolds number,

$$Re \approx \frac{8\mu m \times 1 g/cm^3 \times 220 \mu m/s}{1.1 cP} = 0.0016 \ll 1 \tag{1}$$

The Reynolds number shows that the flow is in the Stokes flow regime. Values for the Reynolds number characterizing microcirculatory fluid flow given in the literature are 0.002 for capillaries, 0.01 for venules, and 0.7 for arterioles [10]. Thus, the Stokes flow assumption may still hold on the length scale of the isolated erythrocyte for some vessels slightly larger than the capillaries themselves.

In addition to erythrocytes, white blood cells and platelets are also suspended in the blood, and must navigate through the microcirculation. White blood cells possess an interior three-dimensional cytoskeleton, and thus the dynamics of their deformation is more complex, but they are much less numerous than erythrocytes.

Platelets generally behave as microcapsules, and are discoids approximately half the diameter of erythrocytes. The plasma itself contains dissolved salts, proteins, and miscellaneous organic molecules, which explains why the viscosity is slightly elevated compared to pure water [9].

The capillary walls are composed of endothelial cells, which are specialized for flow control and mass transfer. Thus, the flow does not exhibit the steady, periodic flow behavior of larger vessels. Instead, local muscles embedded in capillary beds constrict and relax in response to a wide variety of stimuli, including exercise, drugs, and metabolic conditions. This causes an irregular local flow pattern, in which local pressure gradients, flow velocities, and even flow directions change frequently in individual vessels. Another characteristic of the capillary vessels is a thick ($0.4 - 0.5\ \mu m$) layer of macromolecules bound or adsorbed to the endothelial cells lining the capillary [75]. This compressive layer, called the glycocalyx, excludes cells and large molecules from the area proximate to the vessel wall, and retards the plasma flow [71]. Also, past modeling investigations suggest that an additional effect of the glycocalyx is to attenuate the size of the transient deformations that an erythrocyte experiences due to capillary irregularities [77]. In this way, the glycocalyx may actually help minimize the mechanical wear on the cells.

Several diagnostic processes have been developed which attempt to quantify the deformability of individual erythrocytes or populations. Here, we describe the basic experimental setup for two devices. Greater analysis of the flow pattern and cellular geometric orientation for these systems appears in Chapter 6.

Historically, the most common device used to assess erythrocyte deformability

is the light-diffraction ektacytometer [11, 12, 40]. A suspension of erythrocytes in a high-viscosity medium is placed into a Couette viscometer. A laser beam is shot radially from inside the inner cylinder. It passes through the medium and produces a diffraction pattern, which is either circular for undeformed cells, or ellipsoidal for elongated, tank-treading cells [11]. The dimensions of the diffraction pattern are inversely proportional to the dimensions of the actual deformed cells, viewed in the plane perpendicular to the direction of the laser. The diffraction pattern can therefore be used to calculate the average dimensions of the deformed cell population (viewed in that plane), either by measuring light intensities across the diffraction pattern [12], or, as in the modern systems, by using a computer to fit an ellipsoid to the diffraction pattern [40]. The data is usually reported as a deformation index, similar to the Taylor parameter, which ranges between 0 (no deformation) and 1 (infinite deformation).

A second device used to evaluate erythrocyte deformability is a counter-rotating parallel plate system, as in Dobbe *et al.* [27, 28]. Here, a suspension of erythrocytes is inserted between two circular, parallel plates, which shear the cells by rotating in opposite directions. An inverted microscope and automated photography system captures images of the deformed cells. While the average results are consistent with ektacytometry, this experimental system was designed to study deformability distributions within a population of erythrocytes. Note that although this system produces images of individual deformed cells, it does not follow individual cells over time.

Microchannel devices have also been developed, in which the cells are passed

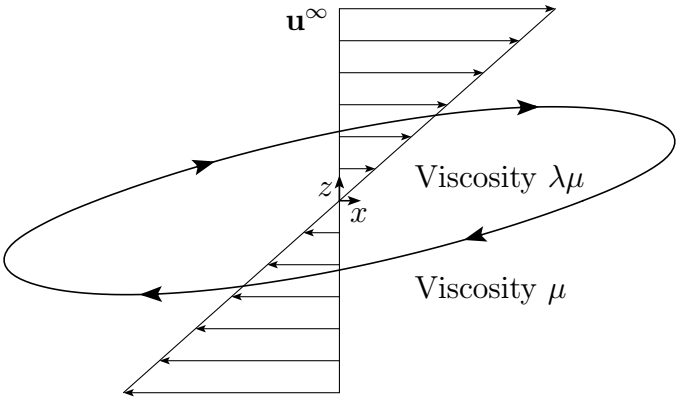


Figure 1.1: A capsule with internal viscosity $\lambda\mu$ suspended in an ambient fluid with viscosity $\mu$ undergoing linear shear flow extends and tank-treads as a result of the shearing forces. The undisturbed fluid velocity field is shown superimposed over the deformed capsule.

through a narrow channel or tube. Unlike traditional ektacytometry or parallel plate systems, microchannel devices have no counter-rotating parts and require no precise motors or control systems, but merely a constant pressure gradient. Therefore, designs based upon these devices are thought to hold greater promise for the development of cheap, disposable systems that can be used in a clinical setting [15]. The flow pattern for these new systems is not a simple shear flow, as it was for previous experimental setups. However, when cellular deformation is considered as a function of wall shear stress, microchannel devices produce comparable results to light-scattering techniques [78].

## 1.2 Stokes Flow and the Boundary Integral Equations

When a capsule, such as an erythrocyte, deforms in response to an ambient flow, resistive elastic forces in the membrane couple to the hydrodynamic forces. For both experimental and numerical investigations, the two most commonly studied basic flow patterns are linear shear flow, illustrated in Figure 1.1, and planar hyperbolic flow (which can be seen in Figure 4.1). Chang and Olbricht [18, 19], for instance, extensively characterized the deformation of an oil droplet covered in a thin polymeric membrane in both shear flow and planar hyperbolic flow (also called two-dimensional extensional flow). They generated the planar hyperbolic flow with a four-roll mill, and the shear flow with a Couette viscometer, as in erythrocyte ektacytometry. These experiments are delicate. One challenge in controlling these flow systems is that while both flow patterns contain a central stagnation point, this is not a stable position for a particle, because the slightest perturbation will cause it to be carried away. Especially in the case of planar hyperbolic flow, the rollers must be carefully readjusted throughout the experiment to keep the capsule centered on the stagnation point. Walter *et al.* [87] also used a Couette viscometer to observe capsule deformation in shear flow; they focused on shape oscillations from steady-state and capsule wrinkling. A third device commonly used to deform capsules in ambient flow is the spinning drop tensometer [44, 61]. In this technique, a capsule is placed in a narrow cylindrical tube. A motor spins the tube, creating concentric circular streamlines inside (i.e. a Couette flow). The centrifugal force elongates the capsule; this results in an axisymmetric deformed geometry. More complex fluid

flows, including those found in blood vessels, have both shear and extensional components; the basic flow patterns discussed here are useful to illustrate the effects of these components on the capsule or cellular deformation.

The physical system in which a capsule deforms as the result of an ambient flow is illustrated in Figure 1.1. Under shearing forces, an initially spherical capsule extends and then tank treads. The figure shows the case in which the undisturbed velocity field $\boldsymbol{u}^{\infty}$ is a linear shear flow, but the formulation discussed here is equally valid for any $\boldsymbol{u}^{\infty}$. The ambient fluid has viscosity $\mu$, and the interior fluid viscosity $\lambda\mu$. For systems involving individual erythrocytes and microcapsules, the conditions hold for Stokes flow ($Re \ll 1$). Therefore the Navier-Stokes equation simplifies to the Stokes equation. We also have the continuity equation. For the ambient fluid, with pressure $p$ and fluid velocity $\boldsymbol{u}$, these equations will be written as follows, and for the internal fluid the appropriate viscosity $\lambda\mu$ substituted for $\mu$.

$$-\nabla p + \mu \nabla^2 \boldsymbol{u} = 0 \tag{2}$$

$$\nabla \cdot \boldsymbol{u} = 0 \tag{3}$$

Taken together, these equations describe the behavior of a viscous, incompressible fluid at low Reynolds numbers, when inertia is negligible. Because these equations are time invariant, force equilibrium is assumed to hold at every instant. As with a viscous droplet, the Boundary Integral Equations (BIE) can be derived in the standard manner from the Stokeslet singularity solutions [62]. For a droplet suspended in an unbounded ambient fluid, the appropriate form of the BIE is the

combined form,

$$(1+\lambda)\boldsymbol{u}(\boldsymbol{x}_0) - 2\boldsymbol{u}^{\infty}(\boldsymbol{x}_0) =$$

$$\frac{-1}{4\pi\mu}\oint_S [\Delta\boldsymbol{f}(\boldsymbol{x})\cdot\boldsymbol{S}(\boldsymbol{x},\boldsymbol{x}_0) - \mu(1-\lambda)\boldsymbol{n}(\boldsymbol{x})\cdot\boldsymbol{T}(\boldsymbol{x},\boldsymbol{x}_0)\cdot\boldsymbol{u}(\boldsymbol{x})]dS \tag{4}$$

In this expression, $\boldsymbol{u}(\boldsymbol{x})$ is the actual velocity at point $\boldsymbol{x}$ defined only on the interface. $\Delta\boldsymbol{f}(\boldsymbol{x})$ corresponds to the hydrodynamic traction across the interface at point $\boldsymbol{x}$. This is equal to the load on the membrane at that point. It can also be defined from the three-dimensional stress tensor $\boldsymbol{\sigma}$ in the inner and outer fluids, and the unit normal $\boldsymbol{n}(\boldsymbol{x})$.

$$\Delta\boldsymbol{f} = \boldsymbol{n}\cdot(\boldsymbol{\sigma}_{exterior\,fluid} - \boldsymbol{\sigma}_{interior\,fluid}) \tag{5}$$

Tensors $\boldsymbol{S}(\boldsymbol{x},\boldsymbol{x}_0)$ and $\boldsymbol{T}(\boldsymbol{x},\boldsymbol{x_0})$ are the Stokeslet solutions for velocity and stress at $\boldsymbol{x}_0$ that would be produced by a point disturbance located at $\boldsymbol{x}$. Note that in the case where the viscosity ratio is unity ($\lambda = 1$), the second term of the integrand vanishes.

If either the velocity distribution or the force vector $\Delta\boldsymbol{f}$ is known along the capsule surface, Eq. (4) can be evaluated to solve for the unknown quantity. The BIE, which describes the fluid dynamics, couples to a solid mechanics description of the interface via boundary conditions. The first condition is that velocity must be continuous across the interface,

$$\boldsymbol{u}_{interior\,fluid} = \boldsymbol{u}_{membrane} = \boldsymbol{u}_{exterior\,fluid} \tag{6}$$

With a capsule, the surface representation is Lagrangian, in which the mathematical interface represents material points directly [72] (Note that this differs

from methods for viscous droplet deformation in Stokes flow, i.e. Wang and Dimitrakopoulos [88]). The interface $\boldsymbol{x}$ then convects with the whole fluid velocity,

$$\frac{\partial \boldsymbol{x}}{\partial t} = \boldsymbol{u} \tag{7}$$

The second boundary condition is that the load on the membrane, $\Delta \boldsymbol{f}$, must correspond to the load computed from an elastic solid mechanics description. An appropriate framework is discussed in Chapter 2.

## 1.3 Outline

Chapter 2 discusses the mechanics of thin elastic shells, and presents a complete system for membrane mechanics which we employ in our numerical method. Topics include membrane statics, appropriate membrane elastic constitutive laws, and dimensionless groups. Chapter 3, after a brief review of past elastic capsule models, then presents the Spectral Boundary Element (SBE) numerical method, validates it by showing agreement with previous low-order numerical methods, and evaluates its properties, including exponential convergence in numerical accuracy. Further, the method is shown to produce numerical solutions for regions of capillary numbers where previous, low-order methods fail.

Chapter 4 employs the SBE method for elastic capsules to study the physical problem of a strain-hardening Skalak capsule deforming in strong planar extensional flows. In contrast to previous methodologies, which fail to converge to a steady-state [48], the SBE method reveals a process of cusp formation at high flow rates, in which capsule edges form spindles and then steady-state cusps due to compressive tensions

at capsule tips. This behavior matches experimental phenomena previously observed [6]. Further, the method reveals a range of high capillary numbers characterized by shape bifurcation, in which both cusped and concave equilibrium configurations exist. Following, Chapter 5 examines the same problem involving a Neohookean capsule. In contrast to the Skalak capsules, these capsules are strain-softening, and at high flow rates produce lamellar shapes with concave edges.

In Chapter 6, the method is extended to model the erythrocyte. The area incompressibility characteristic of the erythrocyte membrane is enforced via a novel implementation of membrane prestress. The extended SBE method produces results in excellent quantitative agreement with experimental observations for erythrocytes in shear flow. It is also used to examine the effects of flow rate and viscosity ratio on capsule geometry, and to examine the transition from tank-treading to tumbling motion. In Chapter 7, the erythrocyte model is used for further investigations, specifically erythrocyte deformation in extensional flow, and the shear-induced deformation of swollen erythrocytes.

Finally, in Chapter 8, we draw some broad conclusions from our results.

# Chapter 2

# Membrane Mechanics

A membrane is a three-dimensional object in which the aspect ratio in one direction is much smaller than in the other two. Membranes can have complex molecular substructure; many membranes are cross-linked polymers, while biological membranes are lipid bilayers. The mechanical properties of a membrane depend on molecular interactions. Many attempts have been made to start with a molecular description of the membrane, and use statistics or molecular modeling to extrapolate a macroscopic account of mechanical phenomena [31, 34, 37, 53]. Li, Lim, and Suresh [51] have even created a whole-cell statistics-based model of erythrocyte deformation. However, this approach is too complicated, if the intention is to couple the mechanical description to the behavior of an ambient fluid; a continuum mechanics approach is more appropriate.

Méléard [54] categorizes possible finite membrane deformations into three basic types. First, the membrane can be sheared in-plane, without changing the surface area. Second, the membrane can be extended in-plane such that the surface area increases. Finally, the membrane can be bent such that the curvature changes. More complex deformations can be expressed as a combination of these basic types. Each basic deformation can be characterized by a modulus of resistance. Ignoring surface

viscosity, a complete description of the mechanical properties of a membrane can therefore consist of a shear modulus, an area dilatation modulus, and a bending modulus.

Because of the aspect ratio, an additional simplification beyond the continuum assumption is possible; the membrane can be considered as a two-dimensional surface in three-dimensional space. This approach, which we use in the SBE method, is called a theory of thin shells.

## 2.1 Membrane Statics

The thin shell description presented below is the general tensorial form, using arbitrary curvilinear surface parameters. Geometric constraints such as axisymmetry simplify the equations. These simplified forms have been used in past studies, but will not be used here. The membrane is treated as a two-dimensional continuum called the middle surface, with arbitrary curvilinear coordinates $\theta^\alpha$ ($\alpha = 1, 2$). By convention, Greek indices are curvilinear and range over 1,2, while Roman indices are Cartesian and range over 1,2,3. Repeated indices are summed. Define the surface tangents $\boldsymbol{t}_\alpha$ by differentiation of surface geometry.

$$\boldsymbol{t}_\alpha \equiv \frac{\partial \boldsymbol{x}}{\partial \theta^\alpha} \tag{1}$$

The unit normal will be $\boldsymbol{n}$. The complete basis system consisting of $\boldsymbol{t}_\alpha$ and $\boldsymbol{n}$ is called the natural basis. A set of reciprocal tangents $\boldsymbol{t}^\alpha$ can be defined such that $\boldsymbol{t}_\alpha \cdot \boldsymbol{t}^\beta = \delta_\alpha{}^\beta$ ($\boldsymbol{n}$ is its own reciprocal). Tensors can then be expressed in either covariant or contravariant components with respect to the base in the standard

manner [60]. The metric tensor $a_{\alpha\beta}$ and surface curvature tensor $b_{\alpha\beta}$ are also both defined in the standard manner [60].

Tensors defined in $\mathcal{R}^3$ must then be transformed into $\mathcal{R}^2$. Define the tangential projection operator $\boldsymbol{P} \equiv (\boldsymbol{I} - \boldsymbol{nn})$. Then the 2nd-order stress tensor $\boldsymbol{\sigma}$ is transformed into the 2nd-order tensor $\boldsymbol{\tau}$, which contains in-plane forces, and into the 1st-order tensor (vector) $\boldsymbol{q}$, which contains transverse shearing forces [36, 69]

$$\boldsymbol{\tau} \equiv \int_{-h/2}^{h/2} \boldsymbol{P} \cdot \boldsymbol{\sigma} \cdot \boldsymbol{P} \; dn \tag{2}$$

$$\boldsymbol{q} \equiv \int_{-h/2}^{h/2} \boldsymbol{P} \cdot \boldsymbol{\sigma} \cdot \boldsymbol{n} \; dn \tag{3}$$

In this expression, $h$ is the membrane thickness, and $dn$ is a differential element in the normal direction, with origin on the middle surface. The only forces not transformed into either $\boldsymbol{\tau}$ or $\boldsymbol{q}$ are those forces with the middle surface as a plane of action. This surface is the hydrodynamic interface; these forces will be recovered in the force balance. One additional transformation, that of the bending moments, is required,

$$\boldsymbol{m} \equiv \int_{-h/2}^{h/2} \boldsymbol{z} \times (\boldsymbol{P} \cdot \boldsymbol{\sigma} \cdot \boldsymbol{P}) dn \tag{4}$$

Here $\boldsymbol{z}$ is a vector to the integration point from the origin on the middle surface. A force balance over an arbitrary differential area of membrane results in expressions for the contravariant components of the hydrostatic traction $\Delta \boldsymbol{f}$ across the membrane [67, 69, 89]

$$\Delta f^{\beta} = -\tau^{\alpha\beta}|_{\alpha} + b^{\beta}_{\alpha} q^{\alpha} \tag{5}$$

$$\Delta f^{\boldsymbol{n}} = -b_{\alpha\beta}\tau^{\alpha\beta} - q^{\beta}|_{\beta} \tag{6}$$

The $q^\alpha|_\beta$ notation denotes covariant differentiation. (See Papastavridis [60] for further explication of the calculus of differential surface geometry.) A subsequent torque balance using the bending moment tensor $\boldsymbol{m}$ yields expressions for the transverse shear vector $\boldsymbol{q}$ and the antisymmetric component of the in-plane stress resultant.

$$q^\beta = m^{\alpha\beta}|_\alpha \tag{7}$$

$$\tau^{[\alpha\beta]} = \frac{1}{2}(b^\alpha_\gamma m^{\gamma\beta} - b^\beta_\gamma m^{\gamma\alpha}) \tag{8}$$

Of the three types of elementary membrane deformations discussed previously, shear and area dilatation are called elastic membrane behavior, and are discussed in the next section. They involve formation only of symmetric in-plane stress $\boldsymbol{\tau}^{(S)}$ and not of transverse shear $\boldsymbol{q}$ or moment tensor $\boldsymbol{m}$. Bending contributions are described in Section 2.3.

## 2.2 Membrane Elastic Behavior

The in-plane stress resultant tensor $\boldsymbol{\tau}$ is the two-dimensional analog of the three-dimensional stress, but to describe elastic behavior, it is also necessary to have an analog of strain. This is accomplished by projection of the three-dimensional deformation gradient $\boldsymbol{F}$, which is defined as a linear transformation from a differential element in a reference three-dimensional object to a deformed state. Denoting $d\boldsymbol{x}$ the deformed element, and $d\boldsymbol{X}$ the reference element, $d\boldsymbol{x} = \boldsymbol{F} \cdot d\boldsymbol{X}$ [52] (For vectors, capital letters will denote the reference shape, and lower-case letters the deformed shape, e.g. the reference tangents and normal will be denoted $\boldsymbol{T}_\alpha$ and $\boldsymbol{N}$,

| Membrane Material | Characteristics | Elastic Behavior |
|---|---|---|
| Ultra-thin oil-water interface membrane [61] | • Forms at oil-water interface by radical polymerization and cross-linking of aminomethacrylates<br>• Amphiphilic<br>• Can be used to encapsulate an oil droplet in an aqueous environment<br>• Extremely small thickness means no appreciable membrane thinning can occur | Neohookean |
| Cross-linked polymer [87] | • Polymer disentanglement causes strain softening<br>• Example: Polyamide or polysiloxane | Mooney-Rivlin |
| Biocompatible serum albumin alginate [17] | • Relaxation of membrane exhibits little hysteresis, indicating almost purely elastic activity | Skalak |
| Red blood cell membrane [8] | • Large area dilatation modulus | Skalak |

Table 2.1: Common membrane material compositions, and appropriate two-dimensional elastic constitutive laws.

respectively). To produce the surface equivalent, called the surface strain tensor, we project [7, 69]

$$\boldsymbol{A} \equiv (\boldsymbol{I} - \boldsymbol{nn}) \cdot \boldsymbol{F} \cdot (\boldsymbol{I} - \boldsymbol{NN}) \tag{9}$$

The effect of the projection is that the linear operator $\boldsymbol{A}$ only transforms elements from the plane of the reference surface, and it only transforms those elements into the plane of the deformed surface. The strain tensor $\boldsymbol{A}$ is most easily calculated by $\boldsymbol{A} = \boldsymbol{t}_\alpha \boldsymbol{T}^\alpha$ [84]. The left Cauchy-Green strain tensor is calculated in the

standard manner ($\boldsymbol{V}^2 = \boldsymbol{A} \cdot \boldsymbol{A}^T$) to eliminate rotational transformation. The left Cauchy-Green tensor has two nonzero eigenvalues, corresponding to the squares of the principal stretch ratios $\lambda_\alpha$. The corresponding unit eigenvectors $\hat{\boldsymbol{b}}_\alpha$ are the directions of principal stretch. The symmetric portion of the in-plane stress $\boldsymbol{\tau}$ is given by a dyadic product [52].

$$\boldsymbol{\tau}^{(S)} = \sum_\alpha \tau_\alpha^P \hat{\boldsymbol{b}}_\alpha \hat{\boldsymbol{b}}_\alpha \tag{10}$$

The values $\tau_\alpha^P$ are called the principal elastic tensions; they are calculated from the stretch ratios via a constitutive law, where the appropriate constitutive law depends on the material composition of the membrane. These constitutive laws and their origins are discussed further in Section 2.2.1. Some representative membrane materials and the appropriate constitutive laws are listed in Table 2.1. The principal tensions are also important as an indicator of membrane buckling [48]. Recall that the basic assumption of thin-shell theory is that the characteristic length scale must be much smaller in the normal direction than in any in-plane direction. One way in which this assumption can fail is when an elastic membrane, devoid of flexural resistance, wrinkles in response to compression. In this situation, the length scale in some direction on the membrane surface can become of approximately the same magnitude as the membrane thickness. Then the equations of thin-shell theory will no longer hold. For numerical solutions, this usually results in breakdown of the numerical method. A necessary but not sufficient condition for membrane wrinkling is that at least one of the principal tensions becomes negative. Wrinkling in ambient flow has been observed experimentally [87].

### 2.2.1 Membrane Elastic Types

The stretch ratios $\lambda_\alpha$ can be used to form two-dimensional surface strain invariants $I_1$ and $I_2$. The first represents elongation, and the second local area dilatation.

$$I_1 = tr(\boldsymbol{V}^2) - 2 = \lambda_1^2 + \lambda_2^2 - 2 \tag{11}$$

$$I_2 = \lambda_1^2 \lambda_2^2 - 1 \tag{12}$$

The strain energy function $\mathcal{W}$, which represents the change in local energy in response to deformation, is classically given in terms of the strain invariants [7, 63]. The exact form of $\mathcal{W}$ depends on the material composition of the membrane. $\mathcal{W}$ can either be derived from known three-dimensional elasticity laws, or developed *de novo* for the two-dimensional case. The symmetric tension tensor $\boldsymbol{\tau}^{(S)}$, which was given in Eq. (10) as a dyadic product of the left Cauchy-Green eigenvectors, can also be written in terms of the invariant derivatives of the strain energy $\mathcal{W}$. Here $J_s = \lambda_1 \lambda_2$.

$$\boldsymbol{\tau}^{(S)} = \frac{2}{J_s} \frac{\partial \mathcal{W}}{\partial I_1} \boldsymbol{V}^2 + \frac{\partial \mathcal{W}}{\partial I_2} J_s^2 (\boldsymbol{I} - \boldsymbol{nn}) \tag{13}$$

If the form of $\mathcal{W}$ is known, Eq. (13) can be evaluated algebraically to derive an expression for the principal tensions $\tau_\alpha^P$ induced by elastic stretching as a function of the stretch ratios $\lambda_\alpha$. The constitutive expressions produced are convenient for numerical evaluation of $\tau_\alpha^P$, which can then be used to produce the tensor $\boldsymbol{\tau}^{(S)}$. Barthès-Biesel and coworkers [7, 8] list several expressions for $\tau_1^P$, derived from strain energy functions. These are summarized in Table 2.2. To calculate $\tau_2^P$, merely reverse the $\lambda_\alpha$ subscripts.

| Material Law | Equation and Description |
|---|---|
| Mooney-Rivlin | $\tau_1^P = \frac{G_s}{\lambda_1\lambda_2}(\lambda_1^2 - \frac{1}{\lambda_1^2\lambda_2^2})[\Psi + \lambda_2^2(1-\Psi)]$<br>$\Psi$ : Mooney-Rivlin parameter $(0 \leq \Psi \leq 1)$<br>• Assumes thin, isotropic, volume incompressible rubber-like sheet.<br>• $\Psi \rightarrow 1 \Rightarrow$ Material behavior approaches Neo-hookean<br>• $\Psi \rightarrow 0 \Rightarrow$ Strain softening (rubber) behavior occurs |
| Neohookean | $\tau_1^P = \frac{G_s}{\lambda_1\lambda_2}(\lambda_1^2 - \frac{1}{\lambda_1^2\lambda_2^2})$<br>• Special case of Mooney-Rivlin in which $\Psi = 1$ |
| Skalak | $\tau_1^P = \frac{G_s\lambda_1}{\lambda_2}(\lambda_1^2 - 1 + C\lambda_2^2[(\lambda_1\lambda_2)^2 - 1])$<br>$K$ : Modulus of resistance to area dilatation<br>$C$ : Moduli ratio $(C \equiv K/G_s)$<br>• Originally derived by Skalak to describe the mechanics of red blood cell membranes.<br>• Exhibits strain stiffening behavior |

Table 2.2: Two-dimensional elastic laws derived from strain energy functions for use in thin-shell membrane mechanics. In every law, $G_s$ stands for the shear modulus.

Any of the laws in Table 2.2 can be modified with the addition of a viscoelastic element in series. Denoting $\mu_s$ the surface viscosity and $D\lambda_1/Dt$ the material derivative of $\lambda_1$, the viscoelastic contribution can be expressed:

$$\tau_1^v = \frac{2\mu_s}{\lambda_1}\left(\frac{D\lambda_1}{Dt}\right) \tag{14}$$

Additional forms of elastic constitutive laws examined in previous numerical studies include a material model based on a network of interconnected springs [58], and a zero-thickness incompressible elastic shell formulation [72]. Note that the latter case is the two-dimensional limit of a three-dimensional material description, and as such the strain invariants are different.

Each of the expressions for $\tau_1^P$ involves two moduli, one for shearing and one for area dilatation, corresponding to two of the three basic membrane deformations discussed previously. In each case, the parameter that stands for area dilatation, as used in the expression, is already dimensionless. This is the Mooney-Rivlin parameter $\Psi$, for a Mooney-Rivlin membrane, and the moduli ratio C in the Skalak expression. The shearing modulus $G_s$ can also be used to form a dimensionless group when the membrane is in contact with ambient flow. This dimensionless group is the capsule analog of the capillary number for viscous droplets. It is often called the elastic capillary number.

$$Ca = \frac{\mu G a}{G_s} \tag{15}$$

Here $\mu$ is the viscosity of the ambient fluid, $G$ is the shear rate, and $a$ is a characteristic length scale, often the radius of a sphere with the same volume as the capsule. $Ca$ shows the ratio of viscous forces in the fluid to resistive elastic forces

in the membrane. Slightly different dimensionless groups have been used by some studies in the past [58, 72]. Both membrane shearing and area dilatation elastic response are associated with a characteristic time scale, determined by the dimensionless form. Understanding the time scales associated with deformation is vital for selecting an appropriate time step for numerical implementation of capsule deformation. The time scale for membrane shear response increases with the elastic capillary number ($t_{shear}/t_{flow} \sim Ca$), while the time scale for area dilatation decreases with the moduli ratio ($t_{area}/t_{shear} \sim C^{-1}$). Throughout this work, all reported values are non-dimensional. Time $t$ has been scaled by shear rate $G$, lengths by capsule radius $R$, and tensions by shear modulus $G_s$

## 2.3 Resistance to Bending

Bending moments occur when the curvature at a point on the membrane is different in the deformed than in the reference state. The curvature of a two-dimensional surface defined in $\mathcal{R}^3$ is a second-order tensor, which can either be expressed in surface component form ($b_{\alpha\beta}$), or in a general tensorial form. In tensorial form, it is defined by differentiation of the normal vector

$$\boldsymbol{B} \equiv (\boldsymbol{I} - \boldsymbol{nn}) \cdot \nabla \boldsymbol{n} \equiv \nabla_S \boldsymbol{n} \tag{16}$$

The relationship between a change in curvature and the induced bending moments is quite complicated. Consequently, most past numerical implementations that incorporated bending assumed axisymmetry [7, 22, 23, 24, 47, 77]. One simplification, to make the general case more approachable, is to assume a linear de-

pendence of bending moments on curvature deviation in any given direction. If in addition the reference curvature is uniform in all directions, a reference mean curvature $\kappa_m^R$ can be projected onto the deformed surface. By subtracting this from the actual curvature, we obtain the difference in curvature in every direction on the surface [69]

$$\boldsymbol{m} = E_B[\boldsymbol{B} - \kappa_m^R(\boldsymbol{I} - \boldsymbol{nn})] \tag{17}$$

Here $E_B$ is the bending modulus, the third characteristic value of membrane mechanical response. This is the expression used in past non-axisymmetric numerical studies of capsule deformation that included resistance to bending [47, 67]. A theoretical framework for incorporating non-uniform reference curvature was developed by Steigmann and Ogden [84]. As far as we are aware, this sort of bending description has not been incorporated into a numerical model. Using the shear modulus from the elastic expressions, and scaling with a characteristic length $a$, we can use $E_B$ to form a third dimensionless parameter for membrane deformation, called the dimensionless bending modulus $\kappa$

$$\kappa \equiv \frac{E_B}{a^2 G_s} \tag{18}$$

The associated time scale for bending decreases with increasing $\kappa$ ($t_{bend}/t_{shear} \sim \kappa^{-1}$). Alternatively, one could combine $E_B$ with the shear rate $G$ to produce a bending analog of the capillary number.

Many techniques have been developed for experimental determination of the membrane mechanical properties discussed here. Often, a technique can be designed such that one of the three basic types of deformation discussed is dominant, and thus

the associated modulus can be studied in isolation. Osmotic swelling [82], for instance, produces only area dilatation, while on the other hand, thermal fluctuations of the membrane result primarily in localized bending deformation [54]. Analyzing these deformations, one can measure either area dilatation modulus or bending modulus, respectively. Other experimental techniques, including compression between parallel plates [17] and micropipette aspiration [43], produce an axisymmetric deformed geometry. The simplified geometries in these experimental systems also allow easier analytical or numerical analysis.

## 2.4 Erythrocyte Membrane Parameters

The spectrin network is the primary determinant of membrane shear response, because, in comparison, the plasma membrane exhibits negligible shear resistance. The ability of spectrin to extend and refold allows the erythrocyte membrane to undergo large shearing deformations as it moves through the capillaries. The reported elastic shear modulus $G_s$ for a red blood cell is $6 \times 10^{-3}\ mN/m$ [56, 73, 77]. The delay in unfolding individual repeat domains in the spectrin peptide also gives rise to a shear viscosity $\mu_s$ of approximately $10^{-3}\ mN \cdot s/m$ [77].

One might expect that the spectrin network could easily change its surface area. However, unlike in the case of shear deformation, the plasma membrane, not the spectrin network, dictates the resistance to area dilatation. The plasma membrane is volume incompressible under physiological conditions, and resists thinning. The effective area modulus $K$ for a red blood cell membrane is therefore fairly large.

Reported values are all close to 450 $mN/m$ [39, 56]. The effective moduli ratio $C$ for a red blood cell membrane is therefore on the order of $10^4$-$10^5$. This indicates that only small changes in surface area will be observed under physiological conditions. Indeed, an area increase of more than 2-4 % causes cell lysis [39].

The bending resistance of an erythrocyte membrane can be thought of as arising from preferred bond angles of the protein network, or from the symmetry of the hexagonal spectrin distribution [67], as well as from the bending resistance inherent in the lipid bilayer [56]. The reported value for the bending modulus $E_B$ is $1.8 \times 10^{-16}$ $mJ$ [73, 77]. Combining the bending modulus with values given previously, we estimate the reduced bending modulus $\kappa$ to be only $3.8 \times 10^{-3}$. The dynamics of deformation for the geometry is therefore determined by shear and area dilatation resistance, with little if any bending influence. Bending resistance will not have an effect on the overall shape [56], but may act on the geometry at a local level, ameliorating small-scale severe curvature gradients, i.e. preventing local buckling.

# Chapter 3

# Spectral Boundary Element Method For Elastic Capsules

To solve the system described in Chapters 1 and 2, we have implemented the Spectral Boundary Element (SBE) numerical method for the case of an interfacial dynamics problem with an elastic interface, in the absence of flexural resistance. The SBE method is a high-order method developed for fixed boundary Stokes flow computations [57, 59], and later for interfacial dynamics and the deformation of viscous droplets [88]. Because it is a Boundary Element method, the SBE method avoids the primary disadvantage of spectral methods for volume discretization, specifically that the resulting linear system is large and dense. The reduction in dimensionality associated with the Boundary Integral formulation results in a linear system that, while still dense, is much smaller than would result from volume discretization. This approach combines the benefits of the spectral methods, including exponential convergence and numerical stability, with the geometric versatility and parallel scalability associated with finite element and boundary element models. The SBE is the only available high-order/high-accuracy method for droplet deformation, and now for capsule deformation, in viscous Stokes flow.

In this chapter, we will first review past solutions and methods for the elastic capsule deformation problem. Following, we will present the SBE numerical method, validate it through comparison with previous numerical methods, and evaluate its properties, including robustness and accuracy.

## 3.1 Past Solutions to the Capsule Deformation Problem

It is apparent that the membrane mechanics description discussed in Chapter 2 coupled to the Stokes condition results in a nonlinear system. As such, the only analytic solutions to the transient problem have been developed for simplified cases. The seminal paper in this field is the 1981 work by Barthès-Biesel and Rallison [4], in which they develop a transient, small-deformation solution for initially spherical capsules with general two-dimensional Lagrangian elastic boundaries. By ignoring flexural resistance, they rewrite the membrane statics formulation in the simplified form $\Delta \boldsymbol{f} = -\nabla_S \cdot \boldsymbol{\tau}$. Because they assume that all deformations are small, they can consider the deformation tensor $\boldsymbol{F}$ as a perturbation of the identity matrix, and $\boldsymbol{n}$ as a perturbation of the reference normal $\boldsymbol{N}$, i.e.

$$\boldsymbol{F} = \boldsymbol{I} + \varepsilon \boldsymbol{D} \tag{1}$$

$$\boldsymbol{n} = \boldsymbol{N} + O(\varepsilon) \tag{2}$$

Here $\boldsymbol{D}$ is an arbitrary deformation, and they assume $\varepsilon \ll 1$. They substitute into the expression for $\Delta \boldsymbol{f}$ to solve for $\Delta \boldsymbol{f}$ as a function of $D$ and $\varepsilon$, and perform a series expansion around $\varepsilon = 0$. Because $\varepsilon$ is assumed small, they disregard all $O(\varepsilon^2)$

terms to produce a function linear with respect to $\varepsilon$

$$\Delta \boldsymbol{f} = \boldsymbol{g}(\boldsymbol{n}) + \varepsilon \boldsymbol{h}(\boldsymbol{n}, \boldsymbol{D}, \lambda_\alpha) \tag{3}$$

Functions $\boldsymbol{g}$ and $\boldsymbol{h}$ incorporate the three-dimensional Young's Modulus as a material parameter. Obviously this linearization is valid only for small deformations. The deformation will be sufficiently small for weak flows, or for capsules with highly viscous interiors. Using the linear model, and considering only initially spherical capsules, Barthès-Biesel and Rallison [4] were able to produce equilibrium solutions, and transient solutions for further simplified cases. Although this model was later extended to incorporate a kinematic membrane viscosity [5], general solutions to the transient capsule deformation problem are too complicated to approach analytically, and thus are best approached numerically.

### 3.1.1 Numerical Methods

As far as we are aware, all previously implemented numerical methods have been low-order methods. Secomb *et al.* [75, 76, 77], for instance, implemented a finite differences method to model axisymmetric erythrocyte deformation in a capillary. They investigated the effects of flow velocity, nonuniform vessel diameter, and the presence of a flow-resistive layer on the vessel wall. Eggleton and Popel [29], on the other hand, used the Immersed Boundary Method (IBM) to study the fully three-dimensional problem of capsule deformation in linear shear flow. They studied capsules with initially spheroidal, oblate spheroidal, and biconcave discoid shapes, and were able to reproduce numerically the tank-treading behavior. One disadvan-

tage of the IBM is that it is necessary to discretize the entire three-dimensional domain in addition to the membrane surface of the capsule.

Unlike the IBM, a method based on the Boundary Integral Equation formulation discussed in Section 1.2 requires discretizing only the two-dimensional interface that represents the surface of the capsule. The application of BIE methods to analyze the deformation of viscous liquid droplets in ambient flow is a classical problem, with extensive examples in the literature. Pozrikidis [66] has written an review article on this subject. The primary difference between liquid droplet versus capsule deformation is the boundary condition at the interface. In the case of a liquid droplet, the interfacial hydrostatic traction $\Delta \boldsymbol{f}$ arises from the surface tension. For a capsule, as previously discussed, it arises from elastic interactions with the membrane.

The simplest BIE methods assume axisymmetry. This allows one to discretize the surface only in the direction of the meridian (one dimension). During evaluation of the surface integral, each point can be weighted by integrating in the azimuthal direction, thus preserving the three-dimensional nature of the problem. The formulation is further simplified by using the axisymmetric form of the membrane statics equations. Diaz *et al.* [22] employed an axisymmetric BIE method to study the transient response of a capsule in ambient flow. They examined the effects of the viscosity ratio and the membrane elasticity. The simplified membrane statics equations made it easier to extend the model to examine the behavior of a viscoelastic membrane [23] and a membrane with bending resistance. They further extended the BIE formulation to model a capsule entering a small pore [24], and to examine

the effects of different elastic constitutive laws [7]. Kwak and Pozrikidis [47] also implemented an axisymmetric BIE method, in order to study the effect of bending stiffness on capsule elongation. Pozrikidis [70] extended this method to model a file of biconcave discoid capsules, representing red blood cells, flowing through a cylindrical tube.

In 1995, Pozrikidis [63] implemented a fully three-dimensional BIE method to study transient capsule deformation in linear shear flow. The membrane is assumed elastic, with a constitutive law derived from a zero-thickness formulation of an incompressible elastic shell. For computational simplicity, he assumes a viscosity ratio of unity, and limits the analysis to spheroid capsules, or slightly oblate spheroid capsules. The surface of the capsule is discretized using curvilinear parameters corresponding to the initial meridian and azimuthal directions. This introduces one singular discretization point at either pole. Evaluating the hydrostatic traction for the BIE formulation, Eq. (4), requires taking the surface divergence of the stress resultant, which normally involves high-order differentiation. Because of the uniform discretization, high-order differentiation would significantly worsen the numerical accuracy. Consequently, Pozrikidis is forced to employ an approximation, in which he replaces the single-layer integral in Eq. (4) with a product of two integrals on each surface element, which are then summed over all elements. The quadrature is a low-order three point Gauss method, which is applied to each surface element. Recall that the Stokeslet solution $\boldsymbol{S}(\boldsymbol{x}_0, \boldsymbol{x})$ is singular around the point $\boldsymbol{x}_0$. Therefore, in the surface integration, he attempts to compensate for the singularity by integrating the elements proximate to $\boldsymbol{x}_0$ using local polar coordinates.

He examines the shear-induced deformation of elastic capsules over a range of capillary numbers, and identifies a critical shear rate above which the method does not converge to a steady state. For lower capillary numbers, his method is also characterized by sawtooth-type instabilities that manifest near steady state. These instabilities can be minimized either by severely reducing the time step, or by employing a 5-point smoothing formula in the azimuthal direction. However, there are certain simulations, including relaxation modeling, in which the instabilities overwhelm the model, and a stable steady state cannot be produced. Further, the trajectory of the overall shape with smoothing applied deviates slightly from the unsmoothed shape, even when the sawtooth instabilities are not an issue. This effect is especially pronounced for coarse grids.

Ramanujan and Pozrikidis [72] reexamined the general three-dimensional problem by implementing an unstructured mesh discretization of the capsule surface. Certainly an improvement over the previous method of Pozrikidis, this discretization involves subdividing the surface of a regular polyhedron into triangles, and projecting these triangular elements radially onto the capsule surface. The result is a nearly isotropic distribution of triangular surface elements. Unlike the structured mesh method, this discretization introduces no singularities. Each triangle consists of 6 nodes, which are mapped onto a parametric right triangle for interpolation and quadrature. Geometric interpolation is then given by a two-dimensional quadratic form. Interpolation of the stress field, however, must be done with a linear form, because the quadratic form appears to cause disparities in tension at non-vertex nodes across surface elements. Again, they desire to avoid high-order numerical differenti-

ation because of the low-order surface discretization, so they employ an estimate of the surface force instead of directly calculating it at each node. The estimate used is to integrate the stresses over a contour around each surface element. Because the forces must be balanced, this can be used to calculate an average hydrostatic traction acting on the entire element, which is used as representative for the element in the surface quadrature. They then use this average force in conjunction with the same form used in the previous method to approximate the single-layer quadrature.

Because in this unstructured mesh description surface elements are not connected, and because the interpolation scheme is low-order, local errors can build between adjacent surface elements. To combat this, quantities like surface strain tensor must be averaged at each node over adjacent elements. They use a 2nd or 3rd order Runge-Kutta-Fehlberg scheme to advance the nodal points in time. Their results reverse the previous findings of Pozrikidis with the structured mesh description regarding the existence of a critical capillary number. Instead, they find that, as shear rate increases, the shape elongates further, with no clear upper limit. They also examine the effects of different viscosity ratios, and non-spherical initial shapes, and they are able to observe tank-treading behavior in shear flow. Pozrikidis [67] later extended this method to study the effects of bending resistance. Navot [58] implemented a similar surface discretization method to study the behavior of an elastic spring-style membrane in shear flow.

The most recent three-dimensional BIE implementation for capsule deformation is that of Lac *et al.* [48]. Like Pozrikidis [63] in 1995, they use a structured mesh description, with azimuthal and meridian curvilinear parameters for the ini-

tial shape. Surface position is represented using bi-cubic B-spline functions. This assures surface continuity up to second order along the interface, but eliminates all high-order surface derivatives. They assume a viscosity ratio $\lambda$ of unity to simplify the BIE formulation, ignore flexural resistance, and use a 4th-order Runge-Kutta scheme to apply the Lagrange material point condition. They account for the Stokeslet singularities by integrating nodes proximate to $\boldsymbol{x}_0$ with parametric polar coordinates.

Of course, this surface representation introduces heterogeneity in surface element size and type, with quadrilateral elements throughout most of the shape, but triangular elements adjacent to the poles, as well as polar discretization singularities. They find that the stability of the method depends upon the initial position of the poles; in shear flow, the method is not stable when the poles are out of the plane of shear. They examine capsule deformation both in shear flow and in planar hyperbolic flow, with several different elastic material constraints. For each material constraint, they identify regions of stability, capillaries numbers where the numerical method converges to a steady state. Outside these regions, instability causes the method to diverge. They further demonstrate that for capillary numbers below the lower stability limit, one of the principal tensions becomes negative, indicating that the capsule is under compression, and buckling can be expected to occur. When the capillary number is above the upper stability limit, they observe the formation of high-curvature tips, and the method is unstable. The method is able to reproduce tank-treading behavior, and produces results in reasonable agreement with the previous study of Ramanujan and Pozrikidis [72].

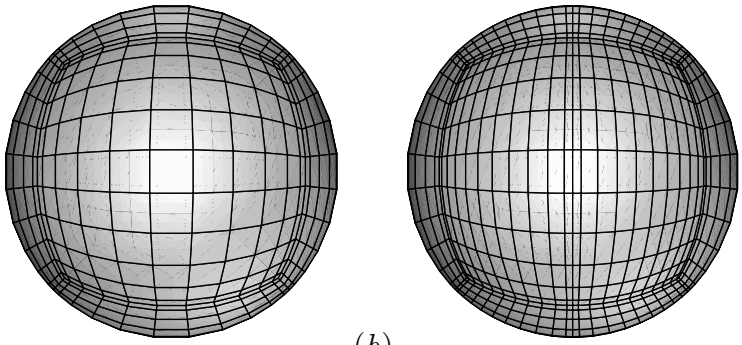

$(a)$ $(b)$

Figure 3.1: The SBE discretization uses a spectral, block-structured mesh. A sphere discretized using (a) $N_E = 6$, or (b) $N_E = 10$ spectral elements. $N_B = 12$ and the spectral points are of type Gauss-Lobatto Legendre.

## 3.2 SBE Discretization and Time Advancement

The Spectral Boundary Element method, previously applied for fixed boundary computations [57, 59], and later for viscous droplet deformation [88], is based on a high-order polynomial interpolation for surface quantities. The discretization used for the SBE is a block-structured mesh, shown for a spherical capsule in Figure 3.1. First, we divide the capsule surface into $N_E$ quadrilateral surface elements. The number of surface elements commonly ranges from 6 to 14. Additional elements can be formed by splitting existing elements. For instance, the 6-element discretization shown in Figure 3.1(a) can be split into the 10-element configuration in Figure 3.1(b). Each surface element is then mapped onto a square parametric domain. Dividing the surface in this way makes calculations involving interpolation more efficient, since the interpolation is only over the element, and not the entire surface. Thus the parameters of the domain become curvilinear coordinates for the

surface. The nodes used to discretize the parametric domain are zeros of orthogonal Jacobi polynomials, such as Legendre or Chebyshev, on the interval [-1,1]. This obtains the exponential convergence properties characteristic of spectral methods. Letting $N_B$ represent the number of points to use in each direction for the parametric domain, we then represent the geometric position, and all functions of geometry like $\Delta \boldsymbol{f}$ and $\boldsymbol{u}$, at each point using Lagrange polynomials.

$$\boldsymbol{x}(\xi, \eta) = \sum_{i=1}^{N_B} \sum_{j=1}^{N_B} \boldsymbol{x}(\xi_i, \eta_j) h_i(\xi) h_j(\eta) \tag{4}$$

Here $h_i(\theta^\alpha)$ represents the $(N_B - 1)$-order Lagrange interpolant polynomial for node $i$ with respect to curvilinear direction $\theta^\alpha$. The derivative in either direction can be computed by simple differentiation of this expression. Second derivatives can easily be calculated through continued differentiation. By adjusting the distribution of surface elements, and the density of spectral points within those elements, we can maximize stability, accuracy, and efficiency.

This discretization results in a total of $N_E N_B^2$ nodes. Nodes at the edges of elements overlap. We will call these nodes coincident points. Because the problem is three-dimensional, there are a total of $3N_E N_B^2$ unknown quantities in the Boundary Integral Equation (4). The result is a linear system of dimension $3N_E N_B^2$.

$$\boldsymbol{u} - c\boldsymbol{u}^\infty = \boldsymbol{A} \cdot \Delta \boldsymbol{f} + \boldsymbol{B} \cdot \boldsymbol{u} \tag{5}$$

The BIE equation incorporates the geometry both as the points where the BIE holds $\boldsymbol{x}_0$, which we call collocation points, and at the points involved in the integration where $\boldsymbol{u}$ and $\Delta \boldsymbol{f}$ are defined. The latter class we call basis points. The collocation points are of type Gauss-Legendre, which are entirely interior, and the

basis points are of type Gauss-Lobatto, which include the exterior endpoints. The matrices $\boldsymbol{A}$ and $\boldsymbol{B}$ are calculated by Gauss-Legendre quadrature from the Stokes flow singularity solutions using variable transformations as described by Muldowney and Higdon [57]. Eq. 5 can be solved for either $\boldsymbol{u}$ or $\Delta\boldsymbol{f}$. The kinematic condition (Eq. 7) can be evaluated using any explicit or implicit time solution method, which is applied at the basis points. We have chosen to use a 4th-order Runge-Kutta method. The time step should be small enough to satisfy the stability condition.

$$\Delta t < O(Ca\,\Delta x_{min}) \tag{6}$$

Here $\Delta x_{min}$ is the smallest length scale in the problem, e.g. the minimum grid spacing [88, 67].

Implementing the Spectral Boundary Element method for capsules has required the following additions to the droplet deformation method: 1) building a differential geometry toolkit for tensor manipulation, covariant derivatives, etc., 2) creating a stored reference geometry, which must map each node to the current shape at every point in time, 3) replacing the surface tension interfacial boundary condition, $\Delta\boldsymbol{f} = \gamma(\nabla\cdot\boldsymbol{n})\boldsymbol{n}$, with one based on membrane statics from Section 2.1, and 4) implementing a smoothing scheme that preserves continuous correspondence with the reference shape.

## 3.3 A Smoothing Algorithm for Elastic Interfaces

Applying the algorithm described in Section 3.2, even when requiring 0-order continuity between adjacent elements, the resulting method is unstable. This insta-

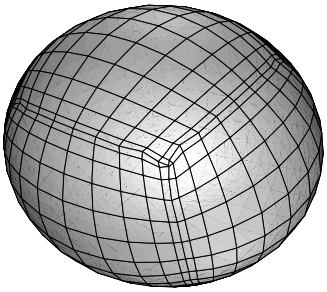

Figure 3.2: Interfacial shape of an initially spherical Skalak capsule with $C = 1$ in a planar extensional flow with $Ca = 0.35$ at time $t = 0.123$. Zero-order continuity at the edges of adjacent elements was enforced. For this specific case, the disparities in the derivatives of the geometry near the elements corners cause interfacial breaking at the next time step. Attempting to use the first-order smoothing of Wang and Dimitrakopoulos [88] produces similar instability. ($N_E = 6$, $N_B = 12$ and $\Delta t = 10^{-3}$)

bility first manifests as high-curvature tips located at element corners, as illustrated for an initially spherical capsule in moderate planar extensional flow by Figure 3.2. It quickly causes failure of the numerical method. The source of the instability is derivative discontinuities along element edges. Because the surface elements used in the SBE are unconnected, there will be a small discrepancy in the derivatives at coincident points after each time advancement step. Wang and Dimitrakopoulos [88] observed a similar instability with their SBE method for viscous droplets. The error associated with each time step is several orders of magnitude smaller than the accuracy of the numerical method. Therefore, as long as they are not allowed to build over time, these errors do not affect the overall accuracy of the numerical method, or the exponential convergence properties (see Section 3.4.2).

Wang and Dimitrakopoulos [88] developed a 1st-order geometric smoothing algorithm to control this instability. However, when we attempt to use the droplet smoothing method with an elastic interface, instabilities similar to those shown in Figure 3.2 still occur. The droplet method of smoothing is insufficient for capsules because, as discussed in Section 1.2, the points for a droplet are only marker points, while the points for a capsule represent real material points, and therefore convect with the entire fluid velocity, not only the normal component [72]. Further, the forces in the case of the droplet derive solely from the current deformed geometry, while the capsule forces derive from a correspondence between the current and the elastic reference geometries. Consequently, we have developed a new 1st-order smoothing algorithm specifically for the SBE with elastic interfaces, which generates a smooth geometry by maintaining continuous correspondence with the reference shape. Our

smoothing algorithm consists of geometric smoothing after each time advancement, and also smoothing of the surface force vectors during assembly of the BIE system.

The first step is to average the position $\boldsymbol{x}$ of coincident nodes for all sets of coincident points. The result is a geometry continuous at element edges. Let $\boldsymbol{x}^{[1]}$ and $\boldsymbol{x}^{[2]}$ be the non-smoothed geometric position for two coincident nodes, determined through explicit time integration at the Gauss-Lobatto basis points for time $t + \Delta t$. Then the new geometry can be calculated

$$\boldsymbol{x}^{[1]}_{new} = \boldsymbol{x}^{[2]}_{new} = \frac{1}{2}(\boldsymbol{x}^{[1]} + \boldsymbol{x}^{[2]}) \tag{7}$$

This produces 0-order continuity at this pair of coincident points. We then use $\boldsymbol{x}_{new}$ to calculate new geometric derivative values. Note that this also results in high-order continuity between elements in the direction along the edge, which coincides with one of the curvilinear directions. The only remaining task to produce complete 1st-order continuity is to smooth in the other curvilinear direction. Unlike Wang and Dimitrakopoulos, we use as the basis for our 1st-order smoothing a tensor quantity, the surface strain tensor $\boldsymbol{A}$ (see Section 2.1), which relates the deformed to the reference shape. We average this tensor over coincident nodes (The [1] and [2] indices now refer to the 0-order continuous geometry).

$$(\boldsymbol{A})_{new} \equiv \frac{1}{2}((\boldsymbol{t}_\alpha \boldsymbol{T}^\alpha)^{[1]} + (\boldsymbol{t}_\alpha \boldsymbol{T}^\alpha)^{[2]}) \tag{8}$$

Note that, because the reference shape is time invariant, the reference tangents $\boldsymbol{T}_\alpha$ have high-order continuity across elements. We then use $(\boldsymbol{A})_{new}$ to obtain new tangent vectors.

$$\left(\frac{\partial \boldsymbol{x}}{\partial \theta^\alpha}\right)_{new} = (\boldsymbol{t}_\alpha)_{new} \equiv (\boldsymbol{A})_{new} \cdot \boldsymbol{T}_\alpha \tag{9}$$

It is then necessary to generate a new geometry that preserves 0-order continuity, but incorporates the new derivative values we desire at the coincident points. This is accomplished by a two-dimensional Hermite-like interpolation, as in Wang and Dimitrakopoulos [88]. In practice, the two-dimensional interpolation consists of two one-dimensional interpolations, and it is easiest to evaluate each one-dimensional interpolation (each curvilinear direction) separately. In each direction $\theta^\alpha$ then, the problem can be stated thus: generate a new set of geometric Lobatto points satisfying the new endpoint conditions but with the same overall geometry as the unsmoothed shape. Obviously, we cannot generate a new set of $N_B$ points satisfying the new derivative conditions, 0-order continuity at the endpoints, and the $N_B$ point conditions; the system is over-defined. Therefore, we interpolate to $N_B - 4$ interior Jacobi points. Combined with the position and derivative constraints at the two endpoints, we have $N_B$ degrees of freedom, enough to generate a new set of $N_B$ geometric Lobatto points. Letting $N_J$ be the number of Jacobi points ($N_B - 4$), the following interpolation expression is used in each direction.

$$\begin{aligned}
\boldsymbol{x}(\xi) = (\xi^2-1)^2 \sum_{i=1}^{N_J} \frac{1}{(\xi_i^2-1)^2} \prod_{j\neq i}^{N_J} \left(\frac{\xi-\xi_j}{\xi_i-\xi_j}\right) \boldsymbol{x}(\xi_i) + \\
\prod_{j=1}^{N_J} \left(\frac{\xi-\xi_j}{-1-\xi_j}\right) \frac{(\xi-1)^2}{4}(\xi+1) \left.\frac{\partial \boldsymbol{x}}{\partial \xi}\right|_{\xi=-1} \\
\prod_{j=1}^{N_J} \left(\frac{\xi-\xi_j}{1-\xi_j}\right) \frac{(\xi+1)^2}{4}(\xi-1) \left.\frac{\partial \boldsymbol{x}}{\partial \xi}\right|_{\xi=+1} \\
\prod_{j=1}^{N_J} \left(\frac{\xi-\xi_j}{-1-\xi_j}\right) \frac{(\xi-1)^2}{4}[1+b_{(-1)}(\xi+1)]\boldsymbol{x}(-1) + \\
\prod_{j=1}^{N_J} \left(\frac{\xi-\xi_j}{1-\xi_j}\right) \frac{(\xi+1)^2}{4}[1-b_{(+1)}(\xi-1)]\boldsymbol{x}(+1)
\end{aligned} \tag{10}$$

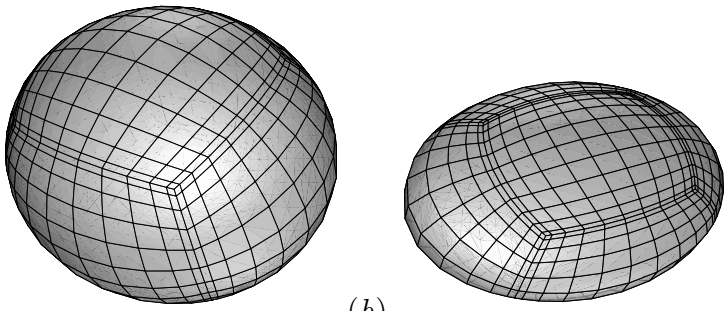

$(a)$ $(b)$

Figure 3.3: Interfacial shape of a capsule with the same parameters as in Figure 3.2 at (a) $t = 0.123$, and (b) $t = 10$ (i.e. well past equilibrium), using our first-order capsule interfacial smoothing. The capsule interface is continuous and smooth across the spectral elements at all times.

In this expression, $\xi_i$ are the Jacobi points. The values $\pm 1$ applied to $\boldsymbol{x}$ and its first derivative are the endpoint values from the domain $[-1, 1]$. In the context of the discretization, they represent the edges of surface elements, which are the coincident nodes. $b_{(\pm 1)}$ are coefficients chosen such that the terms containing $b_{(\pm 1)}$ make no contribution to the endpoint derivative.

$$b_{(\pm 1)} = \sum_{j=1}^{N_J} \left( \frac{1}{1 \mp x_j} \right) + 1 \tag{11}$$

Applying this smoothing scheme after each time step suppresses the numerical instabilities resulting from the disconnect between surface elements.

We have discovered that smoothing the calculated force vector $\Delta \boldsymbol{f}$ in addition to geometry confers additional stability, allowing us to employ a slightly larger time step in the simulation. This 1st-order force-smoothing algorithm is applied just before entering the force vector into the BIE system. The smoothing mirrors the

geometric smoothing, except the interpolated function is $\Delta \boldsymbol{f}$ instead of $\boldsymbol{x}$, and the tensor used for the 1st-order smoothing is the surface gradient $\nabla_S \Delta \boldsymbol{f}$.

$$\nabla_S(\Delta \boldsymbol{f}) = \boldsymbol{t}^\alpha \frac{\partial(\Delta \boldsymbol{f})}{\partial \theta^\alpha} \tag{12}$$

We average $\nabla_S(\Delta \boldsymbol{f})$ at coincident points. The updated derivatives of $\Delta \boldsymbol{f}$ can easily be recovered from the new surface gradient.

$$(\boldsymbol{t}_\beta)_{new} \cdot (\nabla_S(\Delta \boldsymbol{f}))_{new} = \delta_\beta{}^\alpha \frac{\partial(\Delta \boldsymbol{f})}{\partial \theta^\alpha} \equiv \left( \frac{\partial(\Delta \boldsymbol{f})}{\partial \theta^\beta} \right)_{new} \tag{13}$$

The same formula previously used for Hermite interpolation of geometry can then be used to generate a new distribution of force vectors across the capsule surface that is 1st-order continuous across elements. This updated set of force vectors is then used to construct the BIE system.

The membrane smoothing algorithm presented here generates a smooth geometric for the interfacial dynamics problem of an elastic interface, and suppresses the instability observed in Figure 3.2. Figure 3.3(a) shows that the simulation, using the same parameters as in Figure 3.2 and displayed at the time when the numerical methods fails without smoothing, displays no instability when smoothing is employed. Further, the simulation is stable over long (past equilibrium) times, as shown in Figure 3.3(b). This methodology is an efficient technique to preserve the continuity of the interfacial spectral geometry. The entire process, including the relevant two-dimensional Hermitian interpolation, requires a computational cost of only $O(N_E\, N_B)$, i.e. $O(N_B)$ on each spectral element, owing to the fact that it is implemented through products of one-dimensional rules.

It is also important to note that the smoothing methodology introduces negligible error since the discrepancies at the edges of the spectral elements are several orders of magnitude smaller than the accuracy of the numerical method when treated at the end of each time step. In addition, owing to the fact that in these interpolations we employ high-order orthogonal polynomials, the loss of accuracy from one to the other discretization is negligible. By implementing the smoothing scheme after we determine the (temporary) interfacial shape at the desired time $t + \Delta t$, we have the advantage of avoiding incorporating a smoothing technique inside the spectral element algorithm for the solution of the corresponding boundary integral equation. Most importantly, our smoothing methodology preserves the main characteristic of the spectral methods, i.e. the exponential convergence in the interfacial accuracy with increasing number of spectral points as discussed in section 3.4.2 below.

## 3.4 Properties of the SBE Methodology

In this chapter, we investigate the deformation of initially spherical capsules in moderate ambient flow, in order to validate the SBE method and evaluate its properties. The flows we have examined include linear shear flow, in which $\boldsymbol{u}^{\infty} = G(z, 0, 0)$ (see Figure 1.1), and planar extensional flow, in which $\boldsymbol{u}^{\infty} = G(x, -y, 0)$ (see Figure 4.1). We have conducted numerous tests to verify the correctness, accuracy and robustness of our interfacial algorithm for capsules with elastic tensions. We have also considered all material laws mentioned in Section 2.2.1. While we have examined the behavior of capsules with different viscosity ratios, in this chapter, we

present results only for $\lambda = 1$, so that we can compare our findings with those from earlier studies [29, 48]. The accuracy of our results was verified by employing different space discretizations (i.e. $N_E = 6, 10, 14$ spectral elements with $N_B = 8 - 14$ basis points) and several times steps in the range $\Delta t = 10^{-4} - 10^{-3}$.

To quantify the interfacial deformation over time we monitor the capsule semi-axis lengths, in order of ascending magnitude $S$, $W$, and $L$. These capsule dimensions are calculated from the inertia tensor [48, 72]. For deformations resulting in an ellipsoidal geometry, the lengths calculated from the inertia tensor are equal to the real semi-axis lengths. We also calculate Taylor's deformation parameter

$$D = \frac{L - S}{L + S} \tag{14}$$

### 3.4.1 Validation by Comparison with Previous Methods

Figure 3.4(a) shows the deformation of an initially spherical Neohookean capsule in a shear flow for $Ca = 0.6$, a moderate capillary number. $L$, $S$, $W$, and $D$, are shown as a function of time. After the initiation of the flow, the capsule's length $L$ increases with time while its width $S$ decreases. $W$ increases marginally. The cross-section undergoes continuous transformation from circular to ellipsoidal, as seen in Figure 3.4(b). Figure 3.4(c) shows a three-dimensional image of the equilibrium geometry, and it appears as a flat ellipsoidal shape.

We note that our results for the evolution of the capsule's deformation $D$ shown in Figure 3.4(a) are in excellent agreement with results from the Immersed Boundary Method of Eggleton and Popel [29] reported in their Figure 2, and with

those from Lac *et al.* [48] reported in their Figure 3.

The tank-treading behavior discussed in Chapter 1 that capsules undergo in shear flow is reproduced with the SBE method, and can be observed in Figure 3.5, for the evolution of the shape of a Neohookean capsule for the same parameters as the ones used in Figure 3.4. The material points of the membrane rotate around the capsule shape. Note that, for the initial capsule shape, we use the geometry shown in Figure 3.1(b) where the two rows of four spectral elements are defined along the flow direction. The capsule shape is presented in the time interval $[0, 20]$ and plotted row-wise every 2 time units. As this figure reveals, in this time interval the membrane has completed one full circumvolution.

As discussed later in Section 3.5, our results for a Skalak capsule in a planar extensional flow at moderate capillary numbers $Ca$ are also in excellent agreement with earlier computations [48].

### 3.4.2 Spectral Convergence

Having established the validity and robustness of our interfacial algorithm with the representative examples mentioned above, we proceed now to discuss its spectral performance. In particular, a major property of our interfacial algorithm is its exponential convergence in the numerical accuracy with increasing the number of discretization points which results from the spectral nature of our algorithm. Our methodology preserves the exponential convergence both for the geometric properties of a given shape, such as the interfacial curvature, and for the dynamic evolution

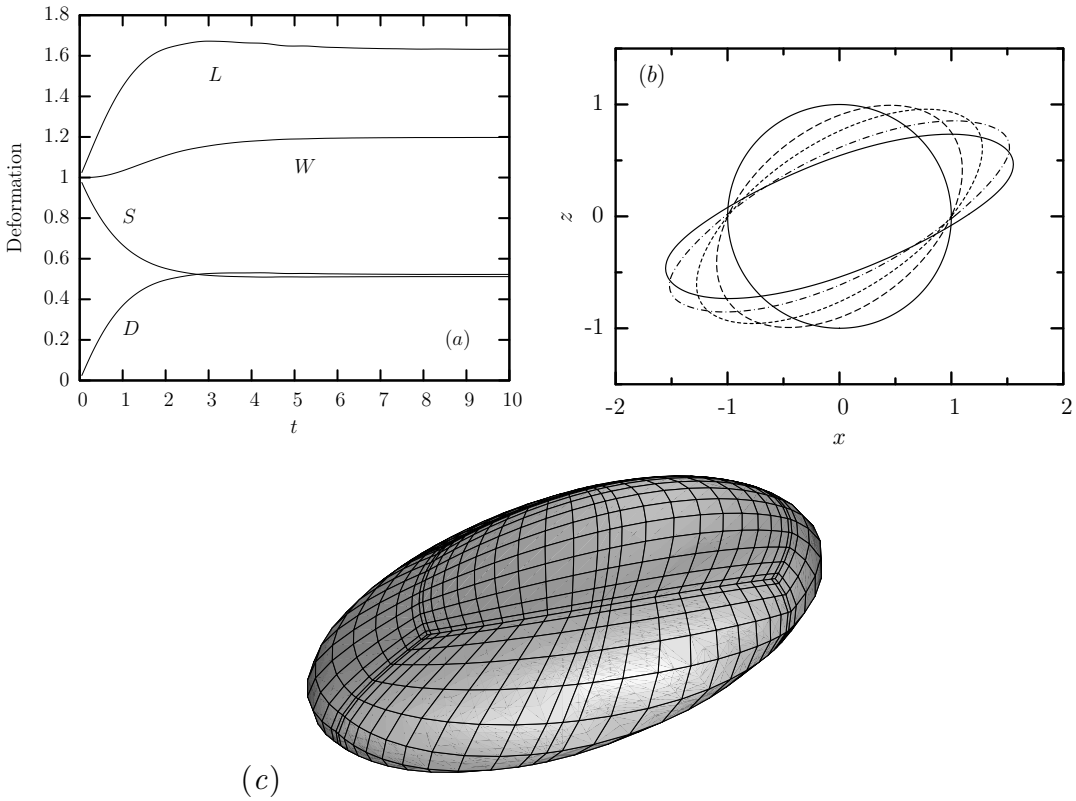


Figure 3.4: The evolution of a Neohookean capsule with $\lambda = 1$ in a shear flow for $Ca = 0.6$. (a) The Taylor deformation $D$, length $L$, width $S$ and depth $W$, shown as a function of time. (b) The cross section with the plane $y = 0$ at times $t = 0, 0.5, 1, 2, 20$. (c) Capsule shape at equilibrium ($t = 10$). The transient evolution of the capsule's deformation $D$ is in excellent agreement with the numerical results of Eggleton and Popel [29] reported in their Figure 2, and with those by Lac *et al.* [48] reported in their Figure 3.

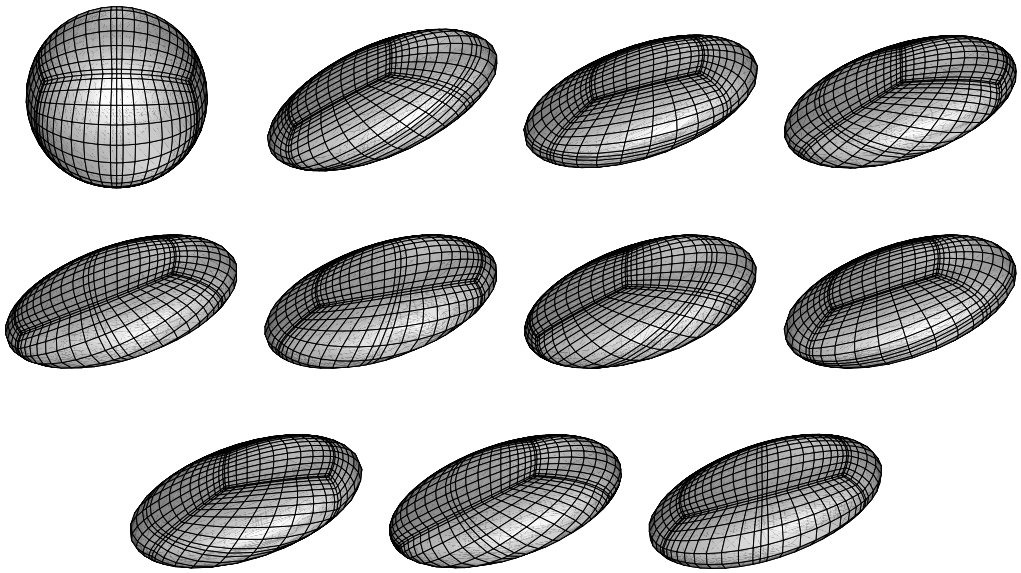

Figure 3.5: A Neohookean capsule in a simple shear flow. The capsule's shape is presented in the time interval $[0, 20]$ and plotted row-wise every 2 time units. The membrane tank-treads around the interior. ($\lambda = 1$, $Ca = 0.6$)

of the capsule's shape. (Note that due to the explicit time integration, the required small time step makes the error associated with the time discretization much smaller than the error associated with the space discretization.)

Figure 3.6 shows the maximum absolute error in the computed curvature as the number of spectral points $N$ increases from 150 to 3750 for a spherical capsule and two representative lamellar capsules. The exponential convergence of our spectral algorithm is in direct contrast to the common linear or quadratic convergence associated with low-order algorithms.

To illustrate the spectral convergence in determining the interfacial shape, we calculated the transient evolution of an initially spherical capsule for a moderate and a large capillary number, i.e. $Ca = 0.35, 1.5$. In both cases, we kept the number of elements $N_E$ fixed and increased the number of basis points in the range $N_B = 6 - 15$. Our results for $N_B = 15$ were regarded as a close approximation for the exact answer. Figure 3.7 shows the exponential convergence in determining the capsule's deformation $D$ as the number of spectral points $N = N_E\, N_B^2$ increases. We note that our results for $Ca = 0.35$ represent the time $t = 0.15$ where $D \approx 0.14$ to illustrate the spectral convergence at small deformations. For $Ca = 1.50$, our results represent the time $t = 0.60$ where $D \approx 0.49$, i.e. they demonstrate the spectral convergence for large deformations. (In both cases, the capsule has not reached a steady-state.) The observed spectral convergence in determining the interfacial shape with our present membrane algorithm is similar to that found for drop dynamics in Wang and Dimitrakopoulos [88]. This spectral convergence shows the success of our smoothing scheme which as discussed in Section 3.3 causes negligible

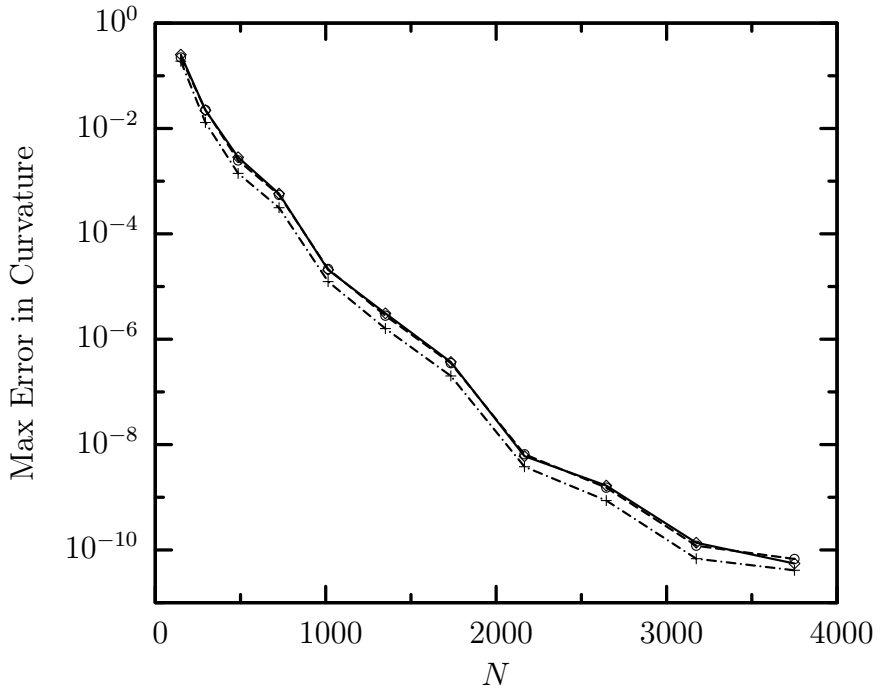


Figure 3.6: Maximum absolute error on the surface for curvature computed by SBE as a function of the number of spectral points $N = N_E\, N_B^2$ for a sphere (——) and different lamellar ellipsoids: ----, $a = 2, b = 1, c = 0.5$; $-\cdot-$, $a = 4, b = 1, c = 0.25$ (where $a$, $b$ and $c$ are the semi-axes of the ellipsoids). The exponential convergence shown in this figure was generated by employing $N_E = 6$ spectral elements and varying the number of basis points $N_B$ from 5 to 25. The analytic curvature was used to determine the numerical error.

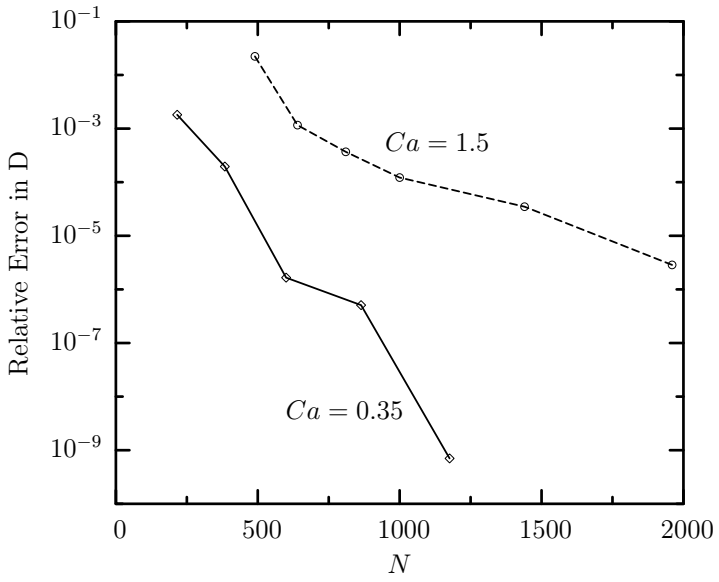


Figure 3.7: Relative error in the computed deformation $D$ versus the number of spectral points $N = N_E N_B^2$ for a Skalak capsule ($C = 1$ and $\lambda = 1$) in a planar extensional flow for $Ca = 0.35$ and $Ca = 1.5$. For $Ca = 0.35$, our results represent the time $t = 0.15$ where $D \approx 0.14$. Here the capsule length has increased by 15% and its width has been decreased by 13%, so this case is representative of small deformations. For $Ca = 1.5$, our results represent the time $t = 0.60$ where $D \approx 0.49$. Here the capsule length has been increased by 71% and its width has been decreased by 41%, representative of large deformations. The exponential convergence shown was generated by employing $N_E = 6$ spectral elements for $Ca = 0.35$ and $N_E = 10$ elements for $Ca = 1.5$, and varying the number of basis points $N_B$ from 6 to 15. In both cases, the results for $N_B = 15$ were used to approximate the numerical error.

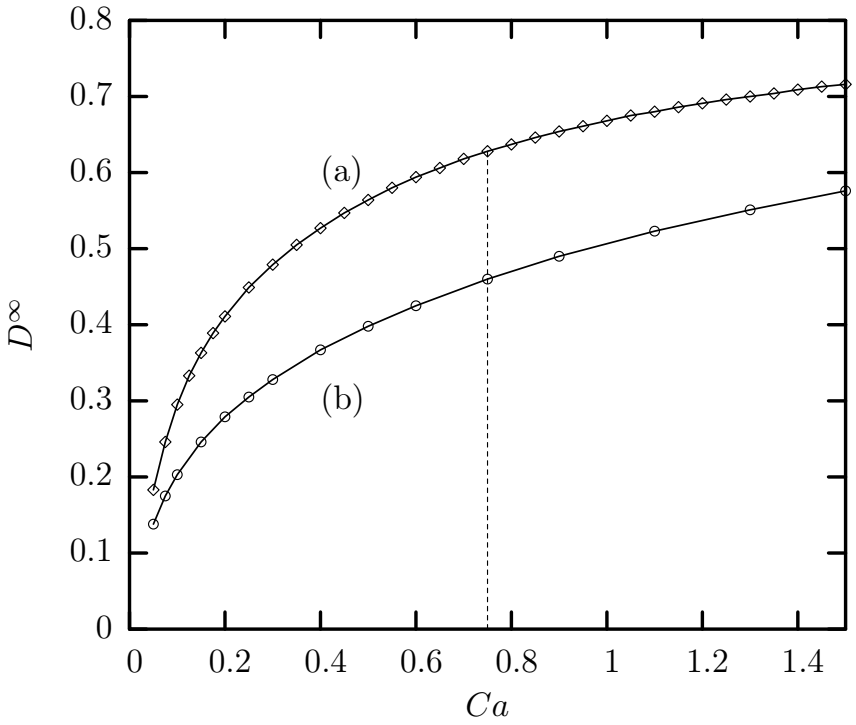


Figure 3.8: $D$ shown as a function of capillary number over a range of low, moderate, and strong flow rates for a Skalak capsule with (a) $C = 1$ or (b) $C = 10$. The data are consistent with the results of Lac *et al.* [48] for the range of capillary numbers shown in their Figure 20 using bi-cubic splines. The dotted line indicates the upper stability limit for the bi-cubic spline method for $C = 1$.

interfacial perturbation. Due to its spectral nature, a fewer number of discretization points may be required for our high-order method to achieve a sufficient accuracy, compared to those required with low-order algorithms.

## 3.5 Robustness of the SBE Method

At higher capillary numbers, previous numerical methods produce divergent results. In particular, the early work of Pozrikidis [63], based on curvilinear discretization along the meridian and azimuthal directions of the capsule surface, found a critical shear rate above which the method does not converge to a steady state. This conclusion was later revoked by Ramanujan and Pozrikidis [72] who, by implementing an unstructured mesh discretization of the capsule surface based on low-order triangular elements, predicted a monotonic increase of the equilibrium deformation with the capillary number and thus no critical flow rate. The recent study of Lac *et al.* [48], which was based on bi-cubic B-spline interfacial interpolation, found a region of moderate capillary numbers outside of which the capsule does not reach steady-state. The authors justified the contradiction of their results with those from Ramanujan and Pozrikidis [72] because the latter study employed an unstructured mesh which requires the usage of approximations (e.g. load averaging over each triangular element) for the determination of the membrane' stresses which may eliminate potential instabilities.

We emphasize that the earlier investigations (as well as the current study) are based on the boundary integral formulation. An exception is the work of Eggleton and Popel [29] who employed an immersed boundary method to study capsule deformation in shear flow; the behavior of this methodology is unclear since the authors studied the interfacial deformation for small to moderate capillary numbers over relatively short time periods.

The bi-cubic B-spline methodology of Lac *et al.* [48] predicts that, for a Skalak capsule with $C = 1$ and $\lambda = 1$ in a planar extensional flow, equilibrium shapes can only be found for capillary numbers $Ca$ in the range $[Ca_L, Ca_H]$ where $Ca_L = 0.15$ and $0.6 < Ca_H < 0.75$. (See Table 1 in that earlier study.) Figure 3.8 shows our results for planar extensional flow for a range of moderate to high capillary numbers both for a Skalak capsule with $\lambda = 1$ and either $C = 1$ or $C = 10$. Our results agree with those of Lac *et al.* [48] in their region of stability, i.e. for moderate capillary numbers. Yet, the SBE method produces stable results, which do not undergo continuous extension or exhibit numerical instability, even above the upper stability limit of Lac *et al.* (indicated by the dotted line on Figure 3.8 for $C = 1$). The SBE method, because it is able to resolve all geometric quantities, including curvature, accurately, is more robust, and extends the possible set of capillary numbers that can be studied numerically. In fact, it reveals novel physical behavior at high capillary numbers, which will be the subject of Chapter 4.

## 3.6 Conclusions Regarding the SBE Method

We have developed a Spectral Boundary Element algorithm for interfacial dynamics in Stokes flow of three-dimensional elastic capsules with shearing and area-dilatation tensions. To produce a stable method and preserve the continuity of the interfacial geometry and its derivatives at the edges of the spectral elements during the interfacial deformation, a suitable interfacial smoothing based on a Hermitian-like interpolation has been developed which preserves the correspondence between

the reference shape and the deformed geometry of the capsule. The smoothing methodology is applied both to the interfacial geometry as well as the surface forces.

Our interfacial spectral boundary element algorithm preserves the main characteristic of the spectral methods, i.e. the exponential convergence in the interfacial accuracy as the number of spectral points increases. However, it avoids creating a large dense system as spectral methods used in volume discretization do. The accuracy of the method and the associated exponential convergence have been demonstrated for the calculation of the geometric properties of a fixed-boundary interface, such as the interfacial curvature, as well as the dynamic evolution of the interfacial shape.

Our numerical results for capsules obeying different membrane laws in shear and planar extensional flows at moderate capillary numbers are consistent with those of earlier methodologies. However, at higher flow rates, our spectral algorithm predicts stable transient and steady-state capsule shapes in contrast to earlier low-order methodologies which predict interfacial breaking.

The present algorithm constitutes a new approach for membrane deformation in Stokes flow based on the (high-order) spectral boundary element formulation which in the near past has demonstrated its high accuracy, robustness and efficiency for fixed boundary surfaces [42, 57, 59], particulate flows [65], equilibrium droplet interfaces under steady flows and/or gravity [25, 26] as well as for the transient droplet evolution [88]. With respect to existing low-order methodologies, our spectral boundary element method for membrane dynamics has the significant advantage of the accurate determination of any interfacial property (including geo-

metric derivatives and membrane tensions) due to its spectral nature. As discussed in Chapter 4, we believe that this is an important issue for the correct and accurate determination of complicated membrane shapes. These characteristics along with the excellent performance of our spectral method for surfaces in close contact (which has been well demonstrated in Muldowney and Higdon [57]) show that our capsule spectral boundary element algorithm is well suited for a wide range of interfacial problems in physiological systems and microfluidic devices.

# Chapter 4

# Capsule Deformation in Planar Extensional Flow

In this chapter we consider in greater detail the deformation of a Skalak capsule with $C = 1$ in a planar extensional flow $\boldsymbol{u}^{\infty} = G\,(x, -y, 0)$ for moderate and large capillary numbers. The flow pattern is illustrated in Figure 4.1. The goal is to use the SBE method to investigate the physical behavior of elastic capsules including the evolution of the interfacial shape and the membrane tensions. We also compare our results with earlier computational and experimental findings.

As discussed previously in Section 3.5, there remains considerable uncertainty regarding the behavior of elastic capsules extended in strong or very strong flows. Ramanujan and Pozrikidis [72] predicted a monotonic increase of the equilibrium deformation with the capillary number, with smooth equilibrium shapes and no upper limit. Lac *et al.* [48], using a method based on bi-cubic B-spline interfacial interpolation, avoided load averaging as in Ramanujan and Pozrikidis [72], but found a critical shear rate above which the method could not obtain a steady-state solution. Navot [58] found results similar to Ramanujan and Pozrikidis [72], but used an elastic law with questionable basis in physical reality.

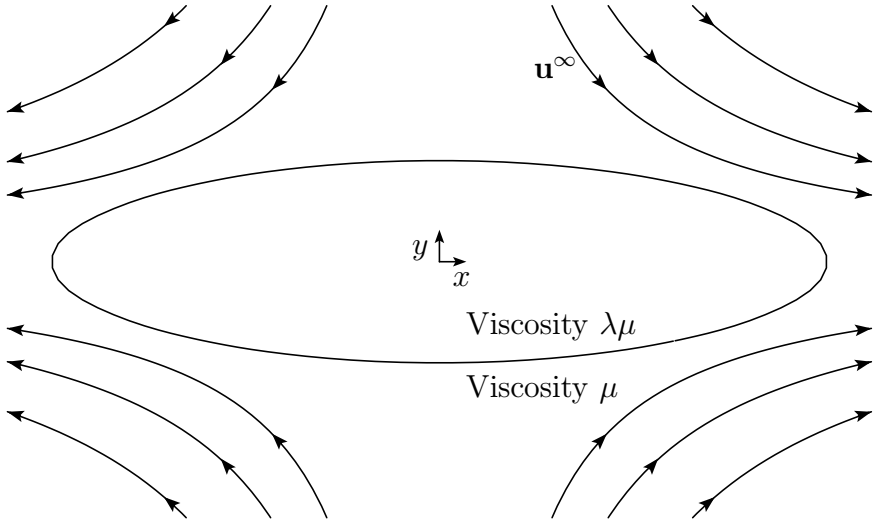


Figure 4.1: A capsule with internal viscosity $\lambda\mu$ suspended in an ambient fluid with viscosity $\mu$ extended in planar extensional flow. The undisturbed fluid velocity field $\boldsymbol{u}^\infty = G(x, -y, 0)$ is shown around the deformed capsule.

To contribute to the physical understanding in this area, we utilize our interfacial spectral boundary element algorithm for capsules with elastic tensions presented in Chapter 3 to study large deformations, in a planar extensional Stokes flow, of a capsule whose membrane follows the Skalak constitutive law, with $C = 1$. This strain-hardening law accounts for both shearing and area-dilation, and while originally developed to describe biological membranes (such that of the erythrocyte) [80], it can also be employed to model membranes obtained by interfacial polymerization [7]. Our high-order, spectrally-accurate computational methodology predicts stable equilibrium shapes whose edges become rounded, spindled and finally cusped with increasing flow rate, in excellent agreement with experimental findings. The transition from concave to convex edges results from the transition of the tensions at the capsule edges from tensile to compressive. In addition, our study shows that there

is a range of high flow rates where both spindled and cusped equilibrium shapes exist; this bifurcation is found by implementing different transient processes to reach equilibrium.

## 4.1 Moderate to Moderately-High Planar Extensional Flow

We begin by examining the deformation of Skalak capsules with $C = 1$ and $\lambda = 1$ in planar extensional flow for a range of moderate to moderately strong flows, beyond the stability limit of the bi-cubic B-spline method of Lac *et al.* [48]. Throughout this chapter, we employ simulation parameters $N_B = 12$ and $\Delta t = 10^{-4} - 10^{-3}$. The number of surface elements $N_E$ is 6 for $Ca < 0.75$, 10 for $0.75 \leq Ca \leq 1$, and 14 for $Ca > 1$.

### 4.1.1 Lengths and Overall Deformation

Figure 4.2(a) shows the deformation $D$ for a Skalak capsule in a planar extensional flow for several capillary numbers ranging from moderate to strong flows. As $Ca$ increases, the capsule's length $L$ increases while its width $S$ decreases as shown in Figure 4.2(b); this results in a monotonic increase of the capsule's deformation $D$ at equilibrium with the capillary number as seen in Figure 4.2(a). A careful examination of Figures 4.2(a) and (b) reveals that while the capsule's width $S$ reaches equilibrium at about the same time for all the flow rates (or $Ca$) studied here, it takes more time for the capsule's length $L$ (and thus for its deformation $D$), to reach equilibrium for the high capillary numbers $Ca = 0.9, 1.1$. (This is the reason that

in this figure we monitor the capsule evolution up to time $t = 18$.)

To explain this anisotropy, in Figure 4.2(c) we present the evolution of the capsule's depth $W$ for the same capillary numbers. At low flow rates (e.g. $Ca = 0.15, 0.25, 0.45$), the capsule's depth $W$ shows a monotonic increase with time, reaching equilibrium at about the same time as the other two dimensions of the capsule. (Observe that $W$ shows a transient maximum even in this range of flow rates.) However, the time evolution of the capsule's depth $W$ is quite different at the large flow rates $Ca = 0.9, 1.1$; after a fast initial growth, $W$ decreases over time, while at equilibrium the higher capillary numbers correspond to smaller depth $W$. This non-trivial behavior of the capsule's depth $W$ affects mostly its length $L$, i.e. the late-time reduction of the depth $W$ at high flow rates causes a further increase of its length $L$.

### 4.1.2 Capsule Profile and Geometry

The evolution of the capsule's profile in the $y = 0$ and $z = 0$ planes for $Ca = 0.45$ is shown in Figure 4.3(a,b). As the capsule deforms, the increase of its length $L$ along with the corresponding decrease of its width $S$, shown in Figure 4.2(b), results in a rather elongated shape in the $z = 0$ plane as depicted in Figure 4.3(a). However, at the same time the capsule's depth $W$ is slightly increased as shown in Figures 4.2(c) and 4.3(b). Both actions results in a flat elliptical (i.e. lamellar) shape of the capsule at equilibrium as seen in Figure 4.3(c).

These results for the evolution of the capsule's deformation $D$ for the moderate

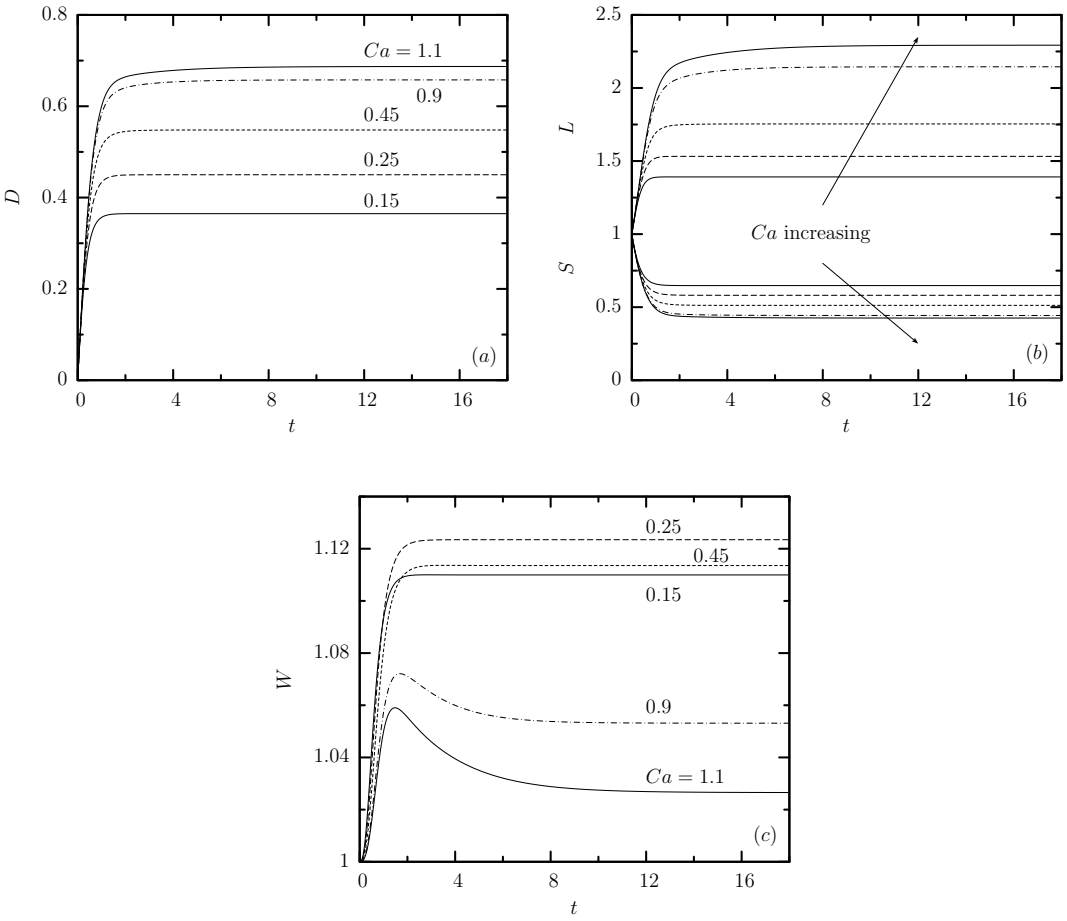


Figure 4.2: Evolution of a Skalak capsule with $C = 1$ in a planar extensional flow for capillary number $Ca = 0.15, 0.25, 0.45, 0.90, 1.1$. Time evolution of the capsule's (a) deformation $D$, (b) length $L$ and width $S$, and (c) depth $W$. The results for $D$ for $Ca = 0.45$ are in excellent agreement with the results of Lac *et al.* [48] reported in their Figure 16.

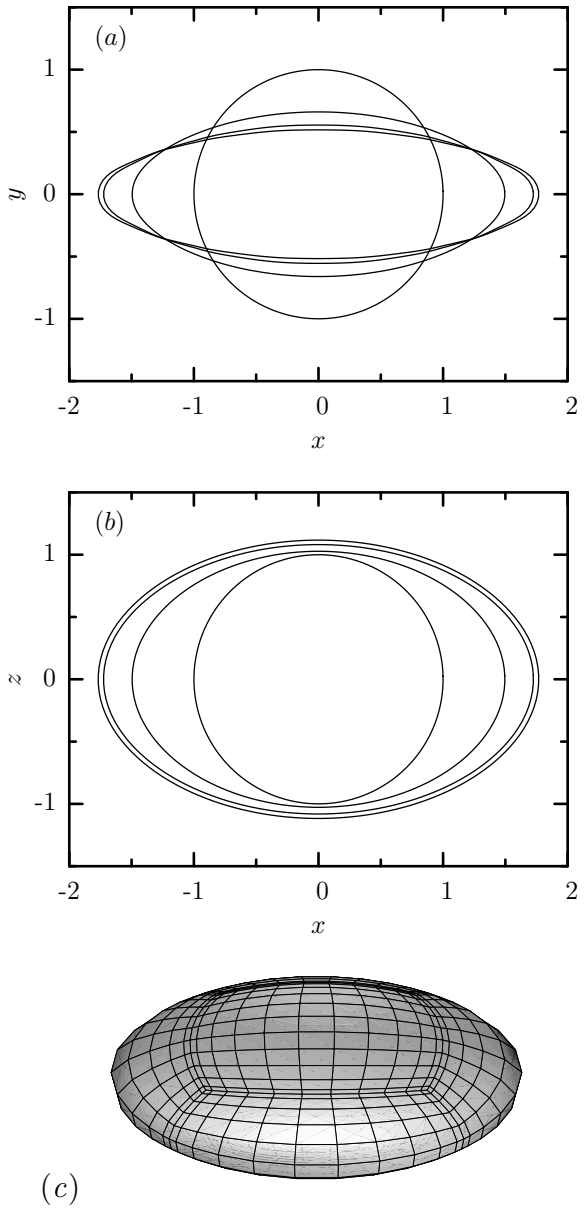


Figure 4.3: Evolution of a Skalak capsule with $C = 1$ in a planar extensional flow with $Ca = 0.45$. (a) Capsule cross-section with the plane $z = 0$ at times $t = 0, 0.5, 1, 18$. (b) Capsule cross-section with the plane $y = 0$ at times $t = 0, 0.5, 1, 18$. (c) Capsule shape at time $t = 18$, i.e. well past equilibrium.

capillary number $Ca = 0.45$ shown in Figure 4.2(a) are in excellent agreement with the computations of Lac *et al.* [48] reported in their Figure 16. In addition, the capsule profile in the plane $z = 0$ at equilibrium shown in Figure 4.3(a) is in excellent agreement with that from the study of Lac *et al.* [48] reported in their Figure 17. However, as discussed in Section 3.5, the bi-cubic B-spline methodology of Lac *et al.* [48] predicts that, for a Skalak capsule with $C = 1$ and $\lambda = 1$ in a planar extensional flow, equilibrium shapes can only be found for capillary numbers $Ca$ in the range $[Ca_L, Ca_H]$ where $Ca_L = 0.15$ and $0.6 < Ca_H < 0.75$. Our results in Figure 4.2(a) agree with those of Lac *et al.* [48] in their region of stability (i.e. for moderate capillary numbers); however, our spectral boundary interfacial algorithm also predicts stable equilibrium shapes for higher capillary numbers, e.g. $Ca = 0.9, 1.1$.

To provide more information on the behavior of the capsule at large capillary numbers, in Figure 4.4 we present our numerical results for $Ca = 1.1$. As seen in Figure 4.4(a,b), over time the capsule elongates in the $x$-direction and flattens in the $y$-direction while its depth shows a rather small but non-trivial variation (which was presented earlier in Figure 4.2(c). The lamellar interfacial shape of the capsule at equilibrium is shown in Figure 4.4(c). It is of interest to observe that the capsule profile with the plane $z = 0$, shown in Figure 4.4(a), becomes quite pointed around time $t = 1$ while at equilibrium the edges in the $x$-direction are more rounded but still more pointed than those for $Ca = 0.45$ shown in Figure 4.3(a).

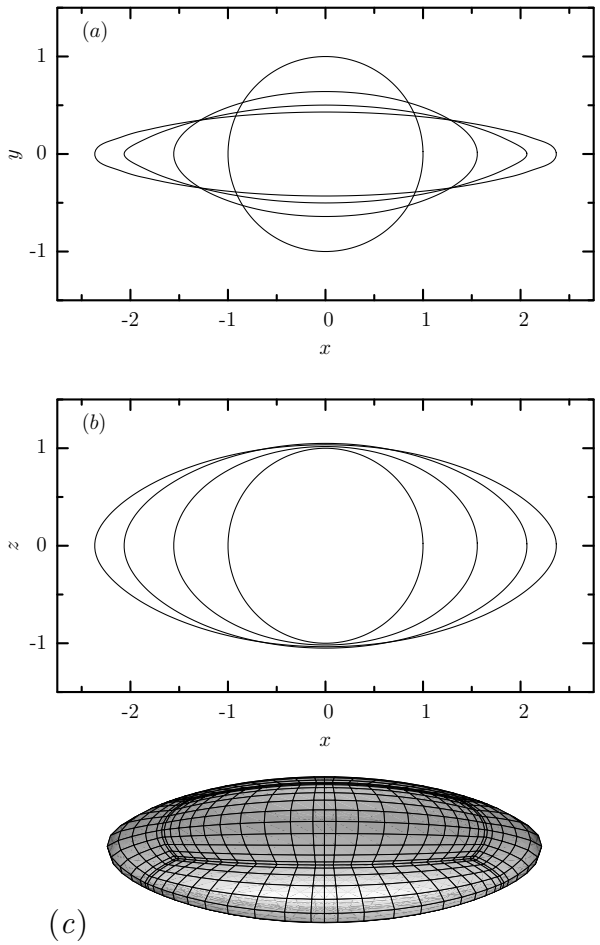


Figure 4.4: Evolution of a Skalak capsule with $C = 1$ in a planar extensional flow with $Ca = 1.1$. (a) Capsule cross-section with the plane $z = 0$ at times $t = 0, 0.5, 1, 18$. (b) Capsule cross-section with the plane $y = 0$ at times $t = 0, 0.5, 1, 18$. (c) Capsule shape at time $t = 18$, i.e. well past equilibrium.

### 4.1.3 Principal Tensions

To investigate the membrane dynamics, in Figures 4.5(a) and (b) we present the time evolution of the maximum $\tau^P_{max}$ and minimum $\tau^P_{min}$ principal tensions, respectively, over the capsule surface for several capillary numbers. The maximum principal tension increases with time from a zero initial value until equilibrium, and thus it is always positive. In addition, higher capillary numbers cause larger values of $\tau^P_{max}$ at equilibrium. The evolution of the minimum principal tension is more complicated. Starting from zero, $\tau^P_{min}$ decreases with time and thus it obtains a negative value at early times. Later the minimum tension increases with time and becomes positive. At equilibrium, $\tau^P_{min}$ increases monotonically with the capillary number.

The location of the minimum and maximum tensions on the capsule surface follows the same basic trend for the different capillary numbers. Initially, the minimum tension $\tau^P_{min}$ occurs at the capsule edges, e.g. looking at the capsule profiles in Figure 4.4, the minimum tension is at $y = z = 0$. After an initial transient period, however, the location of the surface minimum changes. The new surface minimum occurs at the capsule largest depth, e.g. looking at the capsule shape shown in Figure 4.4, the minimum tension occurs at $x = y = 0$. The direction of this tension at late times has no $x$-component, i.e. this tension acts entirely in the $yz$ cross-section. The maximum tension $\tau^P_{max}$ is initially located at the largest width of the capsule, e.g. at the points $x = z = 0$. After a transient period, this tension switches location, and is located in the same place as the steady-state minimum tension; thus at equi-

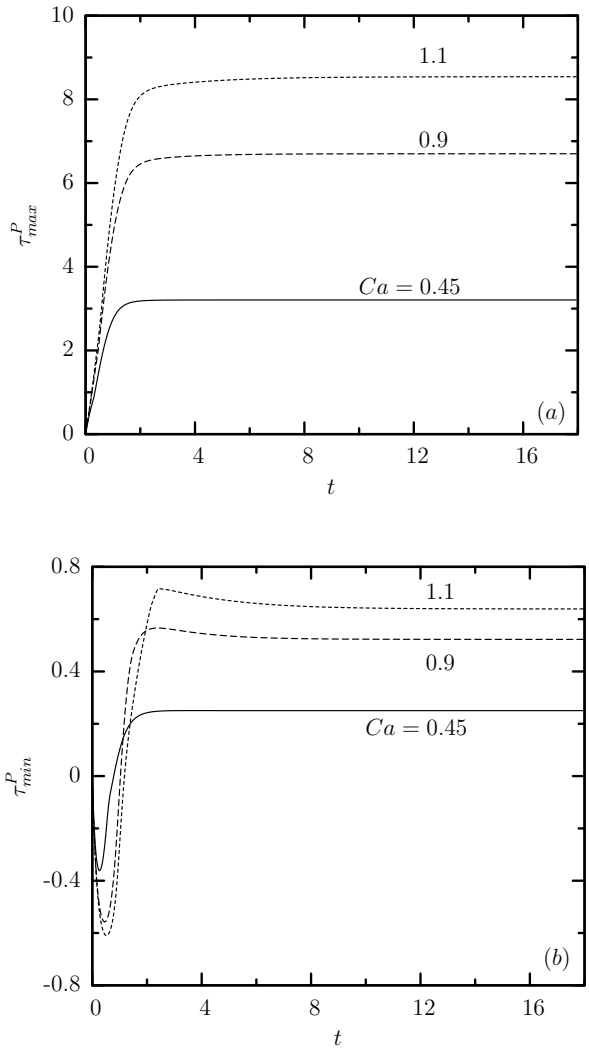


Figure 4.5: Time evolution of the (a) maximum $\tau^P_{max}$ and (b) minimum $\tau^P_{min}$ principal tensions among the spectral discretization points capsule surface for a Skalak capsule with $C = 1$ in a planar extensional flow with $Ca = 0.45, 0.90, 1.1$.

librium, the locations of the minimum and maximum tensions become congruent. Note that the maximum tension $\tau_{max}^{P}$ on the surface is always associated with the direction of the capsule's elongation.

## 4.2 Strong Flows and Cusp Formation

Current understanding of capsule dynamics at higher flow rates than those presented in Section 4.1 is rather limited. Comparing our results with those of Lac *et al.* [48], it is unclear what causes the bi-cubic B-spline methodology to fail in determining the equilibrium shapes for the high capillary numbers we have examined with the SBE method. Lac *et al.* reported that for capillary numbers above the stability limit $Ca_H$ (where $0.6 < Ca_H < 0.75$), the capsule develops high-curvature protruded tips, and the deformation and the tensions in the membrane increase without bound causing interfacial breaking. (See Figure 18(a) from Lac *et al.* [48].) Comparing the capsule profiles at moderate and moderately-high capillary numbers, e.g. for $Ca = 0.45$ and 1.1 shown in Figures 4.3 and 4.4, respectively, we observe that for the higher flow rate the capsule develops pointed edges during the transient evolution. (See the capsule profile with the plane $z = 0$ at time $t = 1$ included in Figure 4.4(a).) For a numerical method to be stable, it must be able to calculate accurately the associated large variation of the curvature at these pointed edges. With respect to this issue, our spectral boundary element method has the significant advantage of the accurate determination of any interfacial property (including curvature) due to the exponential convergence in the numerical accuracy illustrated

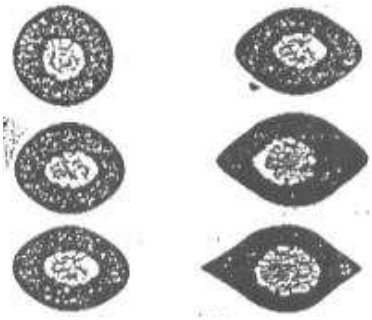

Figure 4.6: Steady-state profiles of a capsule (made from a polymerized polylysine membrane coated by an alginate film) in a planar extensional flow reported in Figure 6 of the work by Barthès-Biesel [6]. As the capillary number increases, the membrane develops first spindled and then cusped edges.

in Figures 3.6 and 3.7.

Experimental findings have revealed a wealth of possible configurations, including stable equilibrium shapes whose edges become rounded, then more extended but still concave (i.e. spindled), and finally convex (i.e. cusped) as the flow rate increases, as shown in Figure 4.6. It is of interest to note that the cusped equilibrium shapes at high flow rates suggest that the membrane shown in Figure 4.6 has negligible bending resistance.

Existing analytical and computational studies are unable to predict the stable spindled and cusped interfacial shapes observed in experiments. The asymptotic solutions for initially spherical capsules by Barthès-Biesel *et al.* [3], for instance, are restricted to small deformations, and the results from the state of the art (low-order) three-dimensional computational methodologies disagree at high flow rates, with none matching the experimental observations. Ramanujan and Pozrikidis [72]

predicted continuous equilibrium elongation, but with rounded interfacial shapes as the flow rate increases, and Lac *et al.* [48] predicted unbounded extension and interfacial breaking at high flow rates. The failure at large deformations of the existing theoretical studies points to the fact that the dynamic behavior of a membrane-like interface submerged in an ambient flow is a complicated physical problem due to the coupling of the fluid dynamics with the (nonlinear) elastic mechanics of the membrane.

On the other hand, the SBE method produces stable equilibrium shapes even at high flow rates. The edges of these shapes become rounded, spindled and finally cusped with increasing flow rate, in excellent agreement with experimental findings. The formation of these cusped edges is a transient process, and by investigating the tensions on the interface, the SBE also elucidates the mechanisms of cusp formation.

### 4.2.1 High-Curvature Tip Formation

Figure 4.7 shows the equilibrium shapes we obtain for several capillary numbers $Ca$ by starting from quiescent initial conditions (i.e. a spherical configuration) and applying a steady flow rate $Ca$. The sequence of equilibrium profiles is (qualitatively) similar to that found in the experiments of Figure 4.6. That is, the shape for $Ca = 1$ shows rounded edges while for $Ca = 1.5$ the edges are more pointed (i.e. the shape is spindled); at higher flow rates the shapes become cusped. We emphasize that we are unable to make quantitative comparisons since the exact parameters in the experimental study are not known, including which constitutive law is best

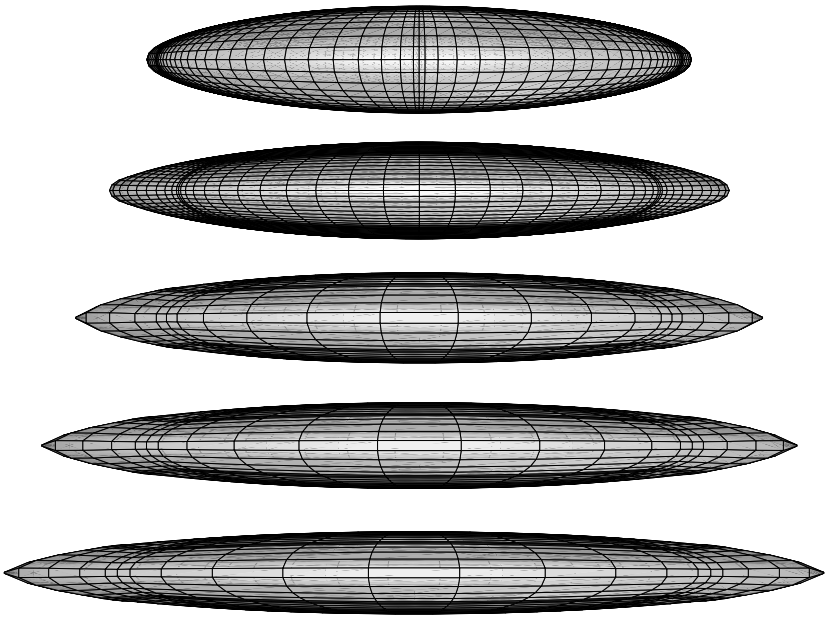

Figure 4.7: Equilibrium shapes for a Skalak capsule with $C = 1$ and $\lambda = 1$ in a planar extensional flow, starting from a sphere, for capillary number $Ca = 1, 1.5, 2, 2.5, 3$. The capsules are extended along the $x$-direction, mainly contracted along the $y$-direction, and the view-point is on the positive $z$-axis.

suited to describe the specific membrane, and the exact value of the viscosity ratio $\lambda$ and the flow rates $Ca$ for the shapes shown in the experimental photographs. (As shown in Figure 20 of Ref.[48], polylysine membrane shows higher surface-area resistance than the Skalak membrane with $C = 1$ used in our computations; this may account for why the experimental shapes show less elongation compared to our shapes.)

Examination of the membrane tensions reveals that the appearance of cusped edges at steady-state is caused by the existence of negative, or compressive, tensions near the capsule edges. Recall that in Section 4.1.3 (Figure 4.5(b)) we observed

transient negative tensions near the beginning of the interfacial evolution, and that these negative tensions occurred at the $y = z = 0$ intersection, which is where the cusp forms at higher capillary numbers. This tension produces no wrinkling owing to its transient nature. Figure 4.8 shows the evolution of the minimum tension on the capsule surface for high capillary numbers, with moderate numbers present for comparison. For $Ca = 0.5, 1, 1.5$ as the geometry reaches equilibrium, the tensions become positive, or tensile, everywhere on the capsule including its edges. Recall that for these shapes $\tau^P_{min}$ relocates to the capsule intersection with the $z$-axis, or $x = y = 0$. For higher flow rates ($Ca = 2, 2.5, 3$), $\tau^P_{min}$ remains located at the capsule edges throughout deformation and reaches a steady-state negative value. The negative tensions near the capsule edges cause local compression (similar to if we pinch the capsule edges with our fingers) which results in cusped equilibrium tips. Unlike the results of Lac *et al.* [48], these are stable equilibrium shapes.

### 4.2.2 Bifurcation at Extreme Capillary Numbers

We emphasize that the value of the capillary number $Ca$ where this transition occurs depends on how the transient dynamics reach equilibrium and thus on the specific transient experiment we apply to the capsule. Therefore, there should be a range of high flow rates where both spindled and cusped equilibrium shapes exist. Note that our results so far represent the case where, to find the equilibrium capsule shape for a given flow rate $Ca$, we start from a spherical geometry and apply a steady flow rate with capillary number $Ca$. In this type of experiment, the lowest

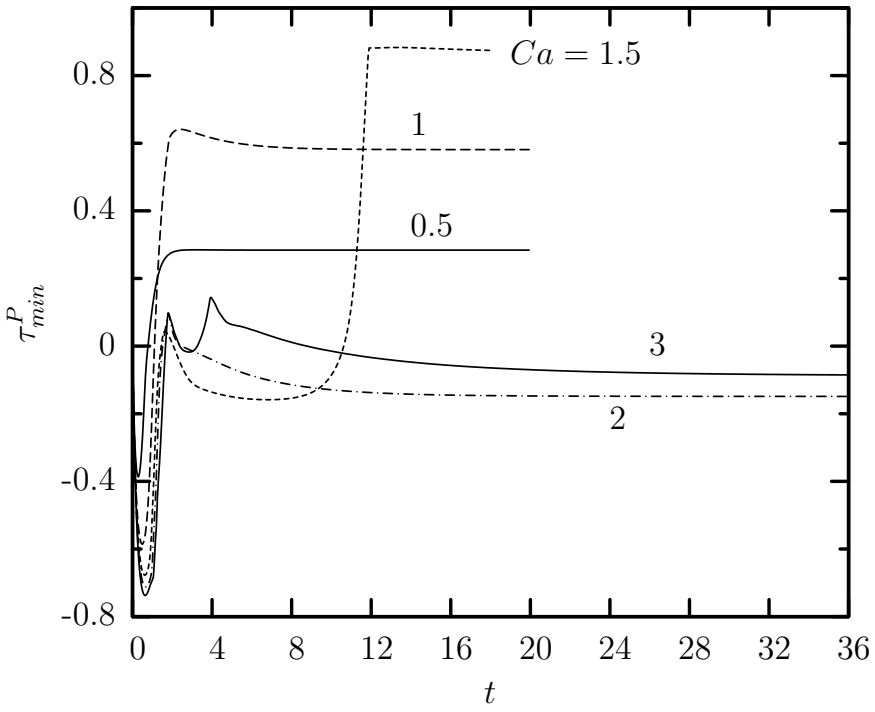


Figure 4.8: Evolution of the minimum principal tension $\tau^P_{min}$ among the spectral discretization points on a Skalak capsule with $C = 1$ and $\lambda = 1$, in a planar extensional flow, starting from a sphere, for $Ca = 0.5, 1, 1.5, 2, 3$.

flow rate where cusped shapes were formed is $Ca = 1.75$.

To find the bifurcation in the equilibrium shapes (i.e. the existence of both spindled and cusped edges for a range of high flow rates), we also implemented another type of experiment. In particular, starting from the rounded shape for $Ca = 1$, we gradually increased the capillary number (with step size $\Delta Ca = 0.25$) allowing the system to reach equilibrium after each flow rate increase. An example of this sort of experiment is shown in Figure 4.9. Here, initially $Ca = 1.5$; after $D$ is at equilibrium, the capillary number is raised to $Ca = 1.75$, which can be observed as a corresponding increase in the deformation. In this experiment, the steady-state shapes are spindled until $Ca = 2.5$ as shown in Figure 4.10; for higher $Ca$ we obtained the cusped profiles we found earlier shown in Figure 4.7. We also implemented a gradual decrease in the capillary number (with step size $\Delta Ca = 0.25$) starting from the cusped equilibrium shape for $Ca = 3$ shown in Figure 4.7. In this experiment, the steady-state shapes are cusped until $Ca = 2$ and spindled for lower flow rates.

To show clearly the transition from spindled to cusped shapes as well as the shape bifurcation, in Figures 4.11(a) and (b) we collect our data for the minimum principal tension $\tau^P_{min}$ and the edge curvature of the equilibrium shapes for the flow rates studied. Near the end of the spindle curve, there is a large increase of the edge curvature with positive value, and thus the pointed shapes have concave (or spindled) edges as shown in Figure 4.10. On the other hand, along the cusp curve the negative tensions near the capsule edges cause local compression and convex (or cusped) equilibrium profiles with large negative edge curvature (Figure 4.7). It is

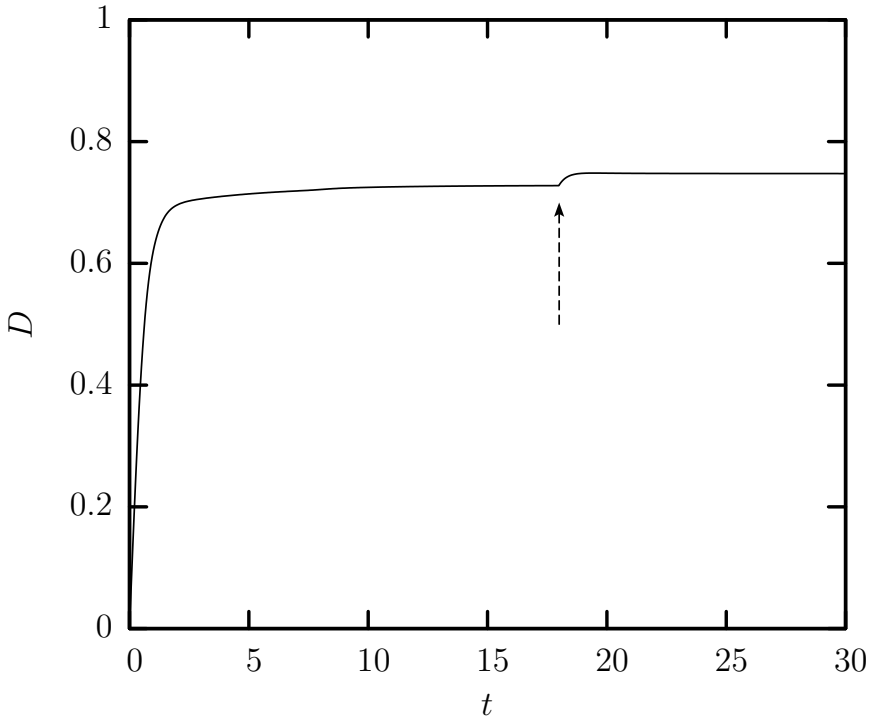


Figure 4.9: In order to produce a smooth, non-cusped geometry at a high capillary number, we start with a lower capillary number, allow it to come to equilibrium, and then raise the capillary number. Here $D$ is shown as a function of time for a simulation beginning with $Ca = 1.5$, and then transitioning to $Ca = 1.75$ at $t = 18$. The final geometry is smooth, with no negative tensions on the surface.

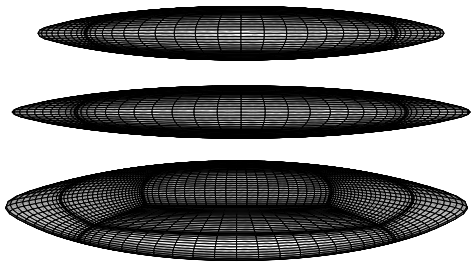

Figure 4.10: Spindled equilibrium shapes for a Skalak capsule with $C = 1$ and $\lambda = 1$ in a planar extensional flow with capillary number $Ca = 2, 2.5$. A three-dimensional view of the $Ca = 2.5$ shape is also included to show the flat elliptical conformation of the capsule. These shapes lie in the bifurcation range $1.75 \leq Ca \leq 2.5$ and were found by gradually increasing the flow rate.

of interest to note that, although the shape bifurcation creates a district change in the capsule profile, it causes minimal changes in the capsule's overall dimensions.

A similar shape transition and bifurcation (but over a limited range of high flow rates) was predicted by the complex-variable analysis of Antanovskii for two-dimensional bubbles [2]; however, computational (transient) dynamics were not able to verify the stability of these equilibrium shapes [64].

### 4.2.3 The Effect of Viscosity Ratio on the Bifurcation

Because there is no internal fluid motion at equilibrium, previous investigators believed that the viscosity ratio can have no effect of the steady-state solution for a capsule extended in planar extensional flow [48]. However, the results with SBE show that multiple steady-state solutions can exist for one capillary number in

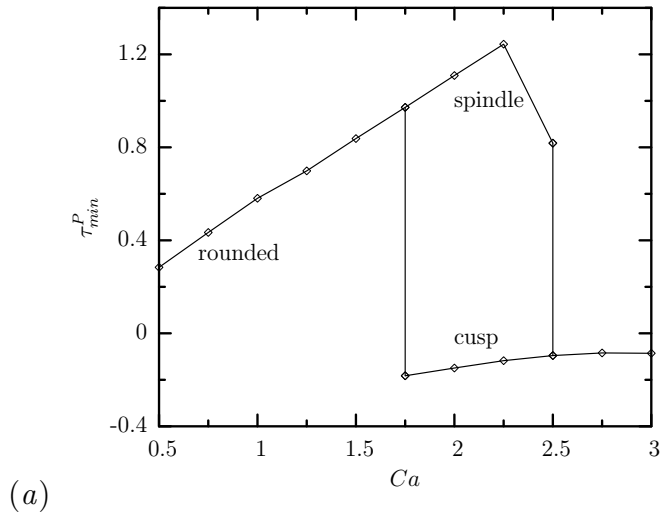


$(a)$

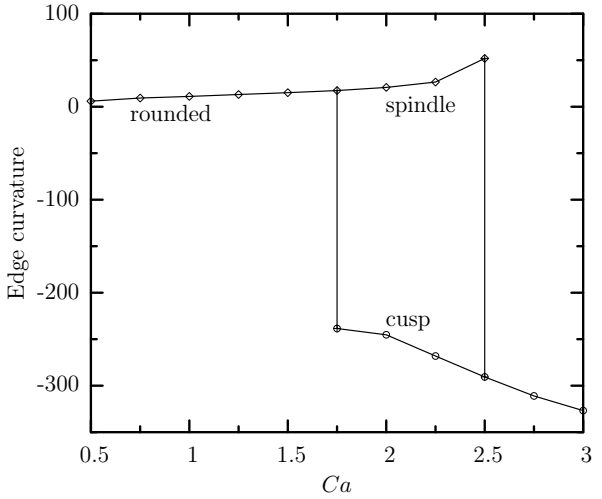


$(b)$

Figure 4.11: Bifurcation in the dependence of (a) the minimum principal tension $\tau^P_{min}$ and (b) the edge curvature (determined along the interfacial cross-section with the $z = 0$ plane) with the capillary number $Ca$, for the equilibrium shape of a Skalak capsule with $C = 1$ and $\lambda = 1$ in a planar extensional flow.

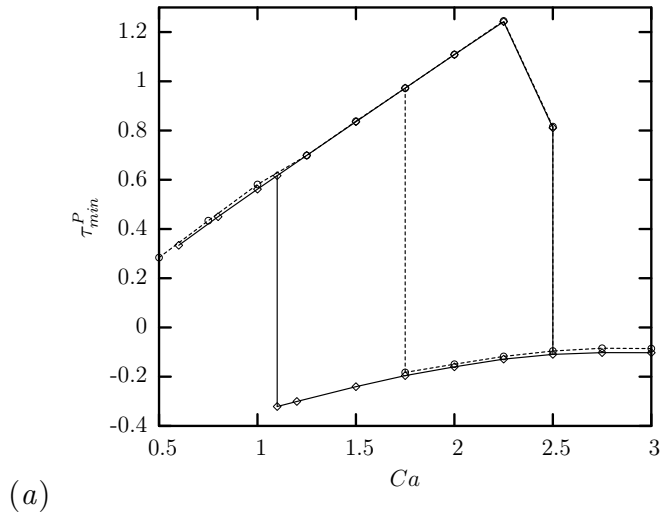


$(a)$

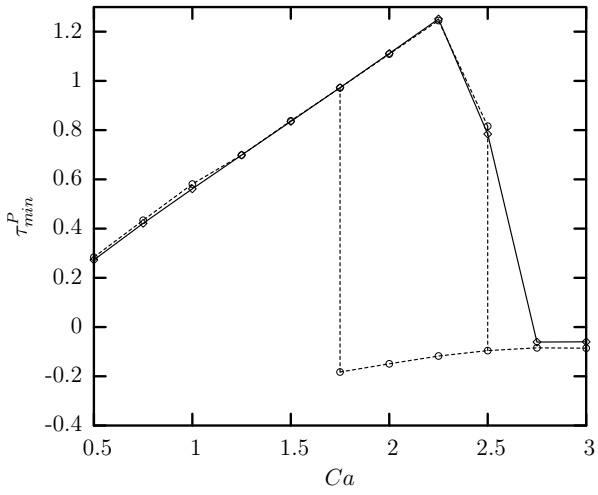


$(b)$

Figure 4.12: The dependence of the minimum principal tension $\tau^P_{min}$ with the capillary number $Ca$, for the equilibrium shape of a Skalak capsule with $C = 1$ for (a) $\lambda = 5$ and (b) $\lambda = 0.1$ in a planar extensional flow. The dotted lines indicate the results for $\lambda = 1$ from Figure 4.11(a). At large viscosity ratios, the bifurcation region expands. At small viscosity ratios, it contracts and disappears entirely.

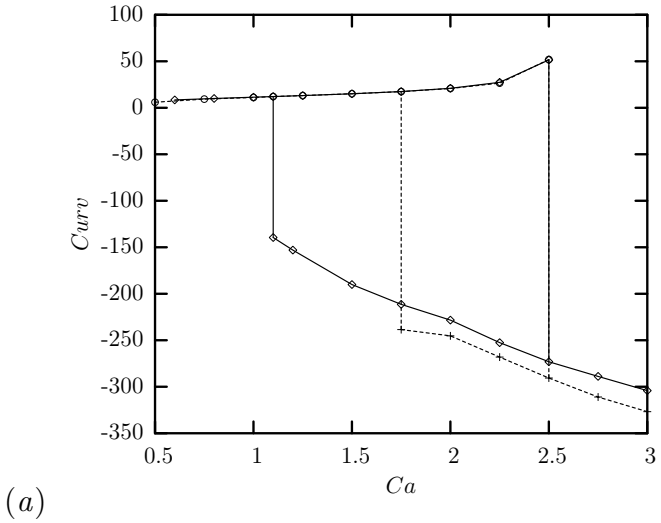


$(a)$

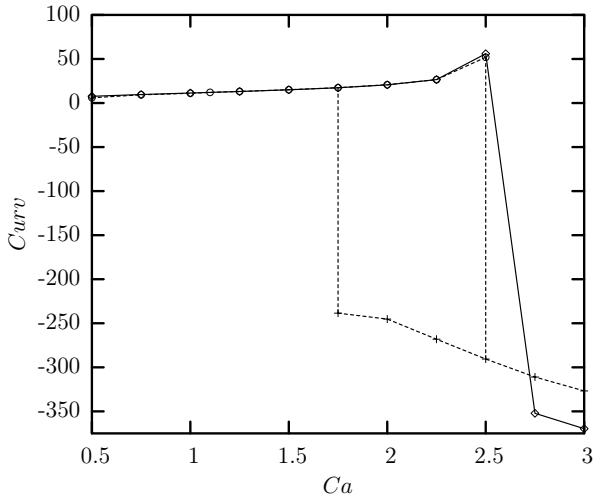


$(b)$

Figure 4.13: The dependence of the edge curvature with the capillary number $Ca$, for the equilibrium shape of a Skalak capsule with $C = 1$ for (a) $\lambda = 5$ and (b) $\lambda = 0.1$ in a planar extensional flow. The dotted lines indicate the results for $\lambda = 1$ from Figure 4.11(b).

planar extensional flow, and that the steady-state solution for a particular capsule deformation problem depends on the transient deformation dynamics. Therefore, while the influence of the viscosity ratio will disappear at equilibrium because internal fluid motion ceases, it is possible for the viscosity ratio to determine which equilibrium geometry a capsule achieves by influencing the transient dynamics.

To investigate possible effects of viscosity ratio, we reproduced for different $\lambda$ the tension bifurcation plot shown in Figure 4.11 for $\lambda = 1$. Figures 4.12(a) and (b) show the results for $\lambda = 5$ and $\lambda = 0.1$, respectively. In both figures, the behavior for $\lambda = 1$ is shown for comparison as a dotted line. At higher viscosity ratios, as shown in Figure 4.12(a), the lower limit of the bifurcation region decreases and the region extends. That is, at higher viscosity ratios, cusp formation is first observed at lower capillary numbers. Raising the viscosity ratio does not affect the upper limit of the bifurcation region. Conversely, at lower viscosity ratios, the lower limit of the bifurcation region increases, so the region contracts. Eventually, the bifurcation disappears entirely, as seen in Figure 4.12(b). Similar results are observed with respect to the edge curvature, shown in Figures 4.13(a) and (b).

## 4.3 Length Changes and Maximum Surface Tension

We have also examined how the equilibrium semi-axis lengths and the maximum surface tension change as a function of capillary in moderate to high planar extensional flow. Figure 4.14 shows the semi-axis lengths length $L$, width $S$ and depth $W$ for $\lambda = 1$ in a planar extensional flow. $L$ increases with capillary number.

Both $W$ and $S$ decrease with capillary number. At high capillary numbers, within the bifurcation region, there are no overall capsule length differences between the smooth shapes and the cusped conformations.

Based on our computational modeling, rupture due to excessive surface tension can be determined for a specific membrane (with known lytic tension) by monitoring the membrane tensions during the capsule's dynamic evolution. It may also be estimated readily by the simple dependence of the equilibrium maximum principal tension $\tau^P_{max}$ with the capillary number which our analysis shows to be linear at high flow rates as illustrated in Figure 4.15. Starting from a sphere, initially $\tau^P_{max}$ occurs at the capsule intersection with the $y$-axis, and shortly thereafter it relocates to the $z$-axis intersection, the equilibrium location; for gradual changes in the flow rate, $\tau^P_{max}$ remains at the $z$-axis intersection. Thus this location is the most probable to rupture in an extensional flow.

## 4.4 Conclusions

As the flow rate increases, the transition from spindled to cusped shapes allows the capsule to withstand the increased hydrodynamic forces, as found for low-viscosity drops or bubbles in strong extensional Stokes flow [16]. We note that strong flows are commonly encountered in industrial and physiological processes, because artificial capsules have wide applications in the pharmaceutical, food and cosmetic industries [69]. In pharmaceutical processes, for example, capsules are commonly used for the transport of medical agents. For mm-size capsules made from

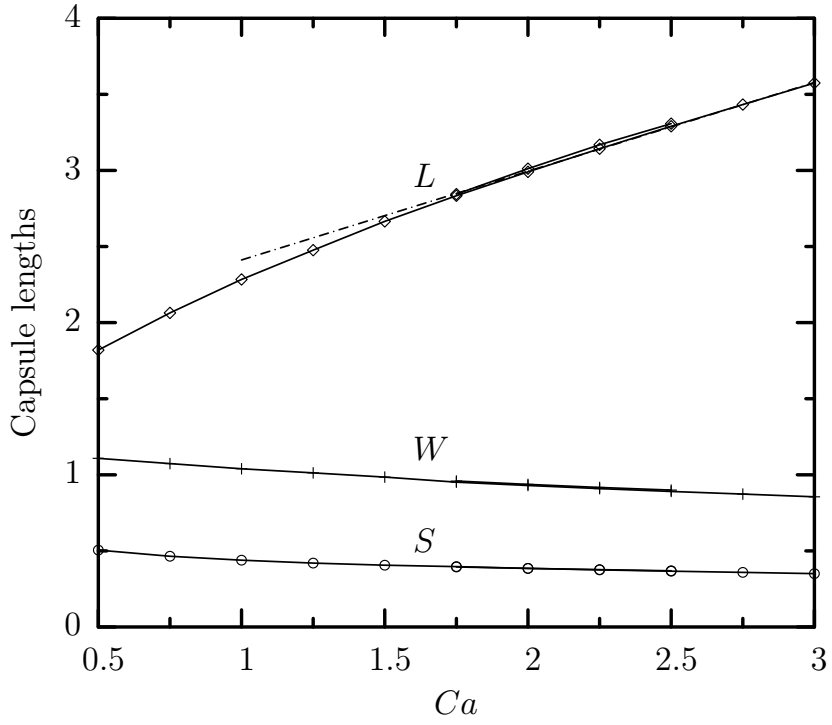


Figure 4.14: Influence of the capillary number $Ca$ on the equilibrium semi-axis lengths length $L$, width $S$ and depth $W$ for a Skalak capsule with $C = 1$ and $\lambda = 1$ in a planar extensional flow. Based on our data for $2 \leq Ca \leq 3$ the best linear fit $(-\cdot-)$ for the capsule length is $L \approx 1.83 + 0.58\,Ca$.

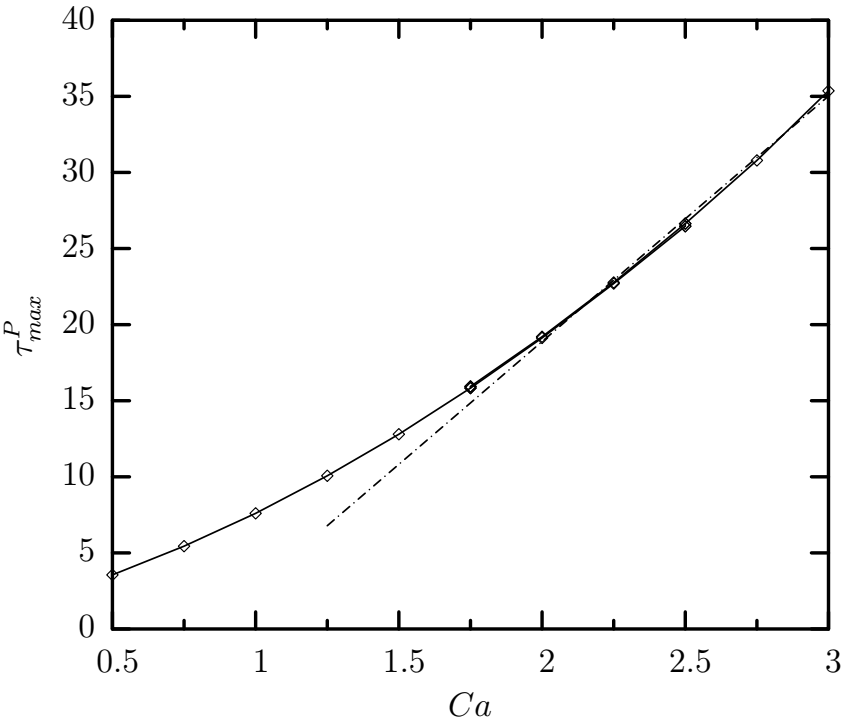


Figure 4.15: Influence of the capillary number $Ca$ on the equilibrium maximum principal tension $\tau^P_{max}$, for a Skalak capsule with $C = 1$ and $\lambda = 1$ in a planar extensional flow. Based on our data for $2 \leq Ca \leq 3$ the best linear fit $(-\cdot-)$ is $\tau^P_{max} \approx -13.4 + 16.1\, Ca$.

aminomethacrylate membranes with shearing modulus $G_s = O(10^{-2})$ N/m and for $\mu$m-size erythrocytes with $G_s = O(10^{-5})$ N/m, flow rates $Ca = O(1)$ require shear stress $\mu G = O(10)$ Pa [56, 61].

The investigation also reveals that viscosity ratio $\lambda$ can affect the steady-state solution for a capsule in planar extensional flow, even though there is no internal fluid motion at equilibrium. Raising or lowering the viscosity ratio either expands or shrinks, respectively, the bifurcation region. The effect is entirely on the lower limit of the bifurcation region; the upper limit is unaffected by viscosity ratio. This suggests that cusp formation can be controlled or eliminated over a range of capillary numbers through manipulation of the viscosity ratio.

The shape transition at high flow rates occurs due to the appearance of compressive tensions near the capsule edges. We emphasize that our results were derived for zero bending resistance; as the bending resistance increases from zero (but still remains very small as happens for many artificial and biological membranes), we expect that the transition from concave to convex edges occurs at a slightly higher flow rate. Much higher bending resistance will probably inhibit the transition to cusped shapes.

It is of interest to note that compressive tensions at low flow rates result in interfacial wrinkling around the capsule equator [48, 87]. The occurrence of compressive tensions can be caused either by mechanical deformation (i.e. due to an external flow as investigated in this chapter) or owing to a (bio)physical process, as in the case of a fluid vesicle undergoing lipid uptake [83]. At large deformations, the analytical prediction of the formation of compressive tensions for nonlinear elastic

laws is practically unattainable; thus, computational investigation is an attractive alternative. The large values of the edge curvature for spindled and, more importantly, for cusped capsules, along with the fact that the membrane tensions are complicated functions of the interfacial geometry, clearly indicate the need for a highly-accurate computational methodology (such as our interfacial spectral algorithm) for the accurate determination of membrane dynamics in strong flows.

# Chapter 5

# Strain-Softening Membranes in a Planar Extensional Flow

In Chapter 4, we examined in detail the behavior of an initially spherical, Skalak capsule deformed in a planar extensional flow. We showed that the SBE method extends the range of stable solutions past that of previous numerical methods, and we identified and characterized the process of cusp formation at high flow rates for these capsules. However, the Skalak law is only representative of certain classes of membrane, such as biocompatible serum albumin alginate [17] and the erythrocyte membrane [8]. A key feature of these membranes is that they are strain-hardening [7]. That is, the relationship between strain and tension is not linear. Rather, with increasing extension, the tension rises faster than if the relation were linear. In contrast, many synthetic membranes are strain-softening; the rate at which tension grows with increasing extension slows as the extension becomes larger. This strain-softening effect is often due to polymer disentanglement. Instead of a Skalak model, these synthetic membranes are better represented by the Mooney-Rivlin and Neohookean membrane models [87]. It was predicted by Barthès-Biesel, Diaz, and Dhenin that the behavior of strain-softening membranes

may diverge radically from that of strain-hardening membranes at large deformations [7]. Therefore, in this chapter we investigate the behavior of a strain-softening Neohookean membrane, at large deformation in an extensional flow, and compare its behavior to the Skalak membrane studied in Chapter 4.

## 5.1 Neohookean Extension in Weak to Moderate Flows

The results presented here for Neohookean capsules in a planar extensional flow with undisturbed flow field $\boldsymbol{u}^{\infty} = G(x, -y, 0)$ use simulation parameters $N_B = 12$ and $\Delta t = 5 \cdot 10^{-4}$, unless otherwise specified. The number of surface elements $N_E$ is 10 for $Ca < 0.325$, and 14 for $Ca \geq 0.325$. The Neohookean results are compared with the results for Skalak capsules from Chapter 4. At large extensions corresponding to the Skalak bifurcation region, all comparisons made to Skalak capsules use the spindled, not the cusped, equilibrium geometries.

For flow rates $Ca \leq 0.4$, the SBE method produces stable, extended, equilibrium geometries for Neohookean capsules. Figure 5.1 shows the deformation $D$ and the semi-axis lengths $L$, $S$, and $W$ as a function of time for Neohookean capsules at capillary numbers below, including, and above the upper limit of $Ca = 0.4$. The simulation results for $Ca = 0.4$ have been extended to $t = 40$ to verify that it does in fact attain a stable, steady-state geometry. Lac *et al.* previously reported that their bi-cubic B-spline method produced no equilibrium solutions above $Ca = 0.24$ for this capsule type [48]; the SBE method has shown that this upper limit was merely an artifact of their numerical technique. As we saw in Chapter 4 for Skalak

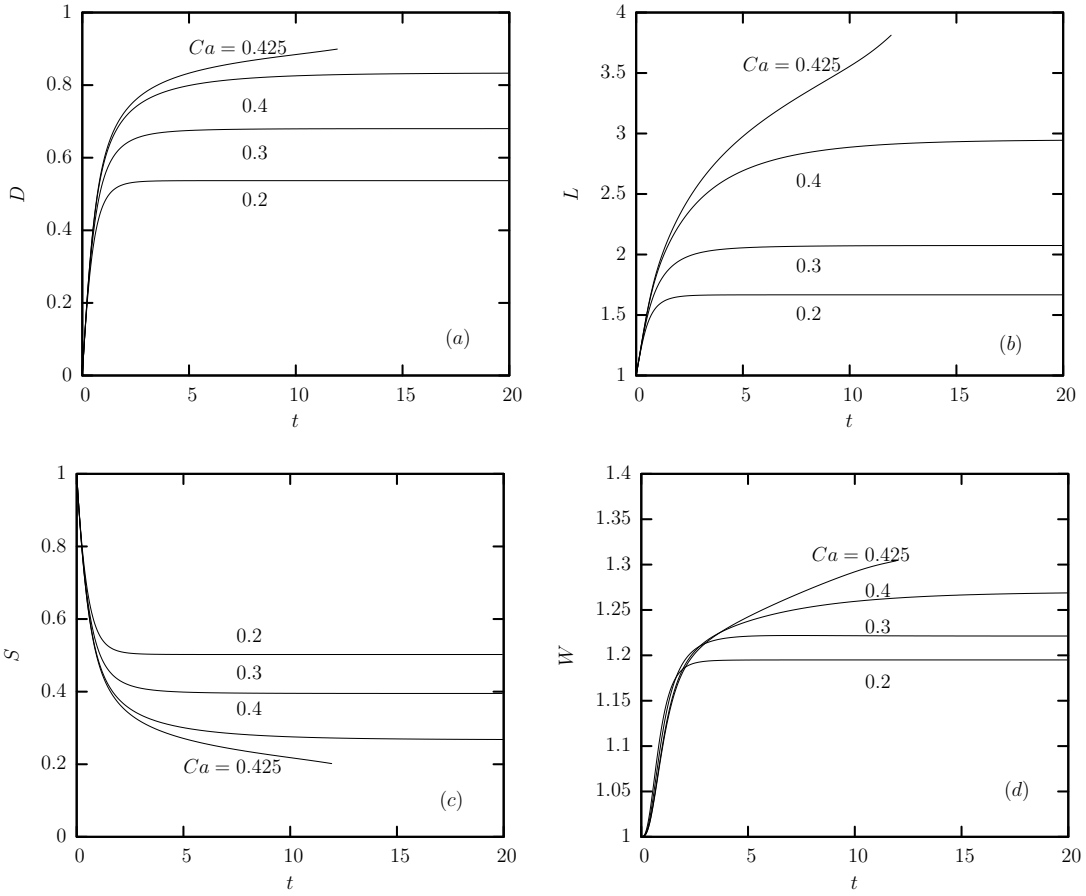


Figure 5.1: For Neohookean capsules in a planar extensional flow, (a) $D$, (b) $L$, (c) $S$, and (d) $W$ are shown as a function of time for capillary numbers $Ca = \{0.2, 0.3, 0.4, 0.425\}$. For the capillary numbers $Ca \leq 0.4$, the capsule reaches an equilibrium shape after an initial transient period. (Note that we have continued the solution for $Ca = 0.4$ until $t = 40$ to ensure that it does reach an equilibrium solution). When $Ca = 0.425$, the capsule appears to undergo continuous extension, i.e. its length increases without bound.

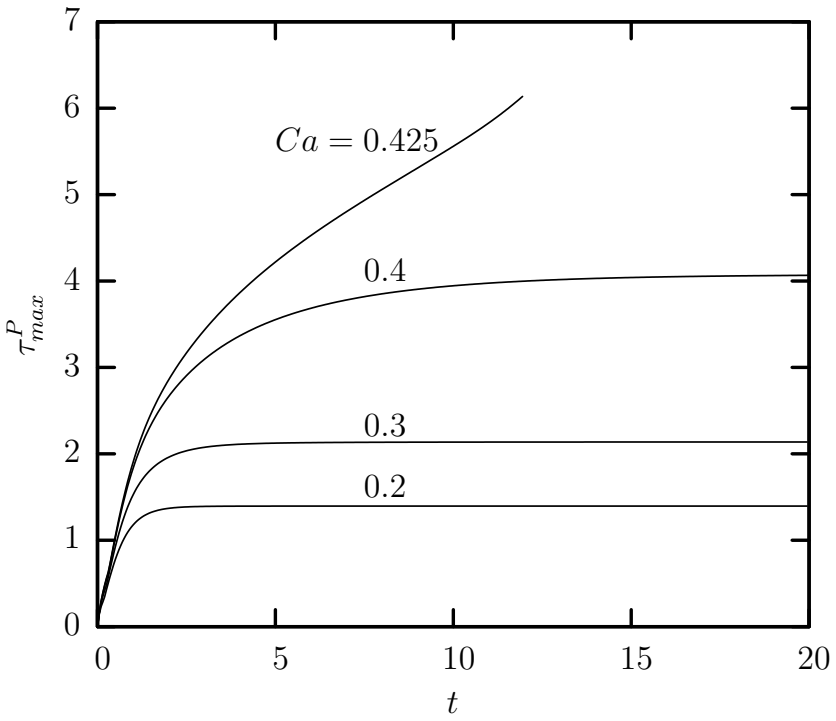


Figure 5.2: The maximum principal tension $\tau^P_{max}$ on the surface shown as a function of time for capillary numbers $Ca = \{0.2, 0.3, 0.4, 0.425\}$ for a Neohookean capsule in a planar extensional flow. The tension reaches an equilibrium value for $Ca \leq 0.4$, but increases without bound at $Ca = 0.425$. This behavior is similar to the behavior of the length $L$ shown in Figure 5.1(b).

capsules, the SBE method obtains stable equilibrium results at capillary numbers above the upper stability of previous low-order methods, because of its ability to resolve complicated geometries accurately. However, the present method also encounters an upper limit. As Figure 5.1(b) demonstrates, at $Ca = 0.425$, just above the upper limit, the largest length $L$ appears to pass through an inflection point, after which it continues to increase without bound. The maximum tension $\tau^P_{max}$, shown in Figure 5.2, behaves like $L$. Eventually, the simulation can no longer accurately describe the geometry because it becomes too extended, and the numerical method fails.

The equilibrium geometry for Neohookean capsules at weak flow rates is similar to that of Skalak capsules. Figures 5.3(a) and (b) show the cross-sections in the planes $z = 0$ and $y = 0$, respectively for a Neohookean capsule with $Ca = 0.2$. The equilibrium geometry for a Skalak capsule with the same capillary number is also shown for comparison. At this capillary number, the Neohookean capsule is only slightly more extended than the Skalak capsule. The remaining dimensions are also comparable. Figure 5.3(c) shows the final geometry for the Neohookean capsule; it appears as an ellipsoid.

At higher flow rates, however, the appearance of the deformed Neohookean capsules differs considerably from that of their Skalak counterparts. Figures 5.4(a) and (b) show the same cross-sections for a Neohookean capsule with $Ca = 0.4$. The equilibrium geometry for the Skalak capsule at the same capillary number, shown as the dotted line (— —) now appears much less deformed than the Neohookean capsule. The dimension in the direction of extension is almost twice as much for

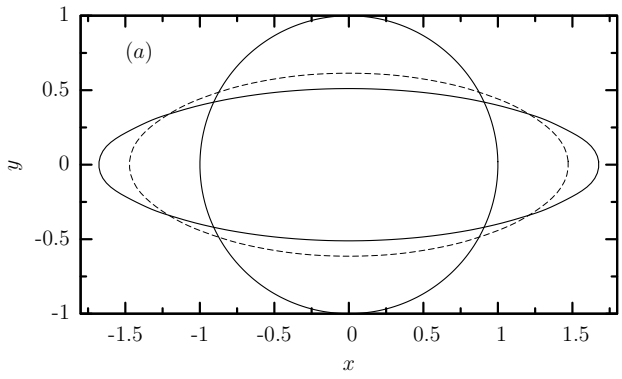


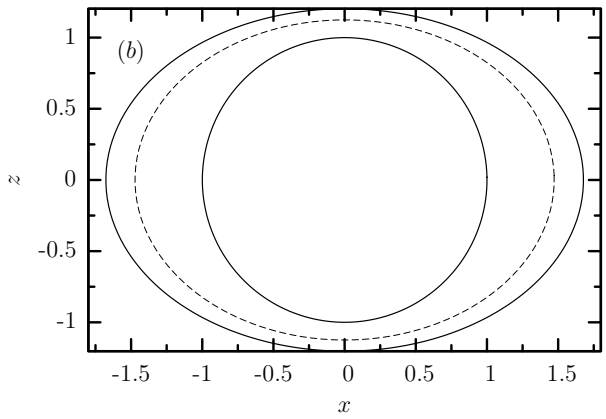


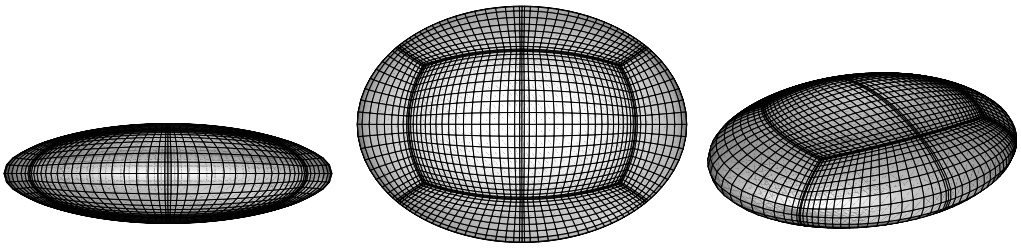

(c)

Figure 5.3: The initial ($t = 0$) and equilibrium ($t = 20$) geometric cross-sections for a Neohookean capsule (——) in a planar extensional flow with $Ca = 0.2$, and the equilibrium cross-sections of a Skalak capsule (— —) with the same capillary number for purposes of comparison. (a) Capsule cross-sections with the plane $z = 0$. (b) Capsule cross-sections with the plane $y = 0$. (c) Neohookean capsule shape at equilibrium, from several viewing angles.

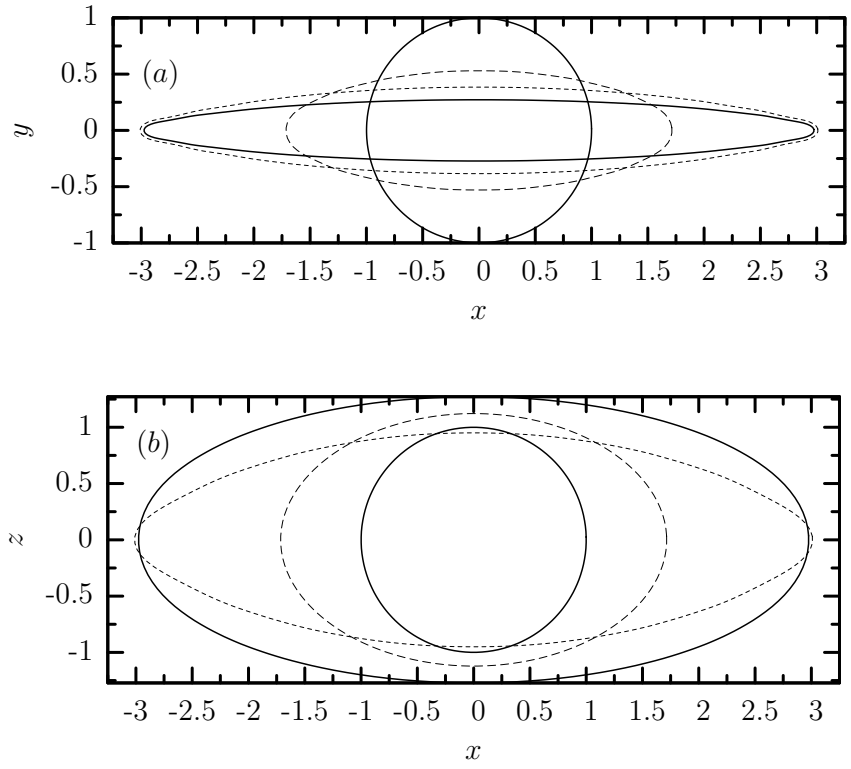


Figure 5.4: The initial ($t = 0$) and equilibrium ($t = 40$) geometric cross-sections for a Neohookean capsule (——) in a planar extensional flow with $Ca = 0.4$. Also shown are equilibrium cross-sections for a Skalak capsule for the same capillary number (— —), and for $Ca = 2$ (- - - -), which has similar extension. (a) Capsule cross-sections with the plane $z = 0$. (b) Capsule cross-sections with the plane $y = 0$.

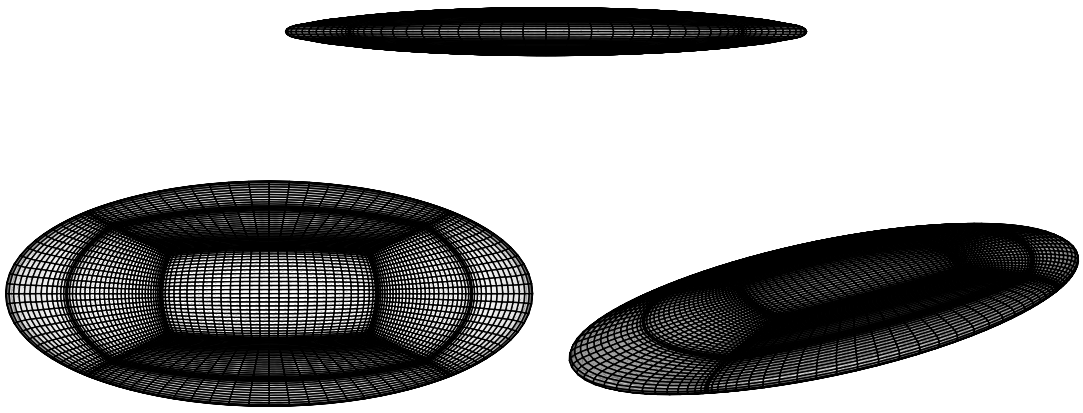

Figure 5.5: The equilibrium geometry ($t = 40$) for a Neohookean capsule with $Ca = 0.4$ in a planar extensional flow, from several viewing angles.

the Neohookean compared to the Skalak capsule. For the Skalak capsule, $Ca = 0.4$ produces moderate deformation, while for the Neohookean capsule, $Ca = 0.4$ should be considered a strong flow, because it produces large deformation.

To compare the large deformation equilibrium geometries between the two membrane laws, the cross-sections in Figure 5.4 also display the final geometry for a Skalak capsule with $Ca = 2$, shown as the dotted line (----). This capillary number was chosen because the capsule dimension in the direction of extension is similar to the Neohookean capsule at 0.4. As is clear from the Figure 5.4(a), at similar extension, the Neohookean capsule is thinner, and in Figure 5.4(b) the cross-section in that plane appears rounder. Examining the equilibrium geometry for the Neohookean capsule from several viewing angles, as in Figure 5.5, it appears not ellipsoidal, but flat and lamellar.

## 5.2 Equilibrium Behavior with Increasing Flow Rate

We have observed that the equilibrium geometry for a Neohookean capsule at a given capillary number appears more extended and flatter than its Skalak counterpart. To examine this comparison more closely, Figure 5.6 illustrates the steady-state behavior of deformation $D$, and semi-axis lengths $L$, $S$, and $W$ for a Neohookean capsule (solid lines) in a planar extensional flow over a range of capillary numbers up to $Ca = 0.4$, the upper stability limit. The vertical line on Figure 5.6(a) indicates the upper stability limit reported by Lac *et al.* for Neohookean capsules in this flow pattern [48]. As the flow rate increases, $D$, $L$, and $W$ increase, while $S$ decreases. Results for Skalak capsules over the same range of capillary numbers are also shown on Figure 5.6 as dotted lines for purposes of comparison. The Neohookean capsules are slightly more deformed than Skalak capsules at low capillary numbers, and much more deformed at higher flow rates. Over this range of capillary numbers, $L$ appears to grow linearly with $Ca$ for Skalak capsules, but shows a much faster, monotonic increase for Neohookean capsules, as seen in Figure 5.6(b). Consequently, at $Ca = 0.4$ the Neohookean capsule is almost twice as extended as the Skalak capsule. The rates of change also differ between the two capsule types for $S$ and $W$; $S$ decreases in both cases, but more rapidly for the Neohookean membrane, while $W$ increases for the Neohookean membrane, but holds steady over this range of capillary numbers for the Skalak membrane.

The maximum tension $\tau_{max}^{P}$ on the surface, shown for both capsule types in Figure 5.7(a), behaves as a function of capillary number like the largest semi-axis

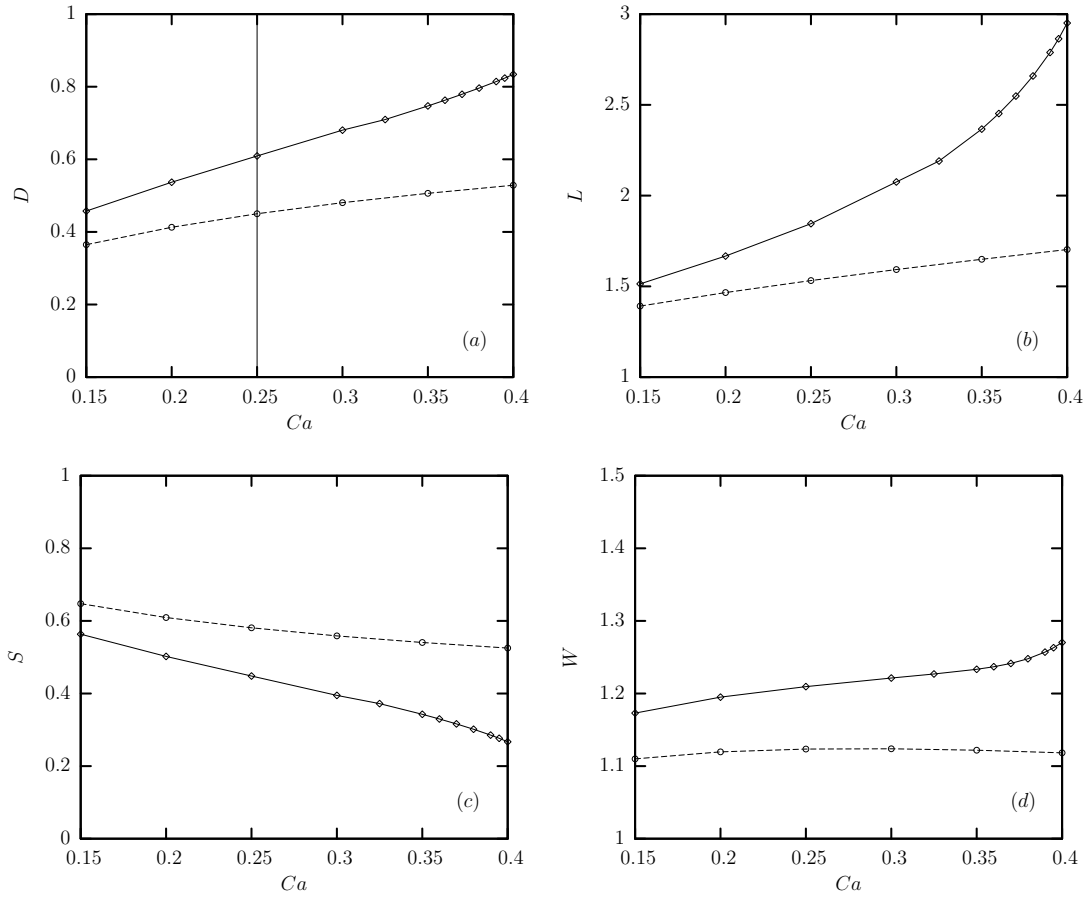


Figure 5.6: Equilibrium dimensions of a Neohookean (solid line) or Skalak (dotted line) capsule in a planar extensional flow as a function of capillary number: (a) Deformation $D$, and semi-axis lengths (b) $L$, (c) $S$, and (d) $W$ as a function of capillary number. The solid vertical line in (a) represents the upper stability limit for Neohookean capsules in planar hyperbolic flow reported by Lac *et al.* using their bi-cubic B-spline method [48].

length $L$. That is, it grows linearly over this range of capillary numbers for Skalak capsules, but appears to grow faster for Neohookean capsules. Combined with the fact that $\tau^P_{max}$ is associated with the direction of extension, this similarity in behavior suggests that $L$ can serve as a proxy for strain, if we wish to examine the tension versus strain behavior, which is determinant of whether a membrane is strain-softening or hardening. Examining $\tau^P_{max}$ as a function of $L$ also allows us to compare the two membrane laws over the entire range of capsule deformations, without being restricted to a small window of capillary numbers. Figure 5.7(b) shows $\tau^P_{max}$ as a function of $L$ for both membrane types, and the strain-hardening behavior of the Skalak capsule now becomes apparent. As the capsule extends, for the Neohookean capsule, the tension increases only linearly with $L$; for the Skalak capsule, the tension grows faster than linear. The picture produced is remarkably similar to Figures 1 and 3 produced by Barthès-Biesel *et al.* with these two capsules for uniaxial extension and isotropic expansion, respectively.

Besides tension, other quantities can also be examined over the entire range of extension by examining their behavior as a function of $L$. Figure 5.8(a) and (b) show $S$ and $W$, respectively, versus $L$. Although the absolute magnitude of $S$ given $L$ differs between the two membranes, the trend is similar; we observe decreasing capsule thickness with increasing extension. However, the behaviors are different with respect to the intermediate length $W$. For Neohookean capsules, $W$ increases monotonically over the entire range of extension pictured. For Skalak capsules with increasing $L$, $W$ at first increases at low extension, and then decreases over most of the range of capillary numbers examined. The differences in behavior for the

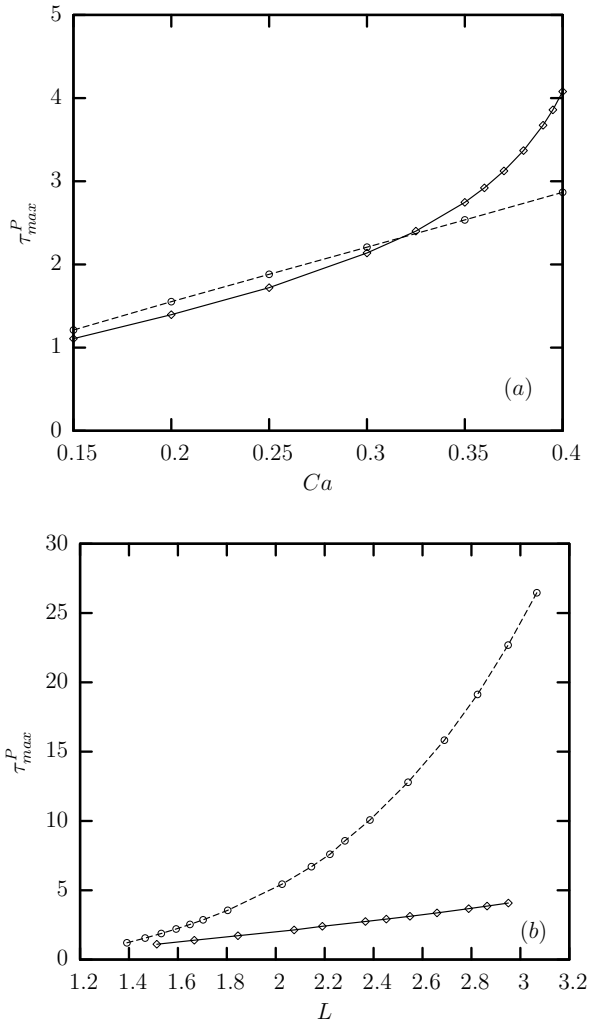


Figure 5.7: (a) The maximum equilibrium tensions $\tau^P_{max}$ on the capsule surface are shown over a range of capillary numbers for Neohookean (solid line) compared to Skalak (dotted line) capsules in a planar extensional flow. (b) $\tau^P_{max}$ are shown as a function of $L$ for the same capsule types and flow pattern.

two non-extensional axes can be summed up by examining the aspect ratio $S/W$, pictured in Figure 5.9(a). Apparent from the figure, for the Skalak capsule, the ratio approaches a non-zero asymptote of 0.4 at large deformations, while this ratio appears unbounded for the Neohookean capsule over the range of capillary numbers for which we obtain stable equilibrium solutions. This means that at large capsule extension, the zy-cross section (perpendicular to the direction of extension) will appear more circular for the Skalak capsules. The Neohookean cross section will be a more extended ellipsoid, and the overall geometry for the extended Neohookean capsules will be more lamellar, or pancake-like, compared to the Skalak capsules. Interestingly, however, the edge curvature for these two capsules, shown in Figure 5.9(b) is the same, and depends only on extension, regardless of membrane material composition.

## 5.3 Continuous Extension

As we previously observed in Section 5.1, the capsule extension increases without bound when $Ca$ is above the upper stability limit of $Ca = 0.4$. We have attempted to verify the numerical results for $Ca = 0.425$ by decreasing the time-step to $2.5 \cdot 10^{-4}$; the results are unchanged. We have also varied the number of surface elements $N_E$ from 14 to 10, and although there is a slight disparity in the magnitude of the length values, the overall behavior is the same.

Unclear from the transient results is whether the transition to continuous extension observed at $Ca = 0.425$ is a phenomenon arising from the transient de-

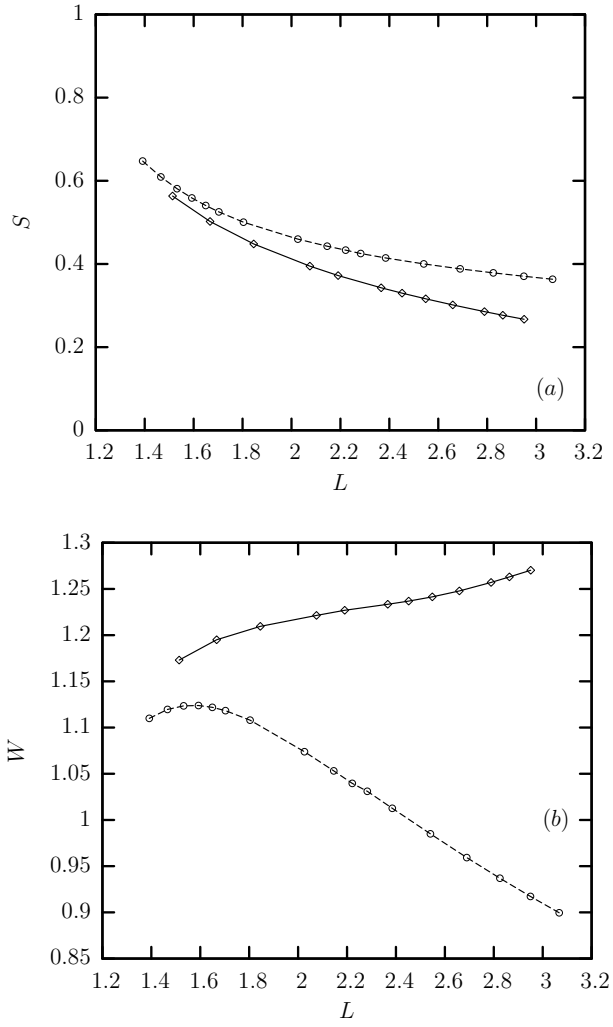


Figure 5.8: Using $L$ as a proxy for strain as in Figure 5.7(b), the remaining two semi-axis lengths are examined as a function of capsule extension in a planar extensional flow for Neohookean (solid line) compared to Skalak (dotted line) capsules. (a) $S$ is shown as a function of $L$; the overall behavior is similar for strain-softening and strain-hardening capsules. (b) $W$ is shown as a function of $L$; while $W$ increases with $L$ for Neohookean capsules over the entire range of capillary numbers explored, it decreases with $L$, after an initial plateau, for Skalak capsules.

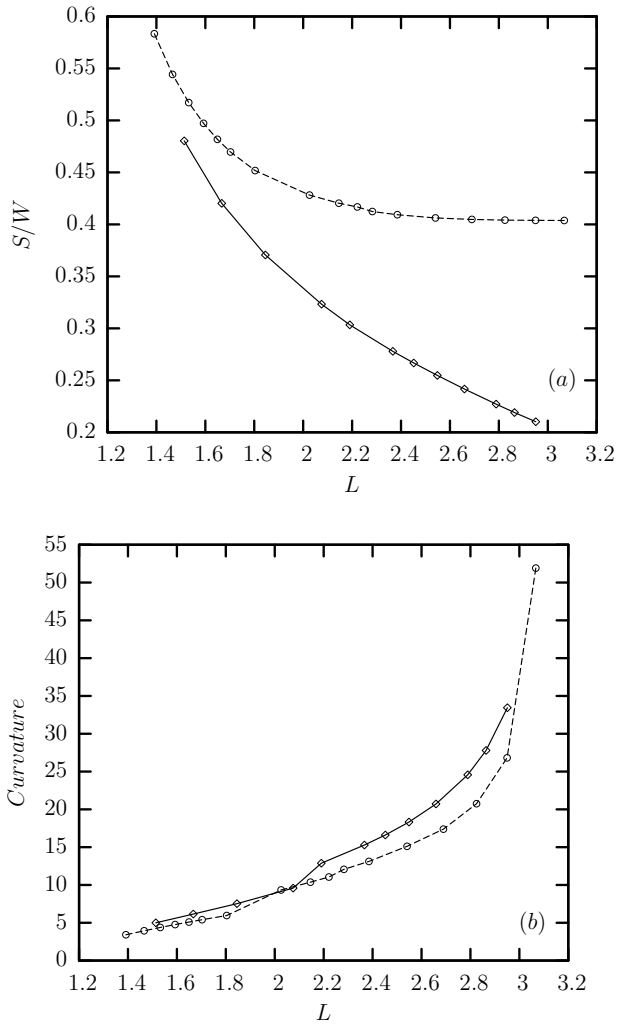


Figure 5.9: (a) The ratio $S/W$ of the two non-extensional axes is shown as a function of capsule extension $L$ in a planar extensional flow for Neohookean (solid line) compared to Skalak (dotted line) capsules. For the Skalak capsule, this ratio approaches a non-zero asymptote of approximately 0.4 at large deformations. This ratio for the Neohookean capsule does not approach a limit in the range of capillary numbers for which we obtain stable equilibrium solutions. (b) Edge curvature is nearly identical for Neohookean and Skalak capsules.

formation process, whether this capillary number actually represents a flow rate at which no equilibrium solution exists, or whether continuous extension here is a numerical artifact due to insufficient grid density for such an extended geometry. To eliminate the first of these three possibilities, we performed a stepping experiment, similar to the experiments in Chapter 4 used to characterize the shape bifurcation. Here, a Neohookean capsule was deformed at $Ca = 0.4$ and allowed to reach equilibrium. Then, the capillary number was raised to $Ca = 0.425$. The results of this experiment for $L$ and $S$ are shown in Figure 5.10. If the continuous extension came from the transient process, we expected that this would produce a stable equilibrium geometry. Instead, the capsule transitions to continuous extension, indicating either that there is no stable geometry corresponding to this flow rate, or that the geometry is so extended that the numerical method fails.

Examining the development of the geometric cross-sections in the plane of extension in Figure 5.11(a) for $Ca = 0.4$, the highest capillary number to produce a stable, steady-state geometry, we observe that both the transient and final geometries have a rounded tip, not unlike the highly deformed but still concave Skalak shapes discussed in Chapter 4. However, as can be seen in Figure 5.11(b), the transition to continuous extension at $Ca = 0.425$ is accompanied by a transition to cusp formation. The cusp is also observed in the Figure 5.11(c), the incremental experiment described in the previous paragraph. This cusp bears a resemblance to the cusp observed previously with Skalak capsules, but with a major difference; the cusped Skalak capsules are stable, steady-state geometries, while the Neohookean capsules are undergoing a continuous extension process, which eventually results in

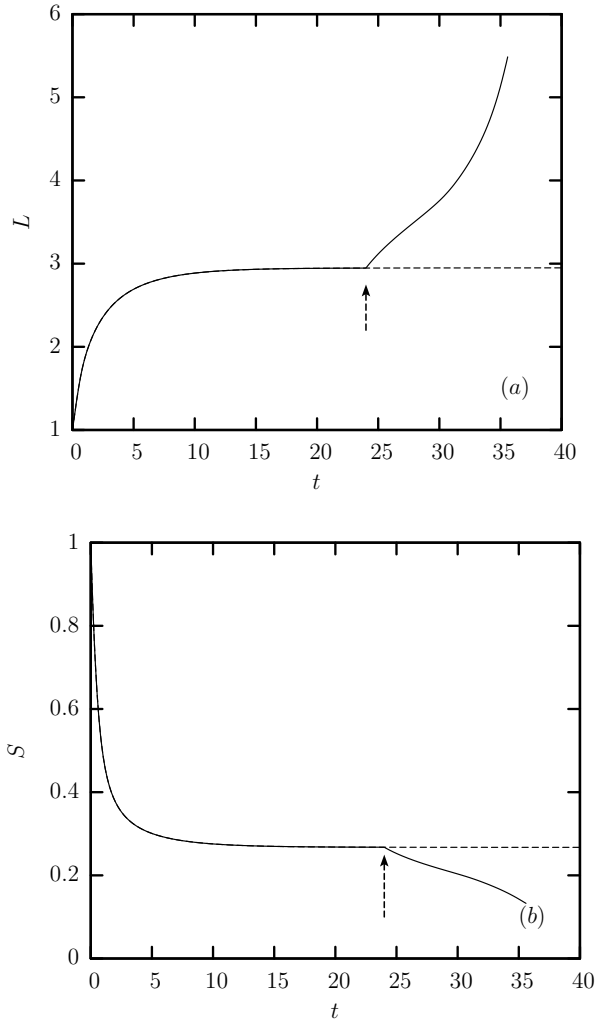


Figure 5.10: The semi-axis lengths (a) $L$ and (b) $S$ are displayed as a function of time for a stepping experiment with a Neohookean capsule in an extensional flow. Initially, $Ca = 0.4$, and the capsule is allowed to reach equilibrium. At $t = 24$, indicated by the arrow, the capillary number increases to $Ca = 0.425$, and the capsule undergoes continuous extension. The dotted line indicates the behavior of an unperturbed capsule allowed to remain at $Ca = 0.4$.

failure of the numerical method.

## 5.4 Conclusions

In the previous chapter, we examined strain-hardening Skalak capsules in extensional flow, found that the SBE method is capable of modeling highly extended geometries, and characterized a bifurcation phenomenon at strong flow rates, in which both smooth and cusped steady-state geometries exist. In contrast, the Neohookean capsules studied in this chapter are strain-softening. Consequently, Neohookean capsules become highly extended at much lower flow rates than do Skalak capsules. The shapes of the extended capsules are also less rounded, and more lamellar, than Skalak capsules with similar extension. No steady-state cusp formation was observed with Neohookean capsules.

Examining the capsule geometry and associated membrane tensions as a function of capsule extension $L$ has allowed us to compare Skalak and Neohookean capsules over the entire range of extension, instead of a narrow window of flow rates. Examining tension in this way, as in our Figure 5.7(b), contrasts the strain-softening versus strain-hardening membrane behavior. Examining the two smaller semi-axes, we found congruent behavior with respect to the capsule thickness $S$, but divergent behavior with respect to depth $W$. We have also shown that, for the strain-hardening Skalak capsules, the ratio $S/W$ approaches a limit at large extensions, while no such limit is observed for the strain-softening Neohookean capsules. The geometric implications of this limit are that the aspect ratio for the two non-

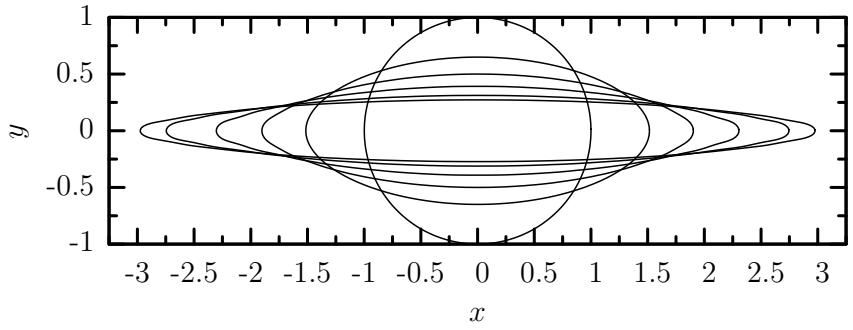


(a)

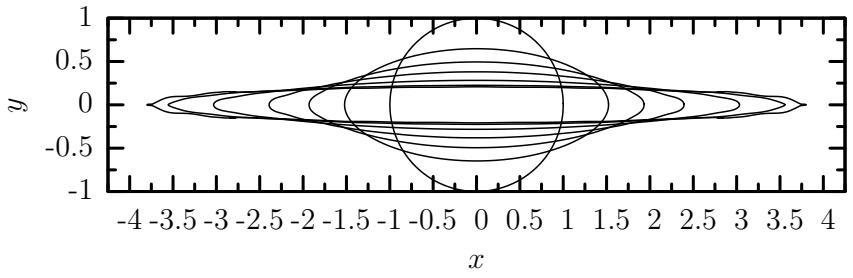


(b)

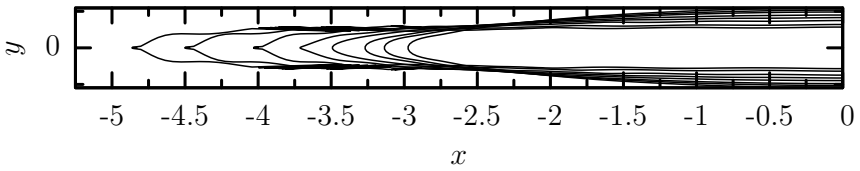


(c)

Figure 5.11: (a) Cross sections in the plane of extension for $Ca = 0.4$ at times $t = \{0, 0.5, 1, 2, 5, 40\}$ show formation of a smooth, rounded equilibrium geometry. (b) Cross sections for $Ca = 0.425$ at times $t = \{0, 0.5, 1, 2, 5, 10, 12\}$ show cusps accompanying continuous extension. (c) Cross sections for the transient experiment described in Figure 5.10 at times $t = \{24, 25, 26, 28, 30, 32, 34, 35\}$ show a shape transition to a cusped conformation accompanied by continuous extension. $t = 24$ is the time at which the capillary number was raised.

extensional directions remains comparable for the strain-hardening capsules, but it does not for the strain-softening capsules.

At flow rates $Ca > 0.4$ with Neohookean capsules, we have observed unbounded extension, with subsequent failure of the numerical method. We have attempted to verify the continuous extension behavior we observe at larger flow rates by using alternate surface grids, time step refinement, and also the stepping experiment shown in Figure 5.10. The stepping experiment indicates that the continuous extension is not a result of the transient process, but it remains unclear whether it represents a physical transition to a region of capillary numbers in which no steady-state geometry exists, or merely a numerical artifact. Consider that in the case of a steady-state geometry in an extensional flow, the boundary integral equation simplifies

$$\boldsymbol{u}^{\infty}(\boldsymbol{x}_0) = \frac{1}{8\pi\mu} \oint_S \Delta \boldsymbol{f}(\boldsymbol{x}) \cdot \boldsymbol{S}(\boldsymbol{x}, \boldsymbol{x}_0) dS \tag{1}$$

All quantities in this expression, including $\boldsymbol{u}^{\infty}$, $\Delta \boldsymbol{f}$, and $\boldsymbol{S}$, are functions of geometry $\boldsymbol{x}$, but this geometry is now not known *a priori*. If continuous extension actually occurs at higher flow rates, then we predict that, for the Neohookean law, a solution for $\boldsymbol{x}$ should exist when $Ca \leq 0.4$, but not when $Ca > 0.4$. Investigation into this hypothesis could help to determine whether or not the continuous extension process we have observed for Neohookean capsules represents a physical transition in behavior, as opposed to a product of the numerical scheme employed.

# Chapter 6

# Erythrocyte Deformation in a Simple Shear Flow

In this chapter, we extend the SBE method to model an erythrocyte deforming in shear flow. The SBE method for erythrocytes has been designed to address many of the shortcomings of previous methods, and it produces solutions in excellent agreement with experimental results. The results produced with our method also supplement existing experimental results, many of which are incomplete due to geometric constraints; SBE provides a truly three-dimensional picture of cellular deformation in shear flow, over a range of flow rates and viscosity ratios.

## 6.1 Modeling the Erythrocyte

The resting geometry of an erythrocyte is not spherical, but in the shape of a biconcave disc, pictured in Figure 6.1. Working with experimental observations from interference microscopy, Evans and Fung gave the following empirical equation to describe the half-thickness $f(r)$ as a function of the radial distance $r$ from the

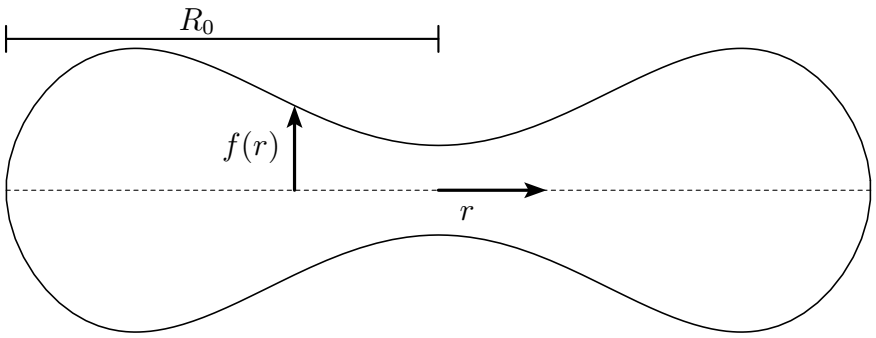


Figure 6.1: The biconcave disc geometry of a resting erythrocyte under physiological conditions. $r$ indicates the radial distance from the central axis of symmetry, and $f(r)$ the half-thickness at $r$. $R_0$ is the radius of the largest cross-section of the biconcave disc. This geometry is taken from the results of Evans and Fung [30].

central axis of symmetry [30]

$$f(r) = \frac{1}{2}\left[1 - \left(\frac{r}{R_0}\right)^2\right]^{\frac{1}{2}}\left[C_0 + C_2\left(\frac{r}{R_0}\right)^2 + C_4\left(\frac{r}{R_0}\right)^4\right] \tag{1}$$

At physiological osmolarity (300 $mO$), $R_0 = 3.91\ \mu m$, $C_0 = 0.81\ \mu m$, $C_2 = 7.83\ \mu m$, and $C_4 = -4.39\ \mu m$. The surface area to volume ratio is high; excess surface area means that, without bending resistance or some other factor, the surface will buckle easily. At hypotonic osmolarity of 217 $mO$, the cells are swollen, and the parameters become $R_0 = 3.80\ \mu m$, $C_0 = 2.10\ \mu m$, $C_2 = 7.58\ \mu m$, and $C_4 = -5.59\ \mu m$. Because certain abnormal states including hereditary elliptocytosis and spherocytosis are associated with a loss of membrane surface area, the surface area to volume ratio for these swollen cells is representative of the pathological geometry

[56].

The erythrocyte membrane, discussed in Sections 1.1 and 2.4, is a complex, multi-layered object. The plasma membrane is essentially a two-dimensional, incompressible fluid [9], but the spectrin skeleton exhibits shear resistance like a two-dimensional elastic solid [39]. This raises the question whether, in constructing an erythrocyte model, the interface should be represented as a liquid, a solid, or some combination of the two.

If the interface is thought of as a two-dimensional fluid, then the erythrocyte is being represented as a fluid vesicle. A basic fluid vesicle model, of the type implemented by Zhou and Pozrikidis [90], by Kraus *et al.* [46], or by Sukumaran and Seifert [85], characterizes the surface by a two-dimensional isotropic stress (surface tension $\gamma$). Unlike in the case of a liquid droplet [88], the surface tension $\gamma$ varies over the surface; it is not known *a priori*. Rather, the distribution of $\gamma$ on the surface must be calculated so the area incompressibility condition is satisfied; that is, a surface distribution for $\gamma$ must be determined such that two-dimensional continuity $\nabla_S \cdot \boldsymbol{u} = 0$ holds everywhere on the surface. Mathematically and computationally, this is a much more difficult problem than determining the stress distribution resulting from the known deformation of an elastic solid, as in Chapter 2. In the absence of simplifications, one must solve for $\gamma$ across the surface simultaneously with velocity $u$. The three studies cited above restricted themselves to the case of a viscosity ratio $\lambda$ of unity in order to simplify the problem. Thus, these methods are not reflective for the erythrocyte, either *in vivo*, where $\lambda \approx 5$, or in the laboratory using ektacytometry equipment, discussed in Section 6.3.1, where $\lambda \approx 0.1$.

On the other hand, treating the erythrocyte membrane as a two-dimensional elastic solid, as we treated elastic capsules in previous chapters, also introduces computational difficulties. The erythrocyte model of Pozrikidis [68], extended from the elastic capsule model of Ramanujan and Pozrikidis [72], treats the membrane in this way. The axisymmetric erythrocyte model of Secomb *et al.* is also of the two-dimensional elastic solid type [75, 76, 77]. The basic numerical implementation appears straightforward, and stable methods exist, including our own, and particularly for the case of negligible bending resistance. These approaches have proven accurate and reliable for a range of artificial capsules. However, in the case of the erythrocyte, the ratio of area dilatation to shear modulus is, as stated in Section 2.4, approximately $10^4 - 10^5$. The relative magnitudes of the shearing and area dilatation resistances result in a stiff problem. That is, the dilatation tensions develop over a short time scale, which requires a very small time step, but shearing tensions develop over a long time scale, which necessitates a long simulation runtime. Previous investigators who used this approach for three-dimensional simulation weakened these requirements by employing a much smaller moduli ratio than the true physical value (several orders of magnitude smaller) [68] in order to make the problem computationally feasible.

Further, it is questionable to what extent either model is representative of physical reality. The fluid vesicle model tends to miss key aspects of erythrocyte membrane mechanics, like shear elasticity, and because it lacks correspondence with any reference geometry, it also cannot account for erythrocyte shape memory. Erythrocyte shape memory was demonstrated by Fischer [33] when he showed that,

after tank-treading, an erythrocyte will always reform its two dimples in the same distinct loci on the membrane. However, the elastic solid model is not a completely accurate model either. While the plasma membrane component of the erythrocyte membrane is nearly area incompressible, it is essentially a two-dimensional fluid, not an elastic solid. That is, the plasma membrane enforces overall area incompressibility, but the phospholipid molecules can flow on the surface. Representing the membrane as an elastic solid eliminates its fluid nature, and attempts to enforce not only global area stability, but also local area incompressibility for every differential elastic surface element, a much more stringent condition.

A final consideration in formulating an accurate and computationally amenable model for the erythrocyte membrane is that, as discussed in Section 2.4, the erythrocyte membrane does exhibit measurable bending resistance, with reduced bending modulus $\kappa$ of $3.8 \times 10^{-3}$ [73, 77]. This is not large enough to affect the overall cellular deformation [56], but it will prevent local buckling which could otherwise occur under certain flow conditions. A realistic model for the erythrocyte membrane must have a way of preventing localized buckling, although it will not necessarily do so by representing explicitly the formation of bending moments.

## 6.2 Prestress and Adaptive Prestress for Area Incompressibility

The mechanism by which the plasma membrane enforces area incompressibility is an isotropic surface stress. Such a stress can also be generated with an elastic

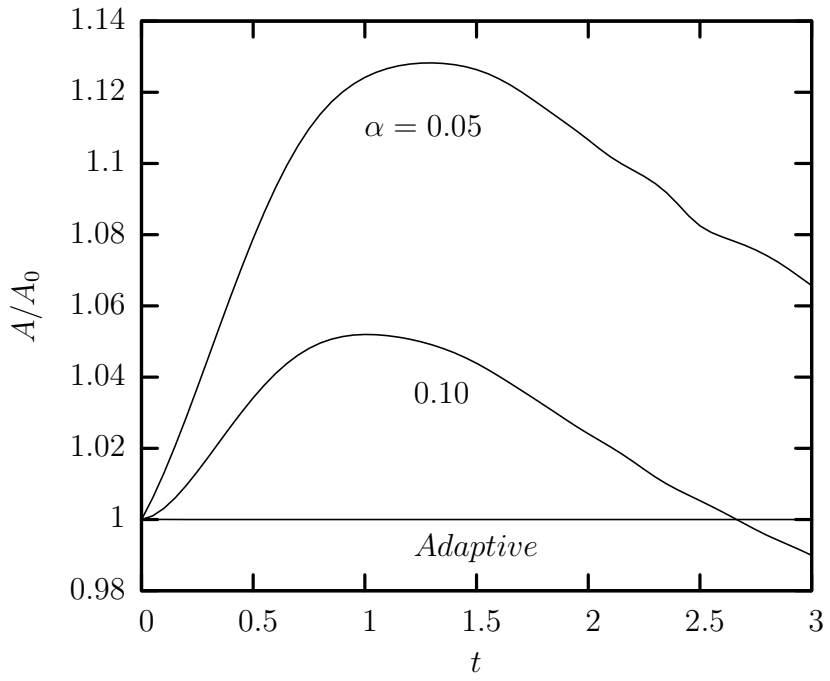


Figure 6.2: The normalized surface area for a biconcave disc in shear flow with two different levels of prestress, $\alpha = 0.05$ and 0.10. Also displayed are the results with adaptive prestress, which effectively maintains a constant surface area ($Ca = 1.5, \lambda = 0.1$, Skalak law, $C = 1$)

element surface model. Applying a prestress, generated by shrinking or expanding the elastic reference shape, without changing the current shape, will apply an isotropic surface tension to an undeformed shape, and add a near-isotropic tension to a deformed shape. Lac *et al.* employed using minor prestresses to represent elevated internal cell pressure [49]. They also used it to prevent local buckling, by counteracting any local compressive tensions [50]. Thus they extended the range of possible capillary numbers they could study with their numerical method.

We have applied prestress in combination with the Skalak material law ($C = 1$) using the SBE method to demonstrate that it can also be used to enforce overall area incompressibility. Following Lac *et al.* [49], we define the prestress parameter $\alpha$ such that all lengths in the undeformed capsule would be scaled by $(1+\alpha)$, relative to the reference shape. Thus, for $\alpha = 0.05$, for instance, the undeformed capsule would be 5% larger than the reference. Note that this is mathematically equivalent to scaling the stretch ratios by $(1 + \alpha)$. Figure 6.2 shows the normalized change in area over a short time for the cases of $\alpha = 0.05$ and $\alpha = 0.10$. It is apparent that prestress counteracts the shearing forces in the flow, to dampen the initial area rise. However, area oscillations of greater than 4 % are still observed for the larger prestress. Further, as the simulation continues, the prestress causes contraction, and the normalized area drops significantly below 1. Consequently, we decided to implement an adaptive prestress algorithm. The goal was to adjust the prestress continually throughout the numerical method, in order to achieve a constant surface area. The algorithm is based on a standard discrete PID controller, with the output

(prestress level) given by the control equation

$$\alpha_n = \alpha_{n-1} + (K_p + K_i + K_d)e_n - (K_p + 2K_d)e_{n-1} + K_d e_{n-2} \tag{2}$$

The prestress $\alpha_n$ is adjusted at each time step based on $\alpha_{n-1}$ from the previous step, the current error $e_n$ in surface area, and, for iterations after the initial two, the error from the previous two steps $e_{n-1}$ and $e_{n-2}$. $K_p$, $K_i$, and $K_d$ are the proportional, integral, and derivative control parameters, respectively. Using the parameter settings $K_p = K_i = K_d = 1$, we obtained excellent control performance, so no attempt was made to tune the control parameters. Figure 6.2(c) shows that the adaptive prestress method maintains a near-constant surface area for a biconcave disc in shear flow. SBE with adaptive prestress produces a stable solution for the erythrocyte deformation problem over a range of moderate capillary numbers. At the capillary number shown, the adaptive prestress $\alpha$ is less than 15% throughout the simulation. At a slightly higher capillary number, such as $Ca = 2.25$, $\alpha \leq 20\%$ throughout the simulation.

Local area incompressibility enforced in a basic elastic model, as stated previously, does not allow the surface to flow as a fluid; rather, connected elements are fixed to one another. By applying a prestress to the shape, which can change such that the surface area remains constant, we allow local area changes in one section of the membrane to compensate for complementary changes in other places. This hybrid model retains the basic elastic element model to represent the spectrin network, and enforces via prestress the area incompressibility aspect of the plasma membrane. The prestress method also avoids creating a stiff problem, because all

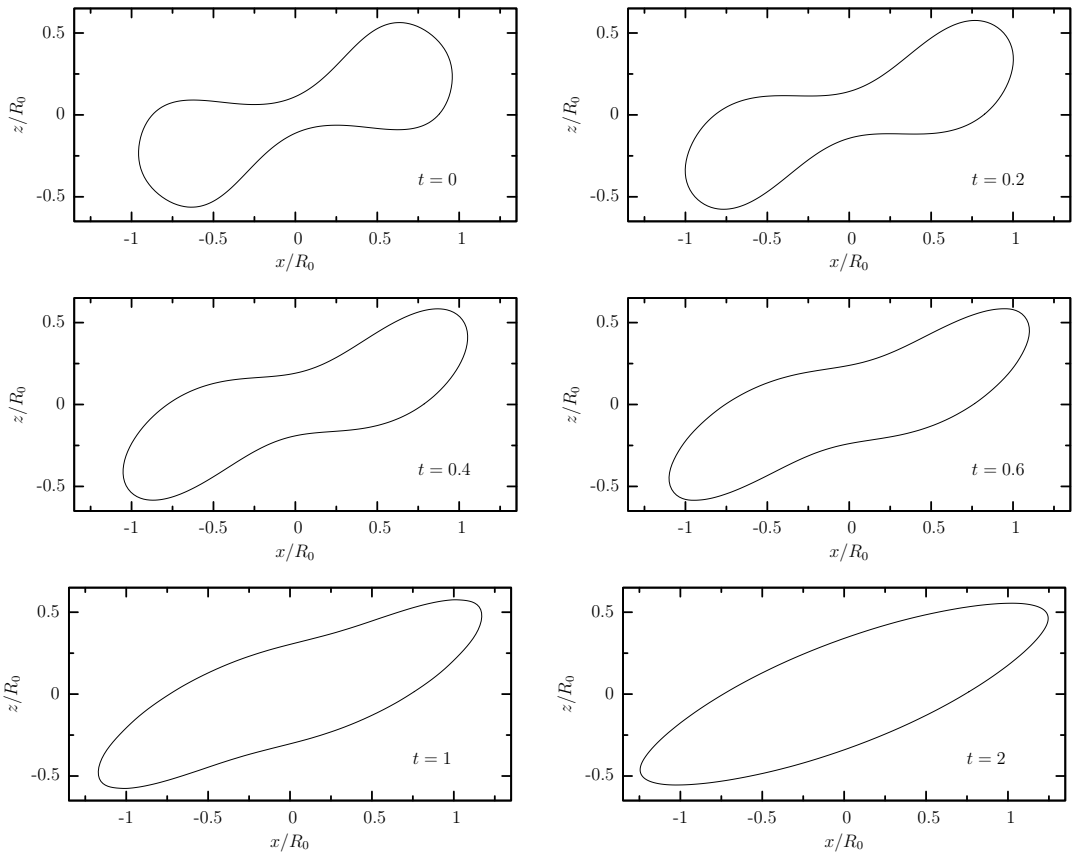


Figure 6.3: The cross section of the erythrocyte in the shear plane is shown at several times early in the deformation to illustrate the shape transition from a biconcave disc to an ellipsoid for $Ca = 1.5$ and $\lambda = 0.1$.

time scales are of the same order. An additional advantage is that prestress prevents local buckling, thus fulfilling the role of bending resistance for a system like the erythrocyte where the reduced bending modulus is very low.

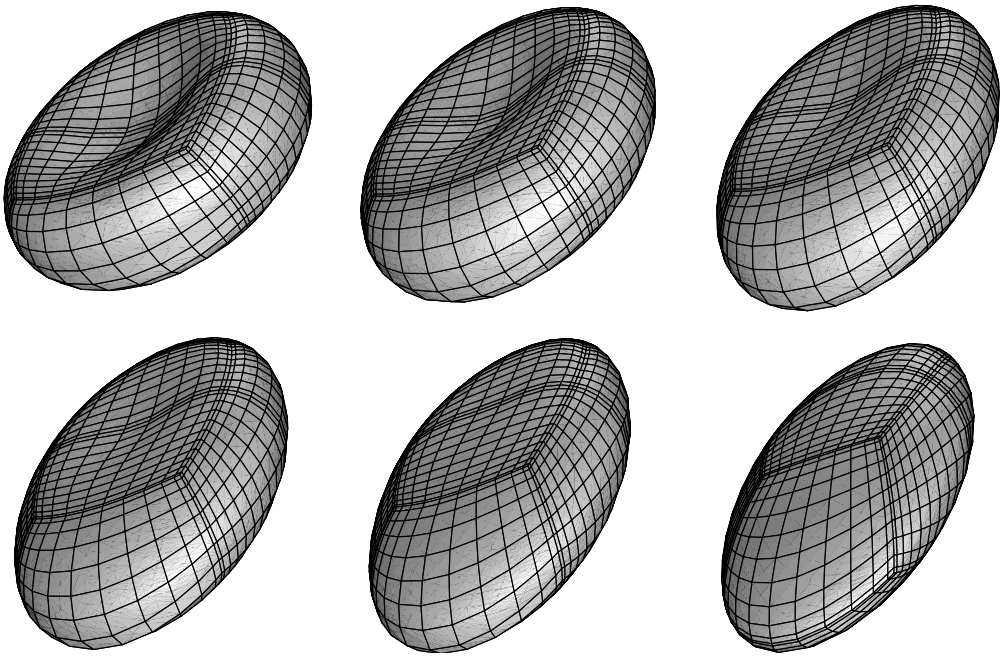

Figure 6.4: The geometry for the erythrocyte is shown slightly askew from the shear plane at several times $\{t = 0, 0.2, 0.4, 0.6, 1, 2\}$ early in the deformation to illustrate the shape transition from a biconcave disc to an ellipsoid for $Ca = 1.5$ and $\lambda = 0.1$.

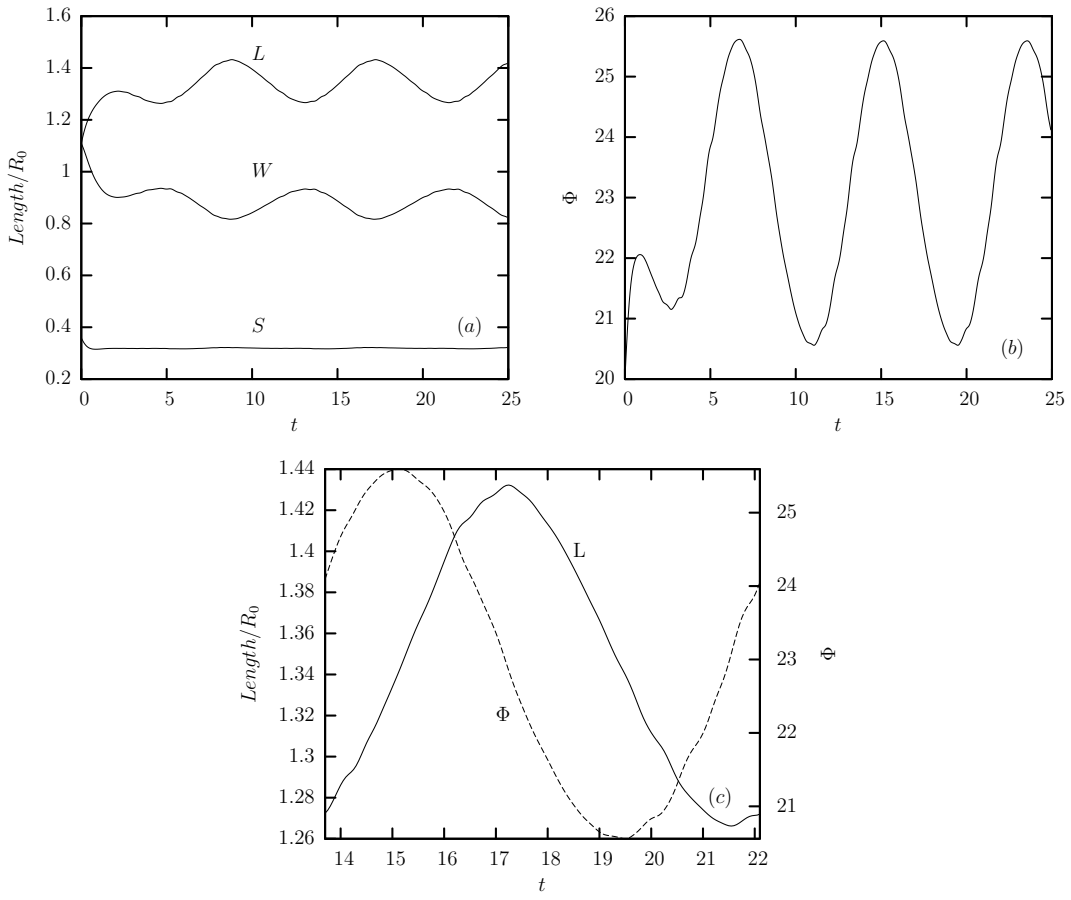


Figure 6.5: An erythrocyte in a simple shear flow, $Ca = 1.5$ and $\lambda = 0.1$. (a) The largest $L$ and intermediate $W$ normalized semi-axis lengths of the erythrocyte oscillate over time. The smallest length $S$ attains a steady-state and exhibits almost no oscillation. (b) The orientation angle $\Phi$ shown as a function of time also oscillates. (c) $L$ (——), and the orientation angle $\Phi$ (– – –), shown over one period. The phase lag is $\pi/2$, as predicted by Skotheim and Secomb [81].

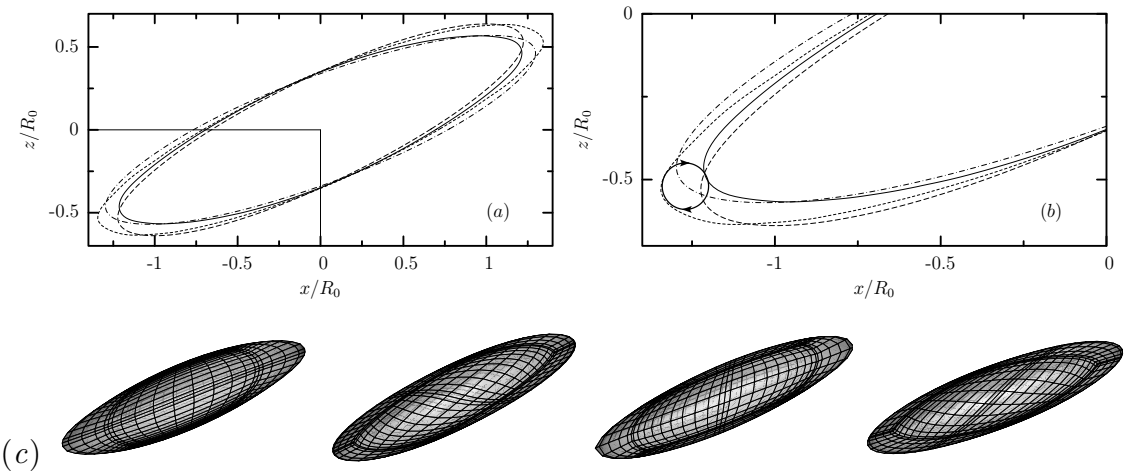


Figure 6.6: An erythrocyte in shear flow for $Ca = 1.5$ and $\lambda = 0.1$. (a) A cross-section in the shear plane at times $t = 13$ (——), 15 (– – –), 17 (- - - -), and 19 (– · –), representing one period of oscillation. By $t = 21.5$, not shown, the cross-section matches $t = 13$ again. (b) The delineated region from (a) magnified. The arrow indicates the direction of motion for the edge of the cross-sectional geometry. (c) The geometry shown at these four times illustrates that the period of oscillation corresponds to one-half of the tank-treading period.

## 6.3 Results From the Erythrocyte Model

The results in this chapter represent an erythrocyte with physiological geometric parameters [30] suspended in a simple shear flow $\boldsymbol{u}^{\infty} = G(z, 0, 0)$, as in Figure 1.1. For all simulations, $N_E = 10$ and $N_B = 12$. The time step is $\Delta t = 5 \times 10^{-4}$. As in previous chapters, all reported times are normalized with the shear rate. The initial position of the undeformed geometry is at an orientation angle $\Phi$ of 20 degrees in the shear plane. Area incompressibility is enforced with the adaptive prestress method described in Section 6.2. After an initial transient period, the erythrocyte assumes an ellipsoidal conformation [55]. Once the shape is ellipsoidal, the semi-axis lengths can be calculated accurately from the inertia tensor [48].

The transition from a biconcave disc to an ellipsoidal geometry happens from $t = 0$ to $t = 2$. This transition is illustrated in Figures 6.3 and 6.4. Following the transition, the erythrocyte tank-treads. However, unlike the case examined in previous chapters, in which the reference shape is spherical, the biconcave reference shape introduces periodic oscillations into the tensions produced as the deformed erythrocyte tank-treads; the dimpled regions of the original biconcave geometry deform differently than the edge regions as they pass around the surface contour. Thus, at steady-state, the lengths $L$ and $W$ of the deformed erythrocyte oscillate, as shown in Figure 6.5(a) for $Ca = 1.5$ and $\lambda = 0.1$, which is representative of the experimental systems discussed later. Its width $S$, after an initial transient period, exhibits minimal oscillation, remaining essentially fixed in time. The orientation angle in the xz-plane also oscillates, shown in Figure 6.5(b). Orientation angle in

the shear plane is calculated from the eigenvectors of the inertia tensor that lie in that plane.

The period $\Pi$ for the length and angle oscillations is the same, but there is a phase lag. Figure 6.5(c) displays the orientation angle and the largest semi-axis length, shown together over one period. The time length of the period is 8.4. The time lag between the peaks is 2.1, giving a phase lag of $\pi/2$ between the angle and length oscillations. This phase lag was predicted for erythrocytes in shear flow by Skotheim and Secomb [81]. As observed by those authors, this phase lag was also identified experimentally by Walter *et al.* for capsules with small deviations from sphericity [87]. This suggests that the $\pi/2$ phase lag may not be specific to the biconcave disc reference geometry, but rather may reflect deeper physical aspects of the capsule deformation problem in the nonspherical case.

Abkarian *et al.* [1] recently described the oscillation of the orientation angle in the plane of shear as a swinging motion. That is, the ellipsoid rocks back and forth between the maximum and minimum orientation angle. However, our SBE results reveal that the real dynamics are more complex. In Figures 6.6(a,b), we show the cross section in the shear plane for the deformed shape. Because of the phase lag between length and angle oscillations, the edge of the interfacial geometry traces an approximately circular path, illustrated in Figure 6.6(b). Figure 6.6(c) shows three dimensional images for the same times as in Figures 6.6(a,b). It is apparent from the images that the oscillation period for the lengths and angle corresponds to one-half of the tank-treading period, meaning that a material point moves halfway around the cell surface during one complete length or angle oscillation.

$(a)$

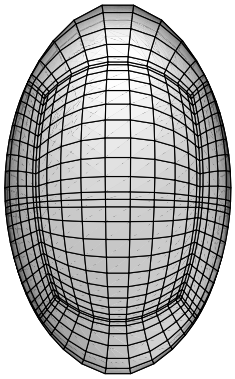

$(b)$

Figure 6.7: (a) An erythrocyte extended in the parallel-plate device of Dobbe *et al.* [27]. The erythrocyte is sheared between two parallel plates, and viewed from above the top plate. (b) An erythrocyte modeled with the SBE method, viewed in the xy-plane for one time instant ($\lambda = 0.1$, $Ca = 1.5$, $t = 17$).

### 6.3.1 Validation By Comparison To Ektacytometry

As discussed in Chapter 1, several diagnostic processes have been developed which attempt to quantify the deformability of the erythrocyte by observing the deformation behavior of individual cells, or average deformabilities for populations of cells. For both a light diffraction ektacytometer [40] and a counter-rotating parallel plate device [27], the flow pattern is a simple shear flow or a good approximation. In these studies, the flow strength is usually reported as the wall shear stress $\sigma_{wall}$. Letting $a$ again be the characteristic length scale, an expression can then be derived for the capillary number

$$Ca = \frac{a\sigma_{wall}}{G_s} \tag{3}$$

Because of the geometry of the ektacytometry systems, the deformed erythro-

cyte is not observed in the plane of shear. In our terminology, the plane of shear is the xz-plane, and $\boldsymbol{u}^{\infty} = G(z, 0, 0)$. Based on this definition, we can say that ektacytometry observes the deformed erythrocyte projected as an ellipse into the xy-plane, as illustrated in Figure 6.7. The deformation parameter computed from the largest and smallest semi-axes of this ellipse, and reported by researchers using ektacytometry, we will call $D_{xy}$. Because, as we have already seen, the erythrocyte has shape oscillations in shear flow, it is obvious that the deformation parameter from ektacytometry is averaged over time. Further, because this technique does not follow individual cells, $D_{xy}$ is also averaged over the erythrocyte population.

Figure 6.8 shows results from ektacytometry (dashed lines), compared with data produced through the SBE method (solid line with data points) for the time-averaged $D_{xy}$ for a range of moderate capillary numbers with $\lambda = 0.1$. Note that the viscosity ratio for ektacytometry systems usually ranges between 0.1 and 0.2. The $D_{xy}$ versus capillary number plots are visually indistinguishable for these two viscosity ratios, so we feel comfortable comparing all ektacytometry data to the case of $\lambda = 0.1$. Further discussion of the effect of viscosity ratio is presented in Section 6.3.4.

The value for the shear modulus commonly reported in the literature, and measured through micropipette aspiration, is $G_s = 6 \times 10^{-3}\ mN/m$ [56, 73, 77], but we find that the capillary numbers calculated with this value need to be translated along the x-axis. This suggests that the shear modulus we observe is somewhat less than the reported value. $G_s = 2.43 \times 10^{-3}\ mN/m$ produces an excellent fit of our data to the experimental results from Figure 6.8. The disparity between this

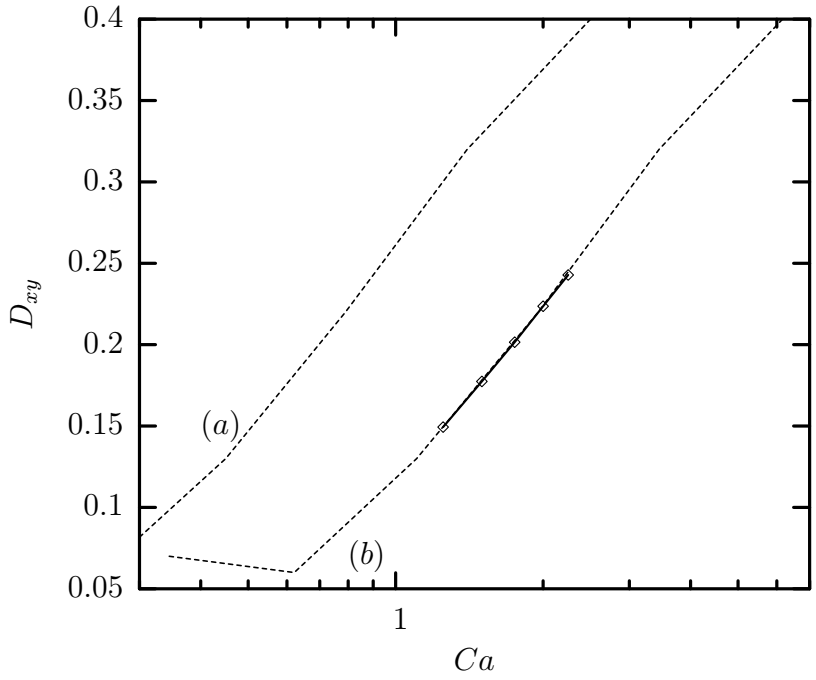


Figure 6.8: Ektacytometry results (dashed lines) for $D_{xy}$ reported by Hardeman *et al.* [40], converted to the capillary number domain using either (a) $G_s = 6 \times 10^{-3}\ mN/m$ or (b) $G_s = 2.43 \times 10^{-3}\ mN/m$. Also displayed as a solid line with data points is the average $D_{xy}$ for the oscillatory solution produced by the SBE method for $\lambda = 0.1$. Using $G_s = 2.43 \times 10^{-3}\ mN/m$, there is excellent agreement between the experimental and numerical results. For $1.25 \leq Ca \leq 2.25$, our data produces the regression line $D_{xy} = 0.3663\ \log(Ca) + 0.1133$ ($R^2 = 0.9999$).

value and the generally reported value of $G_s = 6 \times 10^{-3}\ mN/m$ bolsters the contention of Fischer, Skalak, and coworkers that the erythrocyte shear modulus may display strain dependent behavior [32]. The correspondence between our observations and previous experimental and theoretical predictions regarding erythrocyte shear modulus will be discussed further in Section 6.4.

Using $G_s = 2.43 \times 10^{-3}\ mN/m$, the SBE method captures two important aspects of the relationship between $D_{xy}$ and capillary number. First, the relationship is logarithmic for this range of capillary numbers. Second, using a logscale for capillary number, the SBE method produces a slope consistent with experimental results. Note that the logarithmic behavior is not observed for droplets or for spherical capsules. To the best of our knowledge, no previous numerical model has been able to reproduce real ektacytometry data.

### 6.3.2 The Deformability Distribution

In ektacytometry, the entire population is averaged together by the light scattering process. Because the cells are not synchronized, this also averages cellular deformation over the oscillation period. The second experimental setup, the counter-rotating parallel plate device, was designed by Dobbe *et al.* [27] to study the deformability differences within a population of erythrocytes. Note that they retain the geometric orientation of ektacytometry; that is, they still view the erythrocyte as an ellipse projected into the xy-plane. The viscosity ratio is consistent with ektacytometry, and the mean deformabilities they observed are consistent with

| Capillary Number | $D_{xy}$ Range |
|---|---|
| 1.25 | 0.127 |
| 1.50 | 0.128 |
| 1.75 | 0.128 |
| 2.00 | 0.127 |
| 2.25 | 0.126 |
| | |
| Dobbe 95 % Interval | 0.168 |

Table 6.1: $D_{xy}$ range for the SBE solution, determined from the data points in Figure 6.8. Range, calculated as maximum minus minimum $D_{xy}$, is essentially unchanged over this set of capillary numbers. Also shown is range computed from Table 3 by Dobbe *et al.* [27], using two standard deviations around the mean. The time oscillations can account for much of the experimentally observed variation.

ektacytometry [40]. Dobbe *et al.* designed their experiments so that they can capture data about individual erythrocytes within a population, but they do not follow or monitor individual cells over time. They compiled their results to produce deformability distributions for different shear stresses.

However, Dobbe *et al.* attribute the range of deformabilities they observe to inherent differences among the cells themselves. While these differences may exist, we have already observed that the deformation parameter for a single cell in shear flow oscillates over time. Dobbe *et al.* observe many cells, but they do not follow individual cells over time. It is possible therefore that some of the variation they observe is due to the oscillatory steady-state behavior. To examine the possible contribution of the oscillation to the range observed in the deformability distributions, we display in Table 6.1 the range, maximum $D_{xy}$ minus minimum $D_{xy}$, computed for each SBE data point from Figure 6.8. The range is essentially constant over this set of capillary numbers.

Dobbe *et al.* display in their Figure 3 and Table 4 results for a shear stress of 3 $Pa$, corresponding to $Ca \approx 3.5$, slightly above our upper limit for this viscosity ratio, but close enough so that the relative magnitudes of the deformability range can still be compared. Using the reported mean and standard deviation, we estimate a range for two standard deviations around the mean of 0.168 for the experimental results. The range produced by oscillation alone, with no inherent differences between erythrocytes within a population, is therefore 76% of the experimentally observed range. This indicates that the oscillation has a larger contribution to the range of deformabilities observed than was previously appreciated. Any researchers

who wish to study inherent differences between erythrocytes within a population in the future must therefore devise a way of monitoring individual cells over time.

### 6.3.3 Effects of the Flow Strength

As discussed in the comparison to ektacytometry experiments in Section 6.3.1, the deformation parameter $D_{xy}$ increases logarithmically with capillary number over the range of capillary numbers we observed. However, because the geometry is projected into the xy-plane, this gives only limited information about how the actual three-dimensional shape changes. The SBE method provides an opportunity to address through simulation this shortcoming of the experimental technique.

Figure 6.9(a) shows the semi-axis lengths from the inertia tensor, averaged over time for the steady-state solution, as a function of capillary number. Like the behavior observed with $D_{xy}$, the lengths change logarithmically over this range of capillary numbers. Again, this is consistent with experiments, but unlike the case with a spherical reference geometry. As expected, the largest semi-axis length $L$ increases with capillary number, as the shear flow extends the cell. However, with the biconcave disc, the intermediate length $W$ decreases with capillary number, and almost no change at all is observed in the smallest semi-axis length $S$. This is qualitatively different behavior from the spherical reference shape case, in which major changes were observed in the magnitude of the smallest length, and minor changes in the intermediate length. With a biconcave disc geometry, the thickness of the cell is essentially fixed, and does not change as a stronger flow extends the

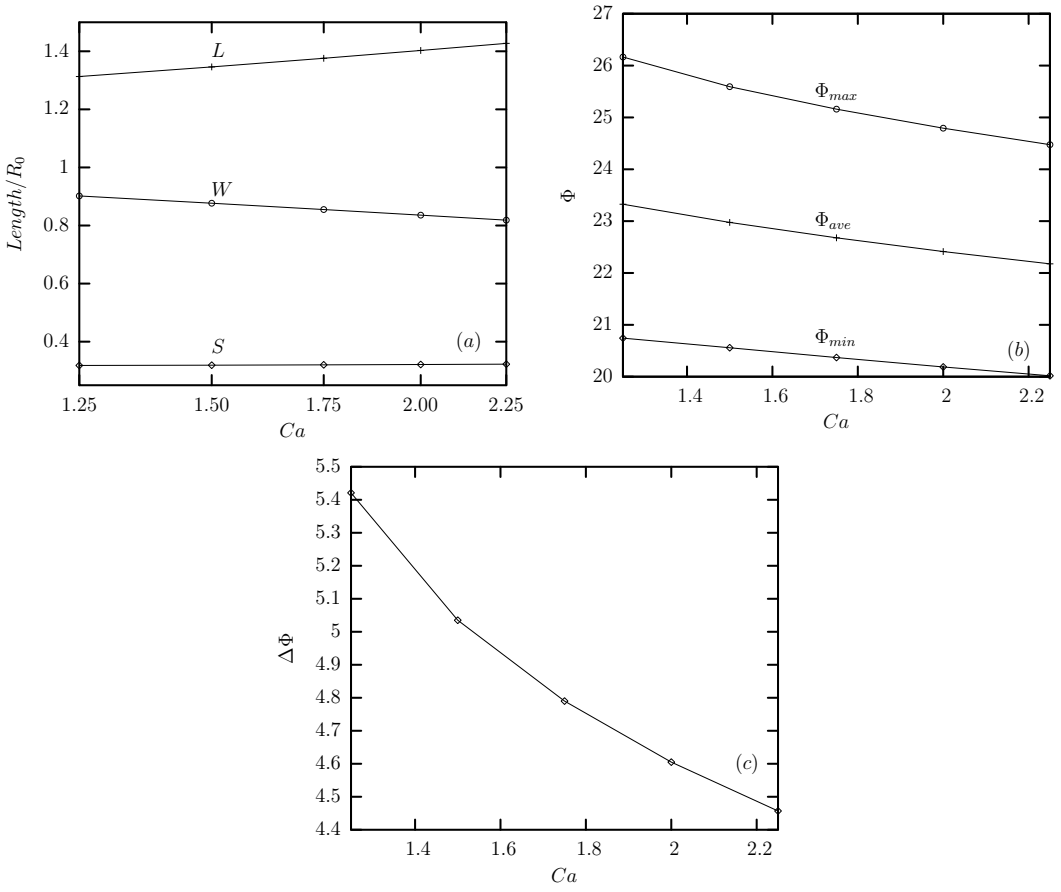


Figure 6.9: Erythrocyte deformation dynamics as a function of capillary number for $\lambda = 0.1$. (a) The normalized semi-axis lengths, averaged over time for the steady-state solution, as a function of capillary number. Like the $D_{xy}$ behavior observed in Figure 6.8, the lengths change logarithmically with capillary number over this range. The regression lines are $L = 0.4475\ \log(Ca) + 1.2685$ ($R^2 = 0.9996$), and $W = -0.3264\ \log(Ca) + 0.9340$ ($R^2 = -0.9999$). $S$ is essentially constant. (b) The maximum, time-averaged, and minimum orientation angles $\Phi$ decrease with capillary number. (c) The amplitude of the angle oscillations $\Delta\Phi$, defined as $(\Phi_{max} - \Phi_{min})$, decreases with capillary number.

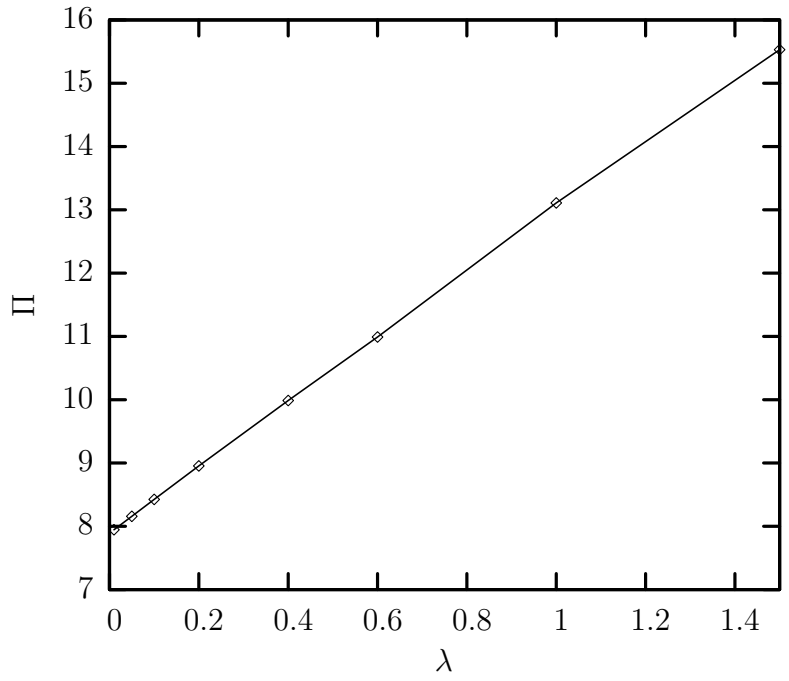


Figure 6.10: The oscillation period Π increases linearly with viscosity ratio $\lambda$, as illustrated for $Ca = 1.5$. The regression line is $P = 5.11\lambda + 7.92$ ($R^2 = 0.9999$).

cell.

The maximum, average, and minimum orientation angles decrease slightly with capillary number, as shown in Figure 6.9(b). The magnitude of the change over the range of capillary numbers we observed is less than the amplitude of the orientation angle oscillations. The amplitude of these oscillations also decreases with capillary number, shown in Figure 6.9(c). Increasing the flow rate appears to dampen the motion described by Abkarian *et al.* as swinging [1].

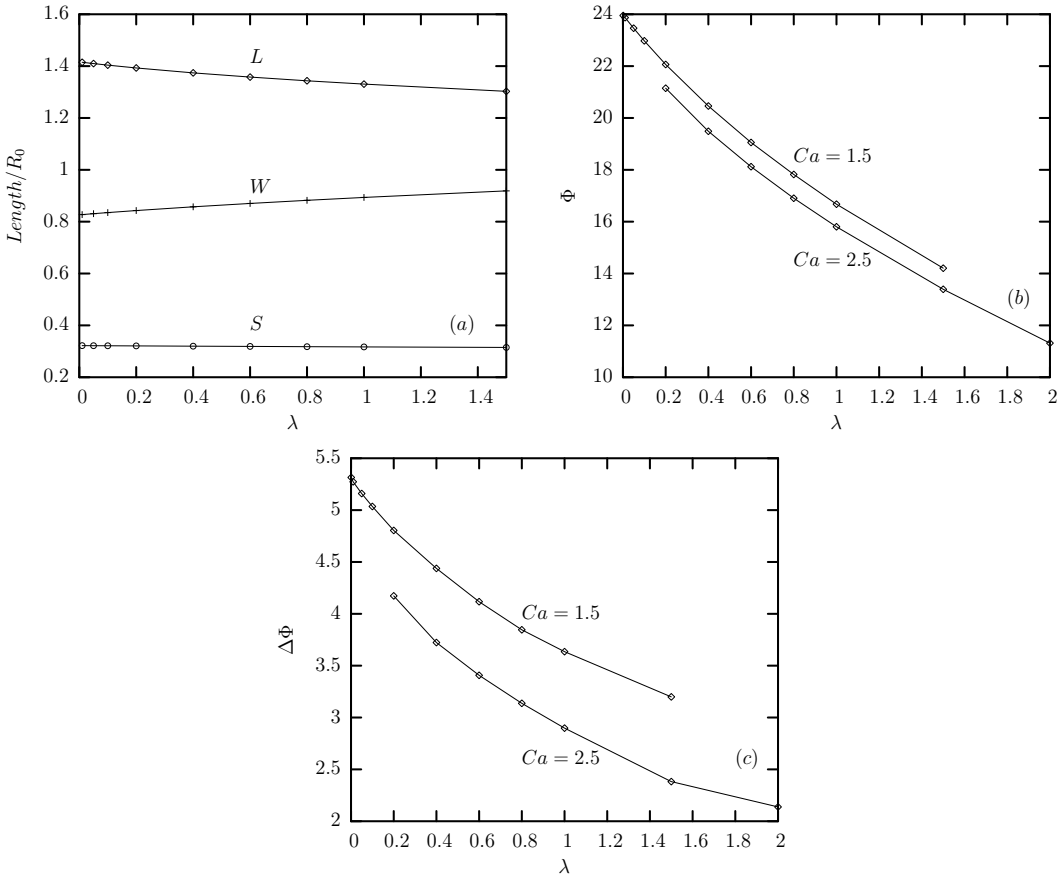


Figure 6.11: Erythrocyte deformation dynamics as a function of viscosity ratio. (a) The normalized semi-axis lengths for $Ca = 2$ averaged over time as a function of viscosity ratio. $L$ ($L = -0.0765\ Ca + 1.4096$; $R^2 = -0.9913$) and $W$ ($L = 0.0661\ Ca + 0.7707$; $R^2 = 0.9957$) decrease and increase, respectively, with increasing $\lambda$. $S$ is essentially unchanged. (b) The time-average orientation angle $\Phi$ as a function of $\lambda$ for $Ca = 1.5$ and $Ca = 2.5$. The orientation angle decreases much more rapidly with $\lambda$ than with $Ca$ (Figure 6.9(b)). (c) The range of the orientation angle oscillation $\Delta\Phi$ shown as a function of $\lambda$ for $Ca = 1.5$ and $Ca = 2.5$. Higher viscosity ratios dampen the orientation angle oscillation.

### 6.3.4 Effects of the Viscosity Ratio

The majority of experimental systems like ektacytometry operate in the range $0.1 < \lambda < 0.2$. Yet, the physiological value for a healthy human subject is closer to $\lambda \approx 5$ [56]. Therefore, here we use the SBE method to study the effect of increasing viscosity ratio on the erythrocyte deformation behavior. It is well known that at high viscosity ratio in shear flow erythrocytes transition from tank-treading to tumbling [1, 68, 81]. Our goal therefore is to examine the changes that occur first within the tank-treading regime, and then as the transition to tumbling occurs.

First, because the time scale for the flow increases with viscosity ratio, the tank-treading period $\Pi$ also increases with viscosity ratio. Figure 6.10 shows that the relationship between $\Pi$ and $\lambda$ is linear. Also apparent from the figure, as $\lambda$ approaches zero, the period approaches a minimum period of approximately 7.9.

The average lengths of the erythrocyte, shown in Figure 6.11(a), show that, at constant flow rate, the cell becomes less deformed as the viscosity ratio increases. That is, when $\lambda$ increases, the largest semi-axis $L$ contracts, and the intermediate one $W$ grows. As in the case of increasing capillary number, the smallest semi-axis changes only minimally. It appears fixed with viscosity ratio, just as it was fixed with both time and capillary number. The average orientation angle $\Phi$ decreases with the viscosity ratio, as observed in Figure 6.11(b), and the extent of the decrease is much greater than was observed with increasing capillary number over the range of capillary numbers shown in Figure 6.9(b). Increasing the viscosity ratio also dampens the angle oscillation, or swinging motion, as seen in Figure 6.11(c). The

overall effect is to bring the ellipsoid in the shear plane closer and closer to the horizontal orientation as $\lambda$ increases.

It is well-known that the erythrocyte undergoes a transition from tank-treading to tumbling at high viscosity ratios [81]. However, the mechanisms of this transition remain unclear. With the knowledge that the orientation angle decreases with increasing viscosity ratio (Figure 6.11(b,c)), our results suggest that, as the viscosity ratio increases, the cell swings closer to the horizontal axis. Eventually, it may reach a tipping point, beyond which it cannot return to the tank-treading orientation, and so it begins to rotate as a rigid body. The transition from tank-treading and swinging to tumbling can be observed in Figure 6.12. Here, using a capillary number of $Ca = 2$, the orientation angle is shown as a function of time for viscosity ratios $\lambda = 0.1, 1, 2$, and 5. For the smallest three viscosity ratios, the angle begins to oscillate around an average value. As the viscosity ratio increases, the average value drops. The evolution of the angle in the case of $\lambda = 5$ begins similarly, but now the average angle has dropped to such an extent that the angle becomes less than zero. In this case, the geometry of the shear flow ensures that, instead of returning, it continues to rotate. Thus the cell tumbles.

## 6.4 Conclusions Regarding Erythrocyte Modeling with SBE

In this chapter, the SBE method for elastic capsules has been extended by using prestress to enforce area incompressibility. This implementation of SBE, when applied to biconcave discoid initial and reference geometries, accurately reproduces

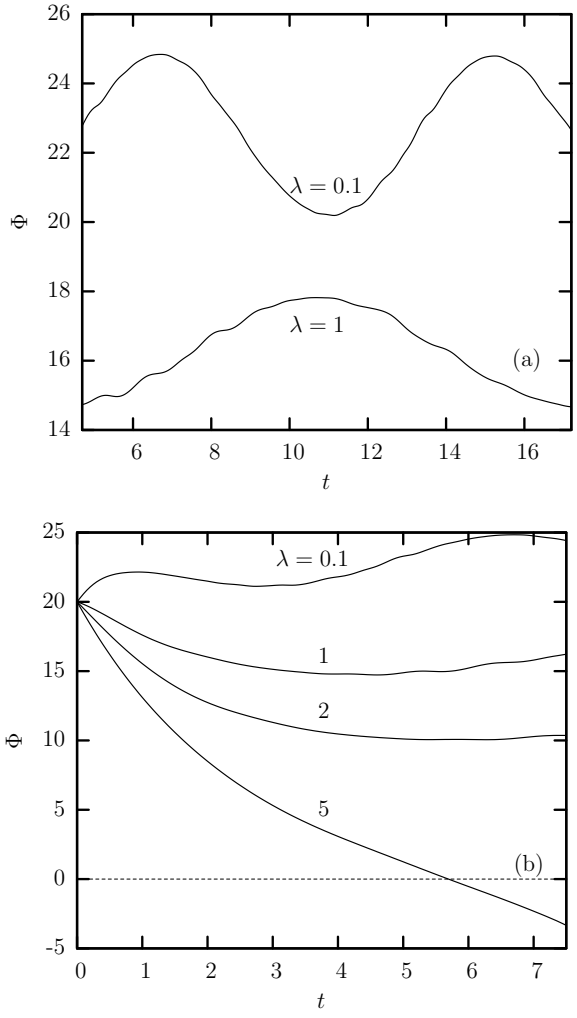


Figure 6.12: The orientation angle $\Phi$ in the shear plane for $Ca = 2$ as a function of time. (a) Shown over one period for $\lambda = 1$ and $\lambda = 0.1$ illustrates that increasing the viscosity ratio decreases the average angle, dampens the oscillation, and increases the oscillation period. (b) Examining the initial behavior of the angle with viscosity ratio $\lambda = 0.1, 1, 2, 5$, these trends continue, eventually resulting in the transition from tank-treading and swinging to tumbling.

experimental data for erythrocyte deformation in an ektacytometer. To the best of our knowledge, no previous numerical method has been able to reproduce real ektacytometry data.

The SBE method allows analysis of the deformation dynamics beyond the geometric constraints inherent in ektacytometry and other experimental techniques. It allows true visualization of the three-dimensional oscillatory behavior over a range of capillary numbers and viscosity ratios. Several conclusions can be drawn. First, because the flow is oscillatory, much of the variation observed in parallel-plate viscometry systems [27] could be due not merely to differences between individual cells, but also to the time-variant oscillatory behavior described by Abkarian *et al.* [1] as swinging. To verify this experimentally, it would be necessary to track and monitor individual cells over time.

Second, the SBE method demonstrates that the smallest dimension $S$ of the tank-treading erythrocyte, which exists in the shear plane, is invariant in time, capillary number, and viscosity ratio. Therefore, the shape changes observed as time oscillations, and also the changes with capillary number and viscosity ratio, occur with respect to $L$ and $W$. Fixed $S$ behavior has not been previously observed with spherical elastic capsules or droplets, and appears to be a result of the biconcave disc reference geometry. $S$ has a normalized magnitude of approximately 0.32, corresponding to a real cell thickness of 2.5 $\mu m$. It is interesting the note that this value is only slightly less than constrictions commonly observed in the capillary, which can often be as small as 4 $\mu m$ in diameter [77].

Third, by studying the deformation behavior with increasing viscosity ratio,

the SBE method has elucidated linkages between the orientation of the erythrocyte in the shear plane and the transition to tumbling. In particular, we show that tumbling is not a radically new behavior which suddenly appears at higher viscosity ratios. Rather, it is an extension of a trend observed with increasing viscosity ratio; the maximum, average, and minimum orientation angles decrease with increasing viscosity ratio. Because the minimum angle cannot decrease below zero and return to a positive angle orientation, the cell reaches a tipping point, and begins tumbling.

Finally, the value of erythrocyte surface shear modulus $G_s$ measured through micropipette aspiration and most commonly reported in the literature is $G_s = 6 \times 10^{-3}\ mN/m$ [56, 73, 77]. Years ago, Fischer, Skalak, and coworkers [32] noted that this experimental technique only produces stretch ratios $\lambda_\alpha$ in the range of 2-4, and predicted that $G_s$ decreases at smaller shear deformations. Fischer *et al.* suggested a value of $G_s = 2 \times 10^{-3}\ mN/m$ for stretch ratios $\lambda_\alpha \approx 1.3$, assuming a biconcave disc unstressed configuration (It has since been confirmed that the biconcave disc shape is indeed unstressed [33]). Our comparison to ektacytometry data from Hardeman *et al.* [40], shown in Figure 6.8, indicates that the surface shear modulus $G_s$ which fits the experimental data to the results from SBE modeling is $G_s = 2.43 \times 10^{-3}\ mN/m$, remarkably close to the prediction made by Fischer *et al.*. Recent work by Abkarian *et al.* also derived an erythrocyte shear modulus less than the value obtained through aspiration [1]. Together, their analysis and our own support the hypothesis of Fischer and coworkers that the shear modulus is strain-dependent, and that it reduces at small deformations.

# Chapter 7

# Additional Erythrocyte Investigations

In Chapter 6, the Spectral Boundary Element method was extended via a novel implementation of membrane prestress to model the erythrocyte. Over a range of moderate capillary numbers, the extended SBE method produces an oscillatory solution for erythrocyte deformation in a linear shear flow. As shown in Figure 6.8, the results were in excellent agreement with experimental data from ektacytometry. The simulation allowed us to go beyond the geometric limitations of past experimental systems to examine the complete three-dimensional deformation behavior of erythrocytes in shear flow. In this chapter, we study two additional problems: 1) erythrocyte deformation in a planar extensional flow, and 2) the deformation of swollen erythrocytes in shear flow, as compared to normal, healthy cells.

All results presented in this chapter were produced via the SBE erythrocyte model from Chapter 6. In all cases, $N_E = 10$ and $N_B = 12$. The time step is $\Delta t = 5 \times 10^{-4}$.

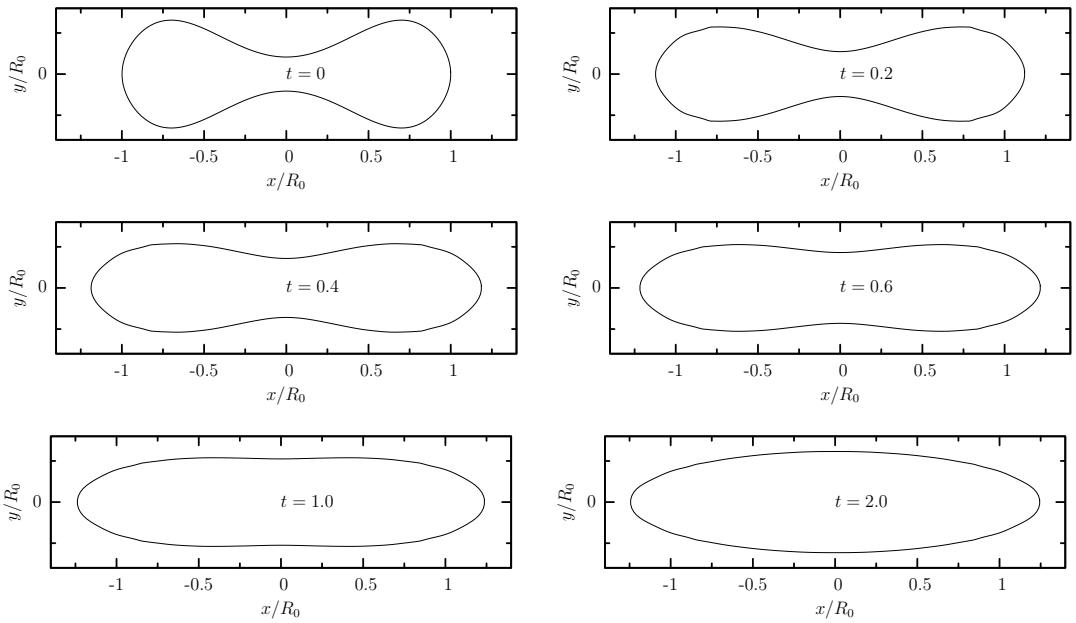


Figure 7.1: The cross section of the erythrocyte in the extensional plane is shown at several times early in the deformation to illustrate the shape transition from a biconcave disc to an ellipsoid for $Ca = 0.2$ and $\lambda = 1$.

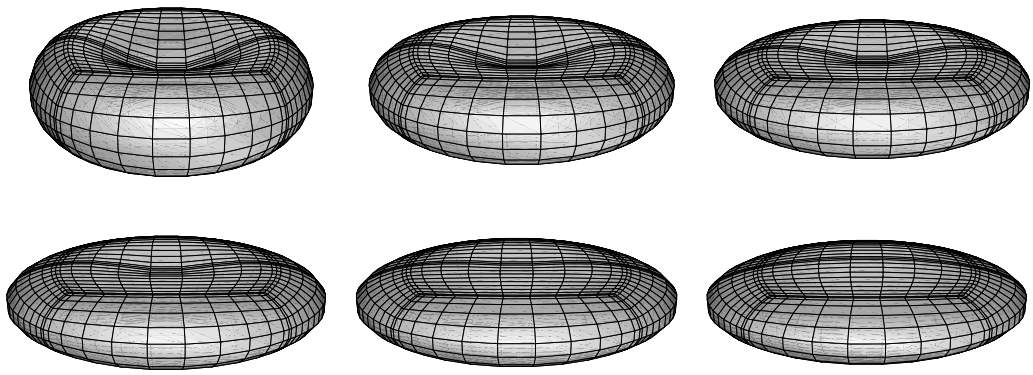

Figure 7.2: The geometry of the erythrocyte is shown slightly askew from the extensional plane at several times $\{t = 0, 0.2, 0.4, 0.6, 1, 2\}$ early in the deformation to illustrate the shape transition from a biconcave disc to an ellipsoid for $Ca = 0.2$ and $\lambda = 1$.

## 7.1 Erythrocytes in a Planar Extensional Flow

The first set of experiments investigate the behavior of an erythrocyte deforming in a planar extensional flow field. This flow pattern, shown in Figure 4.1, was previously examined with elastic, spherical capsules in Chapters 4 and 5. We observe that the erythrocyte loses its biconcave disc shape, and transitions to an ellipsoidal conformation, even at low flow rates. This transition is illustrated for $Ca = 0.2$ in Figures 7.1 and 7.2. Therefore, like in the shear flow erythrocyte studies of Chapter 6, length values calculated via the inertia tensor accurately reflect the real semi-axis lengths after an initial transient period.

Figure 7.3 shows the normalized semi-axes length $L$, width $S$, and depth $W$ as a function of time for several capillary numbers. The capillary numbers chosen

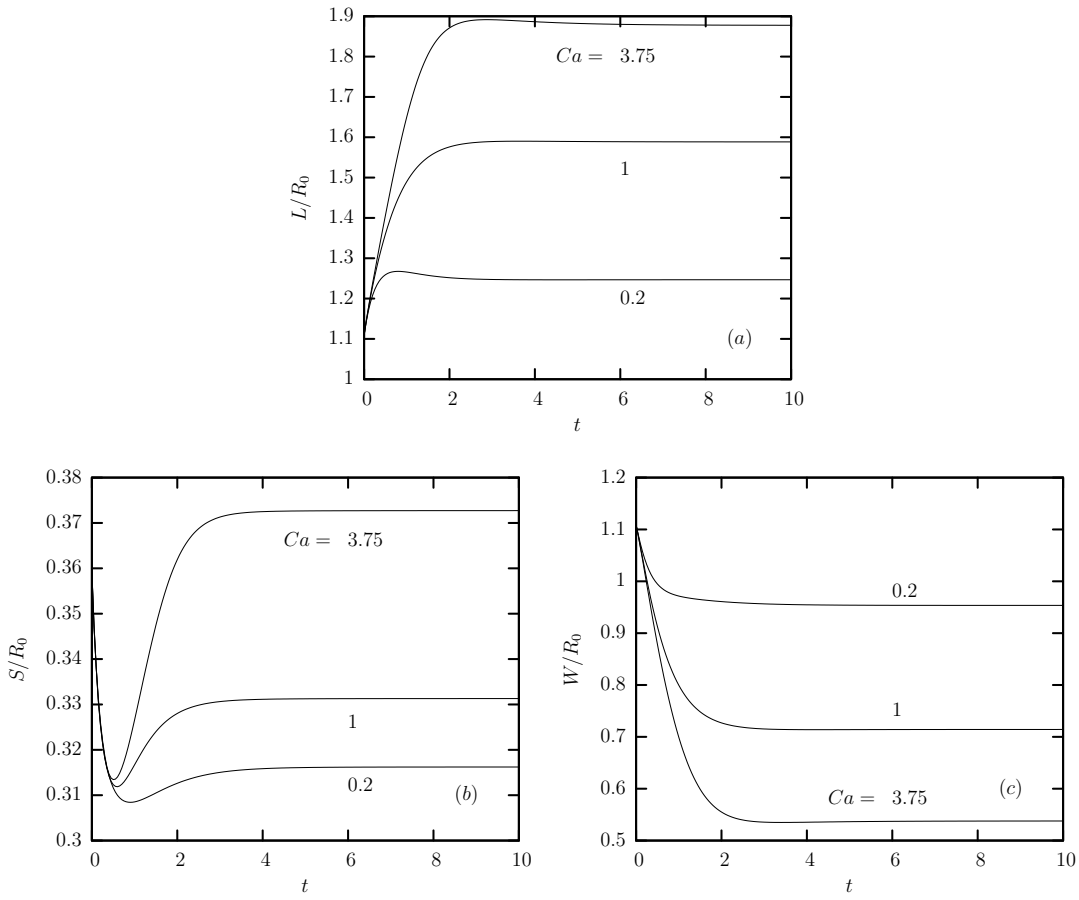


Figure 7.3: Erythrocyte deformation in an extensional flow as a function of time. Semi-axis lengths (a) $L$, (b) $S$, and (c) $W$ are shown as a function of time.

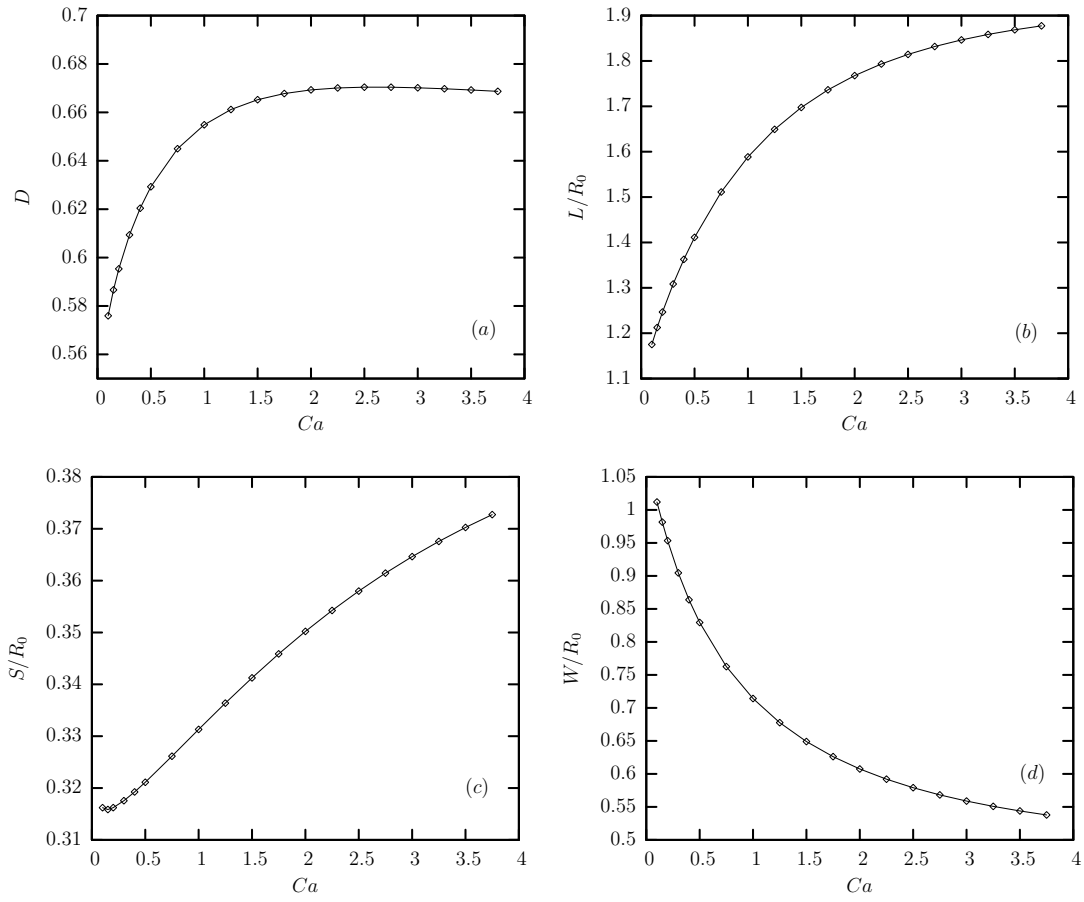


Figure 7.4: Erythrocyte deformation in an extensional flow as a function of capillary number. (a) Deformation $D$, and normalized semi-axis lengths (b) $L$, (c) $S$, and (d) $W$. The overall deformation $D$ plateaus near $Ca = 2$. The rate of change for $L$ and $W$ slows down with increasing capillary number, suggesting they may also reach an upper limit at higher capillary numbers.

are $Ca = 0.2$, representative of weak flows, $Ca = 1$, a moderate flow rate, and $Ca = 3.75$, a strong flow near the upper stability limit for our method. Over this range of capillary numbers, the SBE method reaches a stable, steady-state configuration. Because of the area incompressibility condition enforced via prestress, no cusped shapes are observed analogous to the tips seen with spherical, Skalak capsules.

The trends with capillary number of the semi-axes and the deformation $D$ are shown in Figure 7.4. The deformation parameter $D$, in Figure 7.4(a) appears to reach an asymptotic limit of approximately $D \approx 0.67$ for $Ca \geq 2$. The erythrocyte length $L$ increases monotonically, as shown in Figure 7.4(b). The shape of the curve indicates that it may also be approaching an asymptotic limit, but unfortunately the present method is unable to verify this. The thickness $S$ changes slightly (Figure 7.4(c)), while the depth $W$ decreases monotonically, as shown in Figure 7.4(d); like $L$, the depth $W$ may be approaching a limit at high flow rates.

Comparing the behavior of erythrocytes in the two different flow patterns for which we have results, i.e. a simple shear flow and a planar hyperbolic extensional flow, certain differences are obvious; in shear flow, the erythrocyte tank-treads, and the lengths oscillate, while in extensional flow, the undisturbed flow field lacks a rotational component, and therefore there is no rotation or oscillatory behavior in the solution. However, in both flow fields, the erythrocyte assumes an ellipsoidal geometry under proper flow conditions. We therefore decided to study how the semi-axes of these ellipsoids relate to one another, for the two different flow fields.

Figure 7.5(a) shows the smallest semi-axis length $S$ as a function of the largest

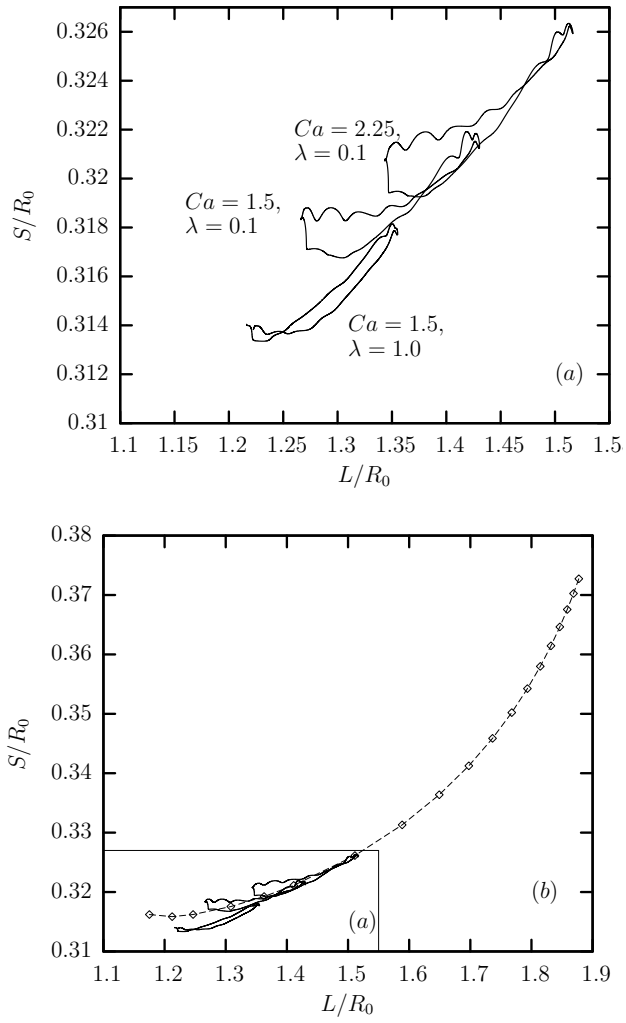


Figure 7.5: (a) For the shear flow results presented in Chapter 6, the smallest semi-axis $S$ is shown as a function of the largest semi-axis $L$ over one period of oscillation for several capillary numbers. Because the erythrocyte response to the flow is oscillatory, the graph produces a closed loop. (b) The shear flow results (solid line) from (a) are shown along with the steady-state $S$ versus $L$ values for erythrocytes in a planar extensional flow (dotted line).

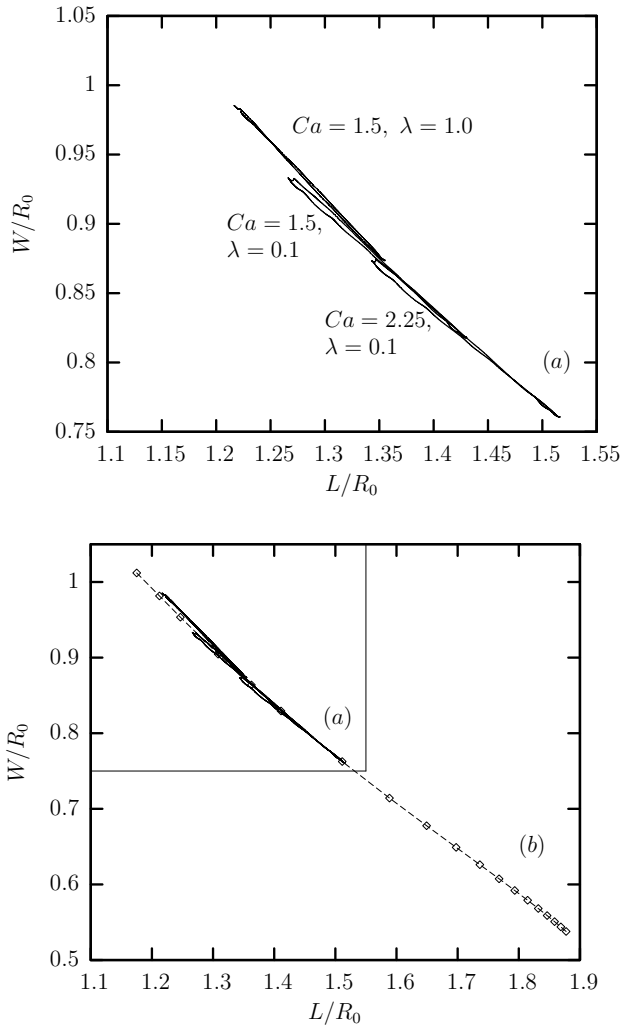


Figure 7.6: (a) For the shear flow results presented in Chapter 6, intermediate semi-axis $W$ is shown as a function of the largest semi-axis $L$ over one period of oscillation for several capillary numbers. Like Figure 7.5(a), these shear flow results are a closed loop, but they appear as lines because the $W$ versus $L$ data retraces the same path twice during one period of oscillation. (b) The shear flow results (solid line) for $W$ as a function of $L$ from (a) are shown along with the steady-state $W$ versus $L$ values for erythrocytes in a planar extensional flow (dotted line).

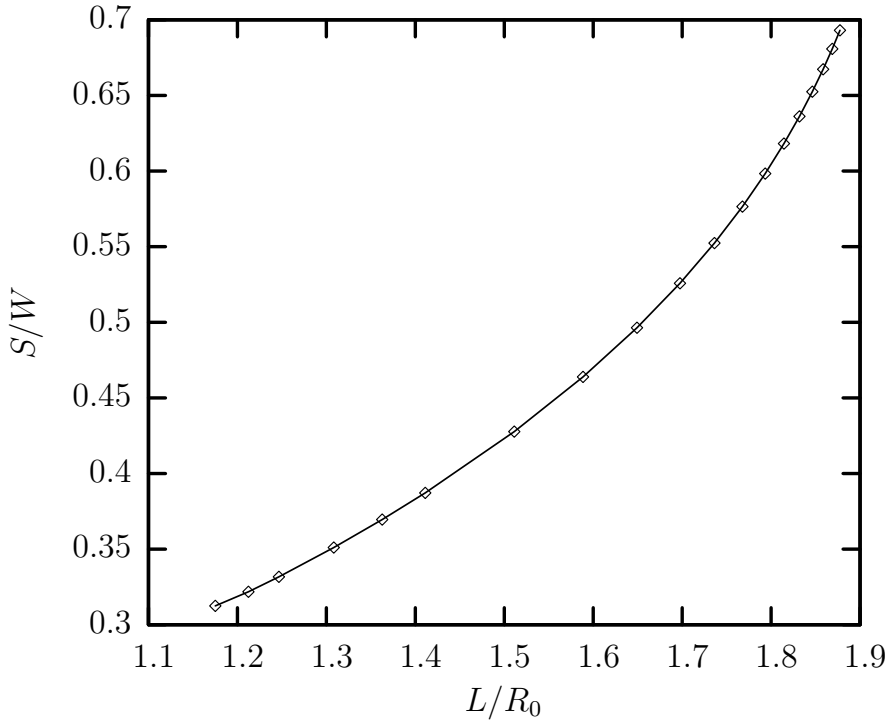


Figure 7.7: The ratio of $S/W$ is shown as a function of $L$ for erythrocytes in a planar extensional flow. This ratio increases towards 1 as the extension increases, indicating that the lateral (zy) cross-section is becoming more circular.

length $L$ for an erythrocyte in shear flow from Chapter 6, plotted over one period of oscillation for several sets of parameters. Because the semi-axis lengths of an erythrocyte oscillate in shear flow, as shown in Figure 6.5(a), plotting $S$ as a function of $L$ produces a closed loop in each case. Figure 7.5(b) shows the shear flow results (solid line) from Figure 7.5(a) along with data for the steady-state results for erythrocytes in a planar extensional flow (dotted line). The data sets for the steady-state behavior for extensional flow and the transient, oscillatory behavior for shear flow are seen to overlap, with similar magnitudes and trends.

Figure 7.6 repeats this analysis for $W$ as a function of $L$. Figure 7.6(a) shows $W$ as a function of $L$ for shear flow, plotted over one period of oscillation for the same sets of parameters as in Figure 7.5(a). These appear more as lines than loops, because the path in the second half of an oscillation period is essentially the reverse of the path traveled in the first half for $W$ considered as a function of $L$. The shear flow results are shown along with extensional flow steady-state results in Figure 7.6(b), and once again the results for shear flow over one period of oscillation are congruent with the extensional flow steady-state results.

Finally, we examined the ratio $S/W$ as a function of extension $L$. Figure 7.7 shows this ratio for the range of capillary numbers we have studied. The ratio increases towards 1 at large extensions, indicating that the cross-section perpendicular to the direction of extension is becoming more circular.

### 7.1.1 Erythrocytes in Extensional Flow Conclusions

Comparing the magnitudes of the shortest $S$ and intermediate $W$ semi-axis lengths, relative to the longest $L$, as we do in Figures 7.5 and 7.6, suggests that the set of possible geometric conformations that can be produced via flow-induced deformation is limited. That is, given a value for $L$, the values of $S$ and $W$ are largely predetermined. This is particularly true for the intermediate length $W$.

It is also clear that $S$, which in the shear flow investigations of Chapter 6 was thought to be constant, actually does change at larger cellular extensions. Based on our observations in this chapter, we predict that $S$ would increase at larger shear-induced deformations than we were able to produce in Chapter 6. We further predict, based on examining the ratio $S/W$, that the cross-section perpendicular to the largest semi-axis length will become more circular at large extensions.

These conclusions indicate that the flow pattern used to investigate the flow-induced deformation of an erythrocyte may be largely irrelevant. This agrees with the finding of Shin *et al.*, displayed in their Figure 5, that the cellular deformation for erythrocytes in microchannel systems is approximately the same as that in shear flow systems at the same wall shear stress [78]. This information is advantageous for experimental researchers, because it indicates that the information that could be obtained from large-deformation investigations in an extensional flow may be obtained equally well by continued investigation in shear flow systems. This is important because extensional flow experiments at high flow rates are technically difficult due to the instability of the central stagnation point [18]. Shear flow experiments with

erythrocytes, in contrast, have a long and successful history [11, 12, 27, 28, 40].

## 7.2 Deformation of Swollen Erythrocytes in Shear Flow

Here we have investigated the deformation of osmotically swollen erythrocytes in a simple shear flow $\boldsymbol{u}^{\infty} = G(z, 0, 0)$. We have used the geometric parameters $R_0 = 3.80\ \mu m$, $C_0 = 2.10\ \mu m$, $C_2 = 7.58\ \mu m$, and $C_4 = -5.59\ \mu m$, which are representative of a hypotonic osmolarity of 217 $mO$ [30].

The primary effect of swelling on the undisturbed shape is to increase the thickness, while leaving $R_0$ mostly unaffected. This effect is preserved in the deformed shape. Figure 7.8(a) shows the normalized semi-axis lengths for a swollen erythrocyte with $Ca = 1.5$ and $\lambda = 0.1$, with the results for a normal erythrocytes shown as dotted lines for purposes of comparison. Although the period $\Pi$ and phase are slightly different for lengths $L$ and $W$, the swelling appears to have only marginal affect on the average magnitude and amplitude of oscillation for these two semi-axis lengths. The swelling does increase $S$ significantly, although it still exhibits little oscillation in time. The second major effect of the swelling, besides increasing $S$, is to increase the orientation angle $\Phi$ compared to that of normal cells, as seen in Figure 7.8(b). The amplitude of the angle oscillation also increases slightly.

Figure 7.9 show the semi-axis lengths, angle $\Phi$, and the amplitude of the angle oscillation over a range of capillary numbers for $\lambda = 0.1$. It is immediately apparent that the swelling broadens the range of capillary numbers for which our method produces a stable oscillatory solution at this viscosity ratio, and this is because the

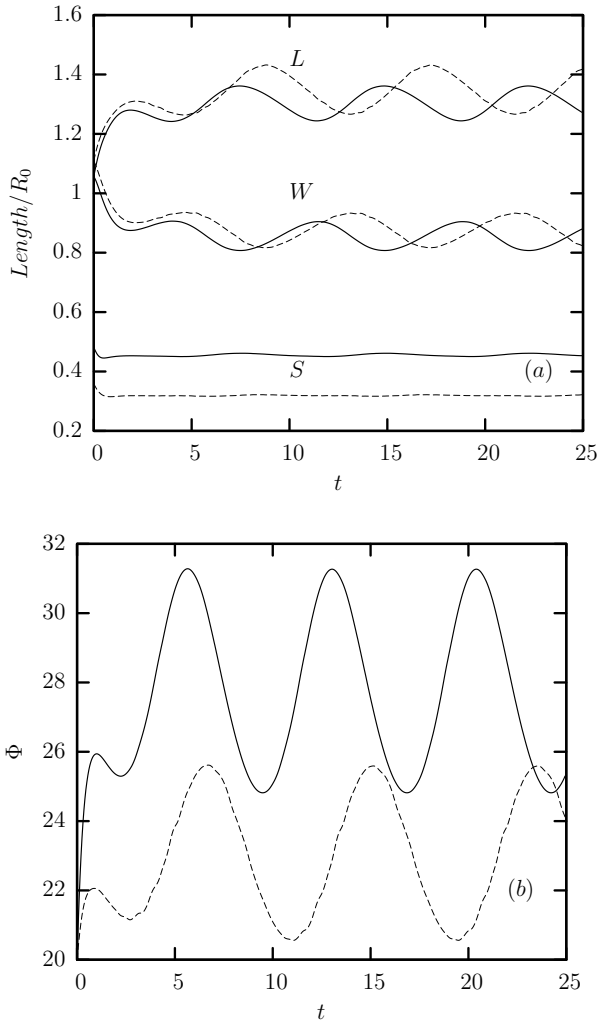


Figure 7.8: A swollen erythrocyte (solid lines) deforming in a shear flow for $Ca = 1.5$, $\lambda = 0.1$. The results from Chapter 6 for a physiologically normal cell (dotted lines) at the same parameters are also shown for purposes of comparison. (a) Normalized semi-axis lengths $L$, $W$, and $S$ are shown as a function of time. (b) The orientation angle $\Phi$ for the swollen (solid line) and normal (dotted line) erythrocytes are shown as a function of time.

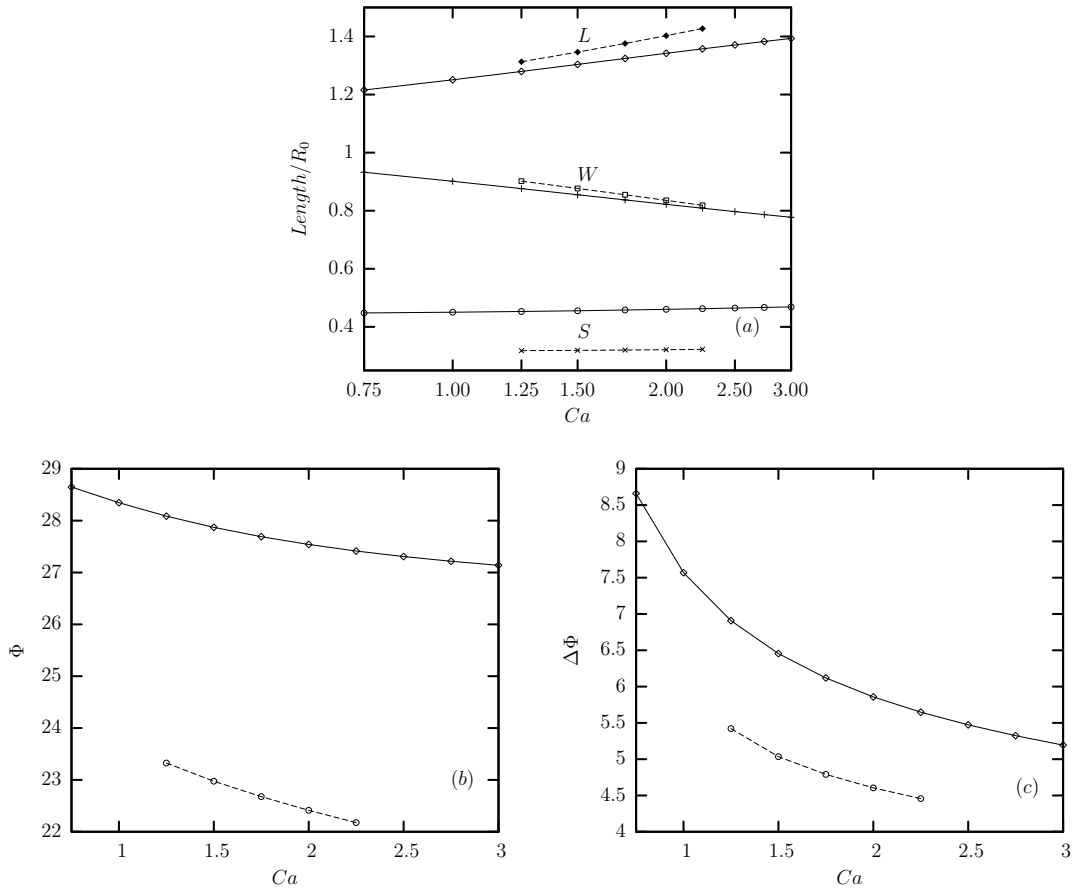


Figure 7.9: Deformation of swollen (solid lines) and normal (dotted lines) cells as a function of capillary number for $\lambda = 0.1$, chosen to study pure tank-treading behavior. (a) Normalized semi-axis lengths $L$, $W$, and $S$, b) the orientation angle $\Phi$, and (c) the amplitude of angle oscillation, defined as $(\Phi_{max} - \Phi_{min})$.

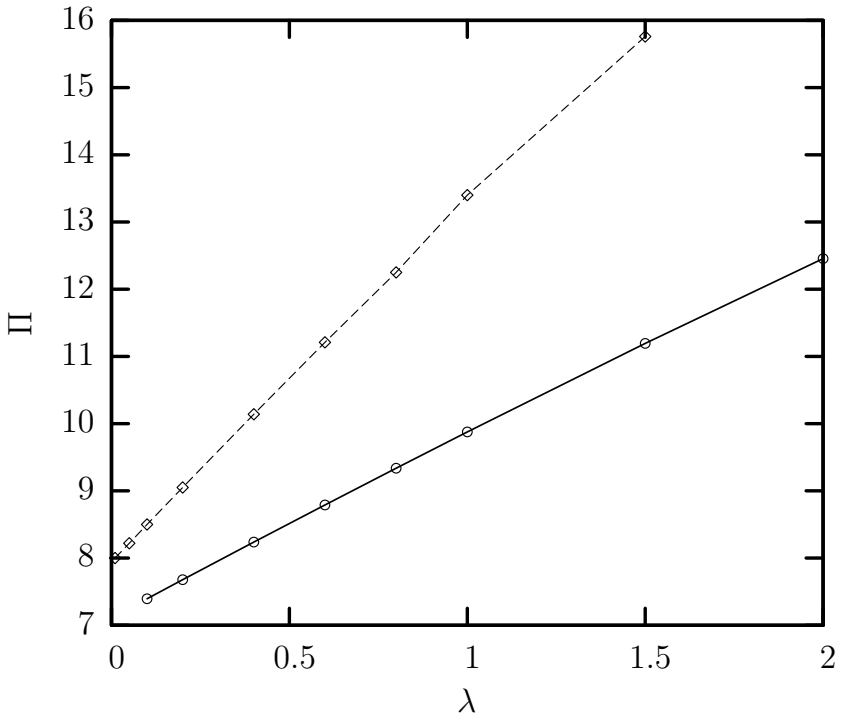


Figure 7.10: The oscillation periods Π for swollen (solid line) and normal (dotted line) erythrocytes are shown as a function of viscosity ratio $\lambda$ for $Ca = 2$.

decreased surface area to volume ratio makes the formation of surface instabilities less likely. For the normal cells, with $\lambda = 0.1$, the SBE method for erythrocytes produces stable solutions for the range $1.25 \leq Ca \leq 2.25$, while for the swollen cells under similar conditions, the method is stable for $0.75 \leq Ca \leq 3$. The trends of all three semi-axis lengths appear similar, as seen in Figure 7.9(a), but the smallest length, as seen previously in Figure 7.8(a), is increased in the swollen cells compared to the normal cells. The orientation angle $\Phi$ and amplitude of angle oscillation also increase over the entire range of capillary numbers relative to normal cells, as seen in Figures 7.9(b,c).

We have observed already from Figure 7.8(a) that the swollen cells have a slightly different oscillation period $\Pi$. To examine this more closely, we plot $\Pi$ as a function of viscosity ratio $\lambda$ for $Ca = 2$ for both swollen and normal cells in Figure 7.10. The results indicate that the swelling has two effects on the oscillation period; first, it lowers the low-viscosity limit for oscillation period, which in this figure is represented by the y-axis intercept, and second, it lowers the slope, the rate at which period increases with increasing $\lambda$. The phase lag between length and orientation angle $\Phi$ oscillations, not shown, remains $\pi/2$, as observed with normal cells in Chapter 6 and predicted by Skotheim and Secomb [81].

The trends for the swollen cells with increasing viscosity ratio $\lambda$ are shown in Figure 7.11(a-c), with respect to semi-axis lengths, angle $\Phi$, and amplitude of $\Phi$ oscillation. For the most part, the trends here also appear to follow the trends for the normal cells, with elevated $S$, $\Phi$, and amplitude of $\Phi$ oscillation. The low-viscosity limit of $L$ for the swollen cells is slightly depressed compared to the normal cells, and $W$ increases slightly slower with increasing $\lambda$ for the swollen cells.

### 7.2.1 Swollen Erythrocyte Conclusions

Several disease states are associated with a change in the surface area to volume ratio of the erythrocytes, including hereditary elliptocytosis and spherocytosis [38, 56]. It is well known that the deformability of affected erythrocytes is reduced in experimental systems including ektacytometry [20] and parallel plate shearing [27]. Similar effects can be observed by treating the erythrocytes with thermal [41, 55] or

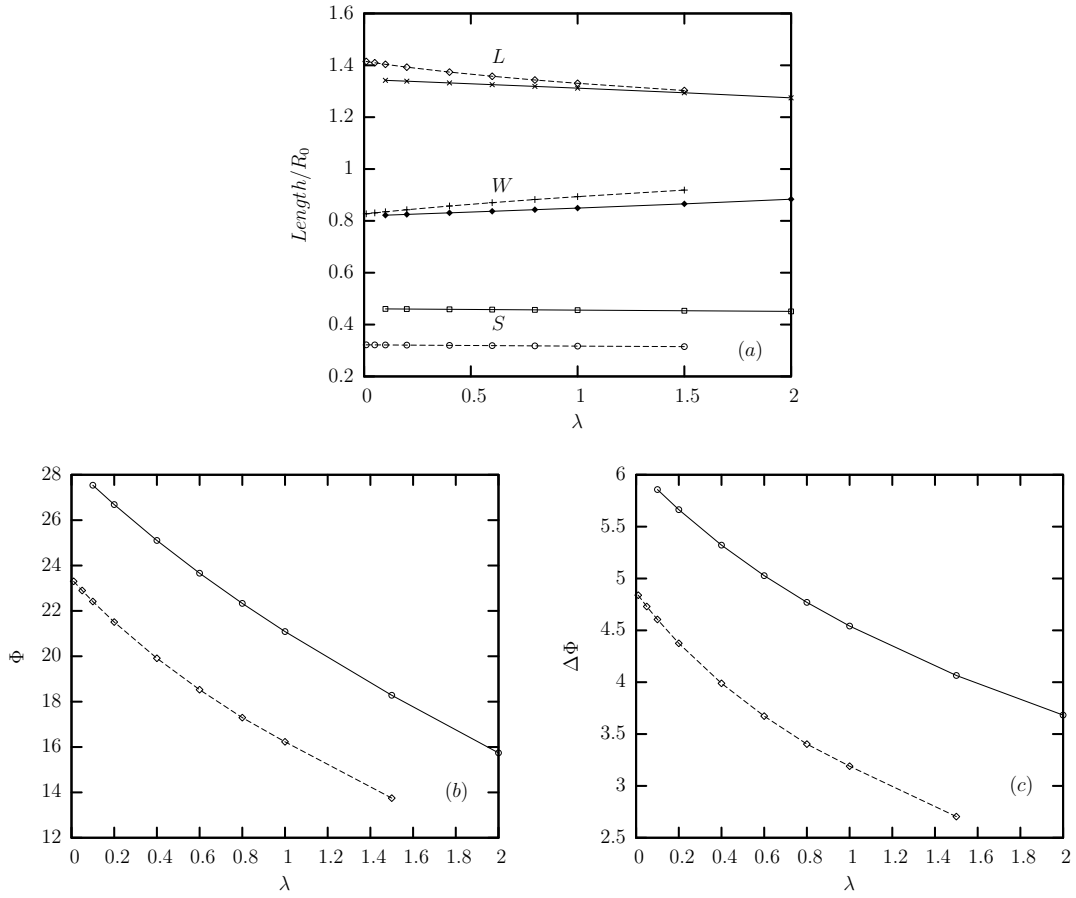


Figure 7.11: Erythrocyte deformation for swollen (solid lines) and normal (dotted lines) cells is examined as a function of viscosity ratio $\lambda$ for $Ca = 2$. (a) Normalized semi-axis lengths $L$, $W$, and $S$, (b) the orientation angle $\Phi$ and (c) the amplitude of angle oscillation, defined as $(\Phi_{max} - \Phi_{min})$.

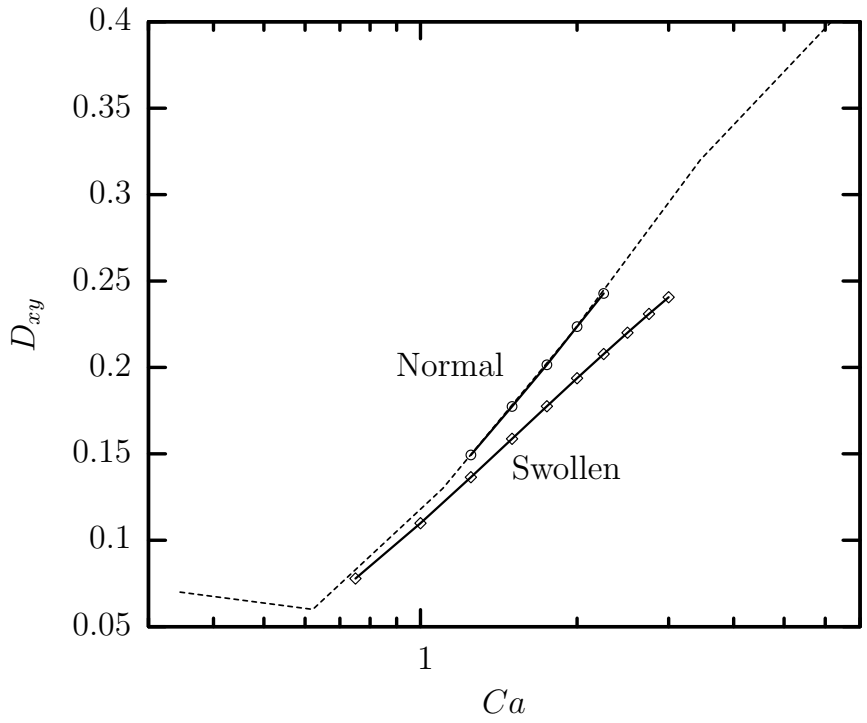


Figure 7.12: Erythrocyte deformation $D_{xy}$, as would be recorded in ektacytometry, is shown as a function of capillary number for $\lambda = 0.1$. The simulation results for cells with normal physiological parameters (from Figure 6.8) are shown along with the results for swollen erythrocytes. The dotted line indicates the data from ektacytometry with normal cells assuming $G_s = 2.43 \times 10^{-3}\ mN/m$.

chemical means [14]. However, in the disease states, both the surface area to volume ratio and the membrane mechanical properties are affected [56]; it is not clear if one or the other is primarily responsible for the decreased erythrocyte deformability.

Our results in this section demonstrate that erythrocytes with elevated surface area to volume ratios have increased thickness $S$, but show minimal change in lengths $L$ and $W$. Since $L$ and $W$ are most closely related to the lengths observed in these experimental systems, this suggests that the swelling has little effect on the cellular dimensions observed in the experimental geometries. Figure 7.12 shows the deformation parameter $D_{xy}$, as it would be observed in ektacytometry, for the swollen cells, compared to the results for normal cells presented in Figure 6.8 in Chapter 6. While the deformability for each capillary number is slightly depressed for the swollen cells, compared to the normal cells, the differences in deformability are minor. In contrast, Chasis and Mohandas, in their Figure 8, observed that elliptocytotic cells had a deformability of only 10 % of the value for a normal, healthy erythrocyte [20]. Figure 7.12 demonstrates that swelling alone cannot produce such affects, which suggests that the altered membrane mechanics play a greater role in reducing cellular deformability than does the cellular swelling.

# Chapter 8

# Conclusions

The capsule deformation problem is found in many scientific and engineering applications including pharmaceuticals, adhesives, cosmetics, and insecticides [17, 21, 45, 61, 87], and in biological systems such as the erythrocyte, which also consists of a liquid core enclosed by a deformable outer shell [56]. Like an emulsion or a suspension of solid particles, a capsule suspension can exhibit complex viscoelastic flow behavior as a result of the capsule micro-rheology [72]. For instance, the tank-treading motion of erythrocytes first observed by Schmid-Schönbein and Wells [74] is a contributing factor to the shear-thinning behavior of blood [9, 13]. Understanding or controlling flow applications involving these capsules or capsule suspensions requires a comprehension of the behavior of fluid-filled capsules in ambient flow, and the response of these capsules to various flow conditions.

The dynamic behavior of an object such as an elastic capsule or an erythrocyte is a fluid mechanics problem coupled to an elastic solid mechanics problem [66]. In this work, we have investigated the flow-induced deformation dynamics of elastic capsules and erythrocytes using the Spectral Boundary Element (SBE) method, which we have developed for interfacial dynamics of elastic shells with shearing and area-dilatation tensions in Stokes flow. This numerical method, originally designed

for fixed boundary Stokes flow computations [42, 57, 59] and later extended for the deformation of viscous droplets [88], has excellent geometric versatility, and is more robust than previous methods. By using the boundary integral formulation, we avoid creating a large dense system as required for spectral methods used in volume discretization. The SBE algorithm also preserves the exponential convergence in the numerical accuracy as the number of spectral points increases, which is the primary advantage of spectral methods. The accuracy of the method and the associated exponential convergence have been demonstrated for the calculation of the geometric properties of a fixed-boundary interface, such as the interfacial curvature, as well as the dynamic evolution of the interfacial shape.

In a planar extensional flow, our investigations have revealed a shape transition for strain-hardening Skalak capsules to a cusped conformation at high flow rates which occurs due to the appearance of compressive tensions near the capsule edges. The transition from spindled to cusped shapes allows the capsule to withstand the hydrodynamic forces at higher flow rates, similar to cusp formation with low-viscosity drops or bubbles in strong extensional Stokes flows [16]. These cusped geometries have been observed experimentally [6], and further results should be experimentally attainable; for mm-size capsules made from aminomethacrylate membranes with shearing modulus $G_s = O(10^{-2})$ N/m, flow rates $Ca = O(1)$ requires shear stress $\mu G = O(10)$ Pa [61]. Our computational method also reveals a region of bifurcation at high capillary numbers, in which both spindled and cusped equilibrium geometries can exist for a single flow rate. Adjusting the viscosity ratio $\lambda$ raises or lowers the lower limit of the bifurcation region. This suggests that cusp

formation could be controlled or eliminated through manipulation of the viscosity ratio. The large values of the edge curvature for spindled and, more importantly, for cusped capsules, along with the fact that the membrane tensions are complicated functions of the interfacial geometry, clearly indicate the need for a highly-accurate computational methodology (such as our interfacial spectral algorithm) for the accurate determination of membrane dynamics in strong flows.

In contrast to Skalak capsules, which are strain-hardening, the strain-softening Neohookean capsules we examined become highly extended at much weaker flow rates, but no formation of steady-state cusped shapes is observed. The geometries of the extended Neohookean capsules are also less rounded, and more lamellar, compared to the shapes of the Skalak capsules. We have contrasted the strain-hardening versus the strain-softening behavior by examining the membrane tension over the entire range of capsule extension for the two membrane types, and observed a linear increase in tension for the Neohookean capsule, but a much greater increase for the Skalak capsule.

In addition to studying elastic capsules, we have also adapted the SBE method to model erythrocytes by using a biconcave disc reference geometry and adaptive prestress to enforce area incompressibility. This implementation of SBE accurately reproduces experimental data for erythrocyte deformation in an ektacytometer, and is, to the best of our knowledge, the first numerical method to do so. The SBE method allows examination of the erythrocyte deformation beyond the geometric constraints inherent in ektacytometry and other experimental techniques, including observation of the three-dimensional oscillatory behavior over a range of capillary

numbers and viscosity ratios.

Our results support a prediction by Fischer, Skalak, and coworkers [32] that the erythrocyte shear modulus decreases at small shear deformations. Other recent experimental results also support the idea that the shear modulus decreases at small deformations [1]. Additional conclusions regarding deformation of healthy erythrocytes deforming in shear flow include that much of the variation observed in parallel-plate viscometry systems [27] may be due to the time-variant oscillatory behavior we observe, and that the transition to tumbling at high viscosity ratio represents not a new behavior, but a continuation of the trend of decreasing orientation angle with increasing viscosity ratio.

The extended SBE method for erythrocytes was also employed to study the deformation of erythrocytes in a planar extensional flow, and the shear-induced deformation of osmotically swollen erythrocytes. In the extensional flow studies, the erythrocyte transitions to an ellipsoidal conformation at both low and high capillary numbers. We observed that the semi-axis lengths, relative to one another, are largely independent of the flow pattern. That is, the smallest and intermediate lengths depend only on the largest length $L$, which represents the overall cellular extension. This is consistent with the findings of previous investigators that erythrocyte deformation in microchannel systems is approximately the same as that in shear flow systems at the same wall shear stress [78], and suggests that similar cellular deformability data can be derived equally well deforming the cell in geometrically simple flow systems, as opposed to flow setups that may require complicated control systems.

Regarding swollen erythrocytes, our results show that changes in the surface area to volume ratio, as observed in osmotic swelling [30] or disease states [38, 56], primarily affect the smallest semi-axis length of the ellipsoid, which is the thickness of the tank-treading erythrocyte. Swelling also increases the angle of inclination in the shear plane. Little effect is seen on the largest or intermediate lengths of the deformed geometry. Because these lengths determine the geometry when viewed in experimental systems like ektacytometry, our results predict only minor differences between normal and osmotically swollen erythrocytes, as reflected in Figure 7.12. This suggests that for disease states like hereditary elliptocytosis, where the deformability of abnormal cells is only 10 % of the deformability for cells from healthy patients, the primary factor reducing the deformability is changes in the membrane mechanics, and not the altered surface area to volume ratio.

The Spectral Boundary Element method has in the recent past proven its effectiveness for fixed boundary computations [42, 57, 59], interfacial dynamics for viscous droplets [88], and now flow-induced capsule deformation. The spatial discretization allows accurate computation of surface quantities, including curvature and membrane tensions, which makes it more robust compared to previous low-order numerical methods for capsule deformation. With elastic capsules, it has revealed and characterized a process of cusp formation and shape bifurcation at high flow rates. Studying erythrocytes, the method produces results in excellent agreement with experimental results for erythrocyte deformation in shear flow, and it has allowed us to go beyond the geometric limitations of the experimental systems to study the three-dimensional geometry of the deforming erythrocyte in its entirety.

# Bibliography


[1] M. Abkarian, M. Faivre, and A. Viallat, Swinging of red blood cells under shear flow. *Phys. Rev. Lett.* **98**, 188302 (2007).

[2] L. K. Antanovskii, Formation of a pointed drop in Taylor's four-roller mill. *J. Fluid Mech.* **327**, 325 (1996).

[3] D. Barthès-Biesel, Motion of a spherical microcapsule freely suspended in a linear shear flow. *J. Fluid Mech.* **100**, 831 (1980).

[4] D. Barthès-Biesel and J. M. Rallison, The time-dependent deformation of a capsule freely suspended in a linear shear flow. *J. Fluid Mech.* **113**, 251–267 (1981).

[5] D. Barthès-Biesel and H. Sgaier, Role of membrane viscosity in the orientation and deformation of a spherical capsule suspended in shear flow. *J. Fluid Mech.* **160**, 119–135 (1985).

[6] D. Barthès-Biesel, Role of interfacial properties on the motion and deformation of capsules in shear flow. *Physica A* **172**, 103-124 (1991).

[7] D. Barthès-Biesel, A. Diaz, and E. Dhenin, Effect of constitutive laws for two-dimensional membranes on flow-induced capsule deformation. *J. Fluid Mech.* **460**, 211–222 (2002).

[8] D. Barthès-Biesel, Flow-induced capsule deformation. In *Modeling and simulation of capsules and biological cells.* (ed. C. Pozrikidis) Chapman and Hall, London 1–34 (2003).

[9] O. K. Baskurt and H. J. Meiselman, Blood rheology and hemodynamics. *Sem. Thromb. Hem.* **29**, 435–450 (2003).

[10] S. A. Berger, Physiological fluid mechanics. In *Introduction to bioengineering.* (eds. S. A. Berger, W. Goldsmith, and E. R. Lewis) Oxford Press, Oxford, 133–170 (1996).

[11] M. Bessis and N. Mohandas, A diffractometric method for the measurement of cellular deformability. *Blood Cells* **1**, 307–313 (1975).

[12] M. Bessis, N. Mohandas, and C. Feo, Automated ektacytometry: A new method of measuring red cell deformability and red cell indices. *Blood Cells* **6**, 315–327 (1980).

[13] J. J. Bishop, P. R. Nance, A. S. Popel, M. Intaglietta, and P. C. Johnson, Relationship between erythrocyte aggregate size and flow rate in skeletal muscle venules. *Am. J. Physiol. Heart Circ. Physiol.* **286**, H113–H120 (2004).

[14] M. Bor-Kucukatay, R. B. Wenby, H. J. Meiselman, and O. K. Baskurt, Effects of nitric oxide on red blood cell deformability. *Am. J. Physiol. Heart Circ. Physiol.* **284**, H1577–1584 (2003).

[15] A. Bransky, N. Korin, Y. Nemirovski, and U. Dinnar, An automated cell analysis sensing system based on a microfabricated rheoscope for the study of red blood cells physiology. *Biosens. Bioelect.* **22**, 165–169 (2006).

[16] J. D. Buckmaster, Pointed bubbles in slow viscous flow. *J. Fluid Mech.* **55**, 385 (1972);

[17] M. Carin, D. Barthès-Biesel, F. Edwards-Lévy, C. Postel, and D. C. Andrei, Compression of biocompatible liquid-filled HSA-alginate capsules: determination of the membrane mechanical properties. *Biotech. Bioeng.* **82**, 207–212 (2003).

[18] K. S. Chang and W. L. Olbricht, Experimental studies of the deformation of a synthetic capsule in extensional flow. *J. Fluid Mech.* **250**, 587–608 (1993).

[19] K. S. Chang and W. L. Olbricht, Experimental studies of the deformation and breakup of a synthetic capsule in steady and unsteady simple shear flow. *J. Fluid Mech.* **250**, 609–633 (1993).

[20] J. A. Chasis and N. Mohandas, Erythrocyte membrane deformability and stability: two distinct membrane properties that are independently regulated by skeletal protein associations. *J. Cell Biol.* **103**, 343–350 (1986).

[21] C. Dai, B. Wang, H. Zhao, and B. Li, Factors affecting protein release from microcapsule prepared by liposome in alginate. *Coll. Surf. B* **42**, 253–258 (2005).

[22] A. Diaz, N. Pelekasis, and D. Barthès-Biesel, Transient response of a capsule subjected to varying fluid conditions: effect of internal fluid viscosity and membrane elasticity. *Phys. Fluids* **12**, 948–957 (2000).

[23] A. Diaz, D. Barthès-Biesel, and N. Pelekasis, Effect of membrane viscosity on the dynamic response of an axisymmetric capsule. *Phys. Fluids* **13**, 3835–3838 (2001).

[24] A. Diaz and D. Barthès-Biesel, Entrance of a bioartificial capsule in a pore. *Comp. Mod. Eng. Sci.* **3**. 321–337 (2002).

[25] P. Dimitrakopoulos and J. J. L. Higdon, Displacement of fluid droplets from solid surfaces in Low-Reynolds-number shear flows. *J. Fluid Mech.* **336**, 351–378 (1997).

[26] P. Dimitrakopoulos and J. J. L. Higdon, On the displacement of three-dimensional fluid droplets from solid surfaces in low-Reynolds-number shear flows. *J. Fluid Mech.* **377**, 189–222 (1998).

[27] J. G. G. Dobbe, G. J. Streekstra, M. R. Hardeman, C. Ince, and C. A. Grimbergen, Measurement of the distribution of red blood cell deformability using an automated rheoscope. *Cytometry* **50**, 313–325 (2002).

[28] J. G. G. Dobbe, M. R. Hardeman, G. J. Streekstra, and C. A. Grimbergen, Validation and application of an automated rheoscope for measuring red blood cell deformability distributions in different species. *Biorheology* **41**, 65–77 (2004).

[29] C. D. Eggleton and A. S. Popel, Large deformation of red blood cell ghosts in simple shear flow. *Phys. Fluids* **10**, 1834–1845 (1998).

[30] E. Evans and Y. C. Fung, Improved measurements of erythrocyte geometry. *Microvasc. Res.* **4**, 335–347 (1972).

[31] O. Farago and P. Pincus, Statistical mechanics of bilayer membrane with a fixed projection area. *J. Chem. Phys.* **120**, 2934–2950 (2004).

[32] T. M. Fischer, C. W. M. Haest, M. Stöhr-Liesen, H. Schmid-Schönbein, and R. Skalak, The stress-free shape of the red blood cell membrane. *Biophys. J.* **34**, 409–422 (1981).

[33] T. M. Fischer, Shape memory of human red blood cells. *Biophys. J.* **86**, 3304–3313 (2004).

[34] L. Fournier and B. Joos, Lattice model for the kinetics of rupture of fluid bilayer membranes. *Phys. Rev. E* **67**, 051908 (2003).

[35] Y. C. Fung, *Biodynamics: circulation.* Springer-Verlag, New York (1984).

[36] P. L. Gould, *Analysis of shells and plates.* Prentice Hall, New Jersey (1999).

[37] N. Gov and S. A. Safran, Pinning of fluid membranes by periodic harmonic potentials. *Phys. Rev. Lett.* **69**, 011101 (2004).

[38] H. Hagerstrand, A. Iglic, M. Bobrowska-Hagerstrand, C. Lindqvist, B. Isomaa, and S. Eber, Amphiphile-induced vesiculation in aged hereditary spherocytosis erythrocytes indicates normal membrane stability properties under non-starving conditions. *Mol. Mem. Biol.* **18**, 221–227 (2001).

[39] O. P. Hamill and B. Martinac, Molecular basis of mechanotransduction in living cells. *Phsiol. Rev.* **81**, 685–740 (2001).

[40] M. R. Hardemann, P. T. Goedhart, J. G. G. Dobbe, and K. P. Lettinga, Laser-assisted optical rotational cell analyser (LORCA): I. A new instrument for measurement of various structual hemorheological parameters. *Clin. Hem.* **14**, 605–618 (1994).

[41] M. R. Hardemann, P. T. Goedhart, and N. H. Schut, Laser-assisted optical rotational cell analyser (LORCA): II. Red blood cell deformability: Elongation index versus cell transit time. *Clin. Hem.* **14**, 619–630 (1994).

[42] J. J. L. Higdon and G. P. Muldowney, Resistance functions for spherical particles, droplets and bubbles in cylindrical tubes. *J. Fluid Mech.* **298**, 193–210 (1995).

[43] R. M. Hochmuth, Micropipette aspiration of living cells. *J. Biomech.* **33**, 15–22 (2000).

[44] M. Husmann, H. Rehage, E. Dhenin, and D. Barthès-Biesel, Deformation and bursting of nonspherical polysiloxane microcapsules in a spinning-drop apparatus. *J. Coll. Int. Sci.* **282**, 109–119 (2005).

[45] I. B. Jang, J. H. Sung, and H. J. Choi, Synthesis of microcapsule containing oil phase via *in-situ* polymerization. *J. Mat. Science* **40**, 1031–1033 (2005).

[46] M. Kraus, W. Wintz, U. Seifert, and R. Lipowsky, Fluid vesicles in shear flow. *Phys. Rev. Lett.* **77**, 3685–3688 (1996).

[47] S. Kwak and C. Pozrikidis, Effect of membrane bending stiffness on the axisymmetric deformation of capsules in uniaxial extensional flow. *Phys. Fluids* **13**, 1234–1242 (2001).

[48] E. Lac, D. Barthès-Biesel, N. A. Pelekasis, and J. Tsamopoulos, Spherical capsules in three-dimensional unbounded Stokes flows: effect of the membrane constitutive law and onset of buckling. *J. Fluid Mech.* **516**, 303–334 (2004).

[49] E. Lac and D. Barthès-Biesel, Deformation of a capsule in simple shear flow: Effect of membrane prestress. *Phys. Fluids* **17**, 072105 (2005).

[50] E. Lac, A. Morel, and D. Barthès-Biesel, Hydrodynamic interaction between two identical capsules in simple shear flow. *J. Fluid Mech.* **573**, 149–169 (2007).

[51] J. Li, C. T. Lim, and S. Suresh, Spectrin-level modeling of the cytoskeleton and optical tweezers stretching of the erythrocyte. *Biophys. J.* **88**, 3707–3719 (2005).

[52] V. A. Lubarda, *Elastoplasticity theory.* CRC Press, Boca Raton (2002).

[53] S. May, Y. Kozlovsky, A. Ben-Shaul, and M. M. Kozlov, Tilt modulus of a lipid monolayer *Eur. Phys. J. E* **14**, 299–308 (2004).

[54] P. Méléard, C. Gerbeaud, P. Bardusco, N. Jeandaine, M. D. Mitov, and L. Fernandez-Puente, Mechanical properties of model membranes studied from shape transformations of giant vesicles. *Biochimie* **80**, 401–413 (1998).

[55] N. Mohandas, M. R. Clark, M. S. Jacobs, and S. B. Shohet, Analysis of factors regarding erythrocyte deformability. *J. Clin. Invest.* **66**, 563–573 (1980).

[56] N. Mohandas and J. A. Chasis, Red blood cell deformability, membrane material properties and shape: regulation by transmembrane, skeletal and cytosolic proteins and lipids. *Sem. Hem.* **30**, 171–192 (1993).

[57] G. P. Muldowney and J. J. L. Higdon, A spectral boundary element approach to three-dimensional Stokes flow. *J. Fluid Mech.* **298**, 167–192 (1995).

[58] Y. Navot Elastic membranes in viscous shear flow. *Phys. Fluids* **10**, 1819–1833 (1998).

[59] J. M. Occhialini, G. P. Muldowney, and J. J. L. Higdon, Boundary integral/spectral element approaches to the Navier-Stokes equations. *Int. J. Num. Meth. Fluids* **15**, 1361–1381 (1992).

[60] J. G. Papastavridis, *Tensor calculus and analytical dynamics.* CRC Press, London (1999).

[61] G. Pieper, H. Rehage, and D. Barthès-Biesel, Deformation of a capsule in a spinning drop apparatus. *J. Coll. Int. Sci.* **202**, 293–300 (1998).

[62] C. Pozrikidis, *Boundary integral and singularity methods for linearized viscous flow.* Cambridge University Press (1992).

[63] C. Pozrikidis, Finite deformation of liquid capsules enclosed by elastic membranes in simple shear flow. *J. Fluid Mech.* **297**, 123–152 (1995).

[64] C. Pozrikidis, Numerical studies of cusp formation at fluid interfaces in Stokes flow. *J. Fluid Mech.* **357**, 29 (1998).

[65] C. Pozrikidis, A spectral-element method for particulate Stokes flow. *J. Comput. Phys.* **156** 360–381 (1999).

[66] C. Pozrikidis, Interfacial Dynamics for Stokes Flow. *J. Comp. Phys.* **169**, 250–301 (2001).

[67] C. Pozrikidis, Effect of membrane bending stiffness on the deformation of capsules in simple shear flow. *J. Fluid Mech.* **440**, 269–291 (2001).

[68] C. Pozrikidis, Numerical simulation of the flow-induced deformation of red blood cells. *Ann. Biomed. Eng.* **31**, 1194–1205 (2003).

[69] C. Pozrikidis, Shell theory for capsules and cells. In *Modeling and simulation of capsules and biological cells* (ed. C. Pozrikidis) Chapman and Hall, London, 35–101 (2003).

[70] C. Pozrikidis, Axisymmetric motion of a file of red blood cells through capillaries. *Phys. Fluids* **17**, 031503 (2005).

[71] A. R. Pries, T. W. Secomb, H. Jacobs, M. Sperandio, K. Osterloh, P. Gaehtgens, Microvascular blood flow resistance: role of endothelial surface layer. *Am. J. Physiol. Heart Circ. Physiol.* bf 273, H2272–H2279 (1997).

[72] S. Ramanujan and C. Pozrikidis, Deformation of liquid capsules enclosed by elastic membranes in simple shear flow: large deformations and the effect of fluid viscosities. *J. Fluid Mech.* **361**, 117–143 (1998).

[73] E. Sackmann, Physical basis of self-organization and function of membranes: physics of vesicles. In *Structure and dynamics of membranes* (eds. R. Lipowsky and E. Sackmann) Elsevier Science, Amsterdam, 213–304 (1995).

[74] H. Schmid-Schönbein and R. Wells, Fluid drop-like transition of erythrocytes under shear. *Science* **165**, 288–291 (1969).

[75] T. W. Secomb, R. Hsu, and A.R. Pries, A model for red blood cell motion in glycocalyx-lined capillaries. *Am. J. Physiol. Heart Circ. Physiol.* **274**, H1016–H1022 (1998).

[76] T. W. Secomb, R. Hsu, and A. R. Pries, Motion of red blood cells in a capillary with an endothelial surface layer: effect of flow velocity. *Am. J. Physiol. Heart Circ. Physiol.* **281**, H629–H636 (2001).

[77] T. W. Secomb, R. Hsu, and A. R. Pries, Blood flow and red blood cell deformation in nonuniform capillaries: effects of the endothelial surface layer. *Microcirc.* **9**, 189–196 (2002).

[78] S. Shin, Y. Ku, M. Paek, J. Jang, and J. Suh, Rapid cell-deformability sensing system based on slit-flow laser diffractometry with decreasing pressure differential. *Biosens. Bioelect.* **20**, 1291–1297 (2005).

[79] R. Skalak and P. I. Branemark, Deformation of Red Blood Cells in Capillaries. *Science* **164**, 717–719 (1969).

[80] R. Skalak, A. Tozeren, R. P. Zarda, and S. Chien, Strain energy function of red blood cell membranes. *Biophys. J.* **13**, 245 (1973).

[81] J. M. Skotheim and T. W. Secomb, Red blood cells and other nonspherical capsules in shear flow: oscillatory dynamics and the tank-treading-to-tumbling transition. *Phys. Rev. Lett.* **98**, 078301 (2007).

[82] A. E. Smith, K. E. Moxham, and A. P. J. Middelberg, Wall material properties of yeast cells. Part II. Analysis. *Chem. Eng. Sci.* **55**, 2043–2053 (2000).

[83] J. Solon, J. Pécréaux, P. Girard, M.-C. Fauré, J. Prost, and P. Bassereau, Negative tension induced by lipid uptake. *Phys. Rev. Lett.* **97**, 098103 (2006).

[84] D. J. Steigmann and R. W. Ogden, Elastic surface-substrate interactions. *Proc. R. Soc. London A* **455**, 437–474 (1999).

[85] S. Sukumaran and U. Seifert, Influence of shear flow on vesicles near a wall: A numerical study. *Phys. Rev. E* **64**, 011916 (2001).

[86] H. Vink and B. R. Duling, Identification of distinct luminal domains for macromolecules, erythrocytes and leukocytes within mammalian capillaries. *Circ. Res.* **79**, 581–589 (1996).

[87] A. Walter, H. Rehage, and H. Leonhard, Shear induced deformation of microcapsules: shape oscillations and membrane folding. *Coll. Surf. A* **183**, 123–132 (2001).

[88] Y. Wang and P. Dimitrakopoulos, A three-dimensional spectral boundary element algorithm for interfacial dynamics in Stokes flow. *Phys. Fluids* **18**, 082106(1-16) (2006).

[89] A. M. Waxman, Dynamics of a couple-stress fluid membrane. *Stud. Appl. Math.* **70**, 63–86 (1984).

[90] H. Zhou and C. Pozrikidis, Deformation of liquid capsules with incompressible interfaces in simple shear flow. *J. Fluid Mech.* **283**, 175–200 (1995).

# Vita

Walter R. Dodson III was born in May 1981, in Frederick, Maryland. He attended Walkersville High School and graduated valedictorian in June 1998. He then matriculated at Washington University in St. Louis, where he studied from August 1998 to May 2002 in the Sever College of Engineering. In May of 2002, he graduated and received a Bachelor of Science degree in Chemical Engineering and a Bachelor of Science degree in Biomedical Engineering. During his undergraduate years, he performed research in bacterial genetics at the Washington University School of Medicine. There he produced work that was included in a paper published in the journal *Molecular Microbiology*. Following graduation, Walter returned to Maryland and began working at BioReliance Corporation in Rockville. His duties there involved him in many stages of final drug manufacturing for contract biopharmaceutical production. He remained at BioReliance through the acquisition by Invitrogen Corporation, and departed in November 2004. Walter enrolled in the Bioengineering Graduate Program at the University of Maryland, College Park, in January 2004. Under the guidance of Professor Panagiotis Dimitrakopoulos, he has conducted research regarding the flow-induced deformation of red blood cells and artificial microcapsules by developing new methods in computational fluid dynamics. He is defending his dissertation for the Doctor of Philosophy degree in April 2008.